universität wien

DISSERTATION

Titel der Dissertation

Nucleation and Defect Interactions in Colloidal Suspensions

angestrebter akademischer Grad

Doktor der Naturwissenschaften (Dr. rer.nat.)

Verfasser:	Wolfgang Lechner
Matrikel-Nummer:	0025283
Dissertationsgebiet (lt. Studienblatt):	Physik
Betreuer:	Univ.-Prof. Dr. Christoph Dellago

Wien, am 16. Februar 2009

Abstract

This thesis deals with two aspects of colloids, the liquid-solid transition and the interaction between defects in colloidal crystals. Using Monte Carlo simulations I investigated the free energy barrier that separates the undercooled liquid phase from the solid phase in the Gaussian-core model. Classical nucleation theory postulates that this barrier is due to the formation energy required to form a solid nucleus in an otherwise liquid environment. Only when this nucleus exceeds a certain critical size, the system freezes spontaneously. I also studied the applicability of Ostwald's step rule in this transition. The results from the analysis of the structural composition the critical nucleus suggest that in the high pressure regime the freezing can indeed be viewed as a two-step procedure. First, a HCP cluster forms in the undercooled liquid. When this cluster surmounts a certain threshold the core of the cluster transforms into a BCC-like structure. The surface to volume ratio of the clusters indicates that nucleus is not of spherical shape, as postulated by classical elasticity theory, but rather have a rough surface. The final solid usually contains defects. In this thesis I studied self-interstitials and vacancies and their interactions in two dimensions. The displacement field of interstitials with periodic boundary conditions can be described accurately with elasticity theory using Ewald summation, at least for distances larger than 15 lattice spacings from the defect center. For vacancies such a description is not possible. With Monte Carlo simulations the effective interactions between interstitials and vacancies was calculated. The interactions between defects are purely attractive even for defects of the same species. The at-

traction between two vacancies is larger than that between two interstitials by a factor of 2. The effective interaction between a pair of defects and an additional defect of the same species exhibits a pronounced local maximum at the smallest distance. The minimum is located such that the defects form strings. These string-like clusters are ended by two pairs of dislocations, the two-dimensional analog to prismatic dislocation loops observed in metals after ion radiation.

Zusammenfassung

Die vorliegende Arbeit beschäftigt sich mit zwei Aspekten kolloidaler Systeme: dem Übergang von flüssig zu fest und der Wechselwirkung zwischen Defekten in kolloidalen Kristallen. Mit Hilfe von Monte-Carlo Simulationen habe ich die freie Energiebarriere im Gaussian-core Modell zwischen unterkühltem flüssigen und festem Zustand untersucht. Die klassische Nukleationstheorie sagt voraus, dass der Grund für diese Barriere darin liegt, dass sich zuerst ein fester Nukleationskern in der unterkühlten Flüssigkeit bilden muss und es erst dann zu einem spontanen Phasenübergang kommt, wenn dieser eine bestimmte kritische Grösse überschreitet. Weiters habe ich untersucht, ob Ostwalds Stufenregel für dieses Modell anwendbar ist. Dazu habe ich die strukturelle Zusammensetzung des Nukleationskeims bestimmt. Dabei zeigte sich, dass es sich bei hohem Druck tatsächlich um einen Übergang in zwei Schritten handelt. Zuerst bildet sich ein Nukleationskeim mit hexagonal dichtest gepackter Struktur. Sobald der Nukleationskeim eine bestimmt Grösse überschreitet formt sich der innere Teil des Nukleationskeims in einen kubisch-raumzentrierten Kristall um. Eine Voraussetzung der klassischen Nukleationstheorie ist, dass der Nukleationskeim ein sphärisches Objekt ist. Um dies zu untersuchen habe ich das Verhältnis von Oberfläche zu Volumen des Nukleationskeims mit dem eines perfekt sphärischen Kristalles verglichen. Es zeigte sich, dass die in der Simulation vorkommenden Nukleationskeime eine viel rauere Oberfläche haben als perfekte sphärische Kristalle. Festkörper, die durch einfrieren entstehen, können Defekte enthalten. In dieser Arbeit habe ich Zwischengitterteilchen und Leerstellen in zwei Di-

mensionen untersucht. Das Verzerrungsfeld von Zwischengitterteilchen mit periodischen Randbedingungen kann sehr präzise mit den Gleichungen der linearen Elastizitätstheorie und Ewaldsummation beschrieben werden, zumindest für Abstände von mehr als 15 Gitterabständen. Für Leerstellen ist eine solche Beschreibung nicht möglich. Mit Monte-Carlo Simulationen habe ich die effektive Wechselwirkung zwischen den Defekten bestimmt. Diese ist ausschließlich anziehend, selbst für Defekte der selben Sorte. Die Anziehungskraft von Leerstellen ist um einen Faktor 2 größer als die von Interstitials. Die effektive Wechselwirkung zwischen einem Defektpaar und einem weiteren Defekt der selben Sorte ist ebenfalls stark attraktiv. Die minimale frei Energie erreicht das System jedoch nicht durch Bildung eines kompakten Clusters, sondern einer Defektkette. An beiden Enden dieser Ketten befindet sich jeweils ein Versetzungsdefekt. Diese Defekte können als zwei dimensionales Analogon zu sogenannten “prismatic dislocation loops” in drei Dimensionen gesehen werden.

Acknowledgments

First of all I would like to thank my supervisor Prof. Christoph Dellago, a *Doktorvater* one can only wish for. Many thanks to my parents, my girlfriend, my colleagues, and friends for their tireless support.

Preface

This thesis is based on work published or to be published as articles in peer reviewed journals. The following is a list of all articles that originated during the time of my thesis.

Included in this thesis :

Chapter 3:
Accurate determination of crystal structures based on averaged local bond order parameters, W. Lechner and C. Dellago, *J. Chem. Phys.* **129**, 114707 (2008).

Chapter 4:
Displacement fields of point defects in two-dimensional colloidal crystals, W. Lechner, E. Schöll-Paschinger, and C. Dellago, *J. Phys.: Condens. Matter* **20**, 40402 (2008).

Chapter 5:
Point defects in two-dimensional colloidal crystals: simulation vs. elasticity theory, W. Lechner and C. Dellago, *Soft Matter* **5**, 646 (2009).

Chapter 6:
Defect interactions in two-dimensional colloidal crystals: vacancy and interstitial strings, W. Lechner and C. Dellago, *Soft Matter*, (to be published 2009).

Not included in this thesis:

Equilibrium free energies from fast-switching trajectories with large time steps, W. Lechner, H. Oberhofer, C. Dellago, and P. L. Geissler, *J. Chem. Phys.* **124**, 044113 (2006).

On the efficiency of path sampling methods for the calculation of free energies from non-equilibrium simulations, W. Lechner and C. Dellago, *J. Stat. Mech.-Theory Exp.* **4**, 04001 (2007).

Chapter 2 consists of still unpublished work, which will hopefully be published in the near future.

Contents

Chapter 1

Introduction

Two aspects of colloidal crystals are studied in this thesis: the liquid-solid transition and the interactions between point defects in the crystals. For both the knowledge of the free energy is of crucial importance, as it is in understanding the mechanism of many physical phenomena. To illustrate this importance consider the liquid-solid transition of water: When pure water is cooled below the freezing temperature it will not become solid immediately, but rather stay liquid in a metastable state. However, as soon as a solid nucleus forms due to random fluctuations or a disturbance from outside, large enough to initiate the freezing event, the whole system will rapidly turn into ice. The formation of such a nucleus is a *rare* event, compared to the typical time scales accessible in computer simulations, and the system can last in the metastable undercooled liquid phase for a long time. The reason for that is a free energy barrier that separates the solid from the liquid state. This barrier can be understood, at least qualitatively, with the classical nucleation theory [1]. This theory postulates that the free energy of the crystalline nucleus consists of two terms,

$$\Delta G = \frac{4}{3}\pi r^3 \rho_f \Delta\mu + 4\pi r^2 \gamma. \tag{1.1}$$

Here, r is the radius of the nucleus, ρ_f the density of the final phase, $\Delta\mu$ the difference in the chemical potential between the two phases, and γ is

the surface free energy between the two phases. The first term corresponds to the contribution of the volume of the nucleus that already is in the free energetically favored phase. The second term corresponds to the unfavorable interface between the two competing phases. In the example above a solid nucleus forms in an undercooled liquid environment, where the solid core of the nucleus is already in the free energetically favored phase, but further growth is suppressed by the free energetically unfavored interface at the surface. Only if the size of the nucleus exceeds a critical volume, will the nucleus grow spontaneously. The critical size of the nucleus is simply the maximum of the free energy ΔG from Eq. (1.1) found by differentiation with respect to the radius r:

$$r^* = -\frac{2\gamma}{\rho_f \Delta\mu}. \tag{1.2}$$

Here, r^* is the critical radius of the nucleus. $\Delta\mu$ is negative and therefore the critical radius is positive. The free energy at the critical radius corresponds to the free energy barrier:

$$\Delta G^* = \frac{16\pi}{3}\frac{\gamma^3}{(\rho_f \Delta\mu)^2}. \tag{1.3}$$

Close to coexistence, the difference of the chemical potential of the two phases is small leading to a large critical radius r^* and barrier height ΔG^*. With increasing undercooling, r^* and ΔG^* decrease.

Homogeneous nucleation and the range of validity of classical nucleation theory have been studied previously for a large variety of systems and phase transitions with computer simulations and experiments. The free energy barrier of the liquid-solid transition was studied in a Lennard-Jones system [2], a hard sphere system [3] and a system of particles with a pair interaction $v(r) = \varepsilon(\sigma/r)^{12}$ [4]. Besides of the liquid-solid nucleation also the vapor-liquid nucleation [5, 6] was studied in the Lennard-Jones system. Here, a liquid droplet aggregates in an undercooled vapor. Recently the vapor-solid nucleation was also studied [7]. The nucleation process in this transition

consists of two steps. First, a droplet forms in the vapor and then a solid nucleus forms in the liquid aggregate. The predictions of the critical size of the nucleus for both steps separately are in good agreement with classical nucleation theory [8]. Nucleation also governs the transition from superheated solid to liquid [9] where, again, the critical size of the fluid liquid is in good agreement with classical nucleation theory. Classical nucleation theory was also confirmed by neutron-scattering experiments on polyolfin [10, 11] as well as real-space imaging of colloidal crystals [12].

Chapter 2 of this thesis is dedicated to the computation of the free energy barrier that governs the liquid-solid transition in a colloidal crystal. As a model for colloidal particles the Gaussian-core model [13, 14, 15] was used, for which the nucleation process is still unexplored. The phase diagram of the system is known and exhibits two unusual features that may lead to an interesting transition behavior. A remarkable phenomenon is the so called reentrant melting, best seen in the phase diagram shown in Fig. 1.1. When the system initially at point P_1 (see. Fig 1.1) is compressed isothermally and reaches point P_2, the system undergoes two transitions. First, it crosses the coexistence line and the system freezes. After further compression, the system melts again and finally reaches P_2. Another interesting feature of the phase diagram is the fact that the solid phase consists of two stable regions; an FCC and a BCC region. This leads to the question whether the transition in the low density region (arrow A in Fig. 1.1) differs from that in high density region (arrow B) and if so, how the transitions differ. The final phases of A and B differ in structure, but does this influence the structure of the critical nucleus as well? These questions will be addressed in Chapter 2.

The latter question is of special interest in the light of Ostwald's step rule [16]. Ostwald predicted in 1897 that the phase of the critical nucleus will not necessarily be the thermodynamically most favorable phase, but to the one with the lowest free energy barrier with respect to the original phase. Alexander and Tague [17] argued, on the basis of Landau theory, that for a

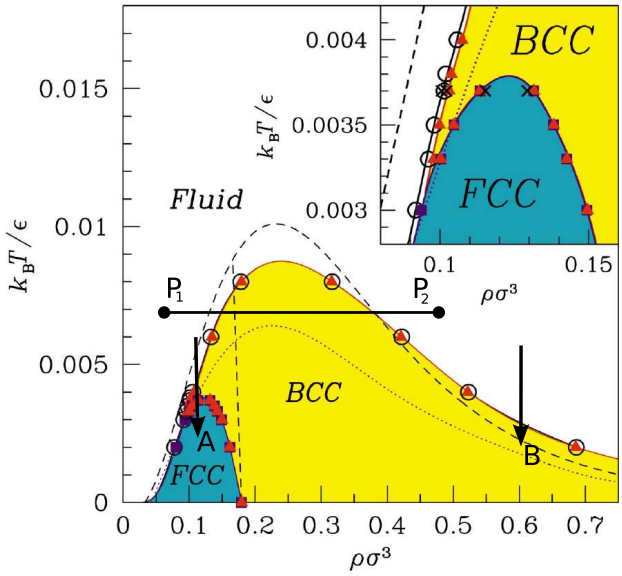

Figure 1.1: Phase diagram of the Gaussian-core model (figure taken from [14]). The nucleation process was studied for and undercooling indicated by the arrows A and B. The points P_1 and P_2 and their connection illustrate reentrant melting described in the text.

liquid-solid transition this phase would always be the BCC phase, at least for small undercooling. This theory was recently corroborated by computer simulations [18, 19, 20]. The simulations showed that in a Lennard-Jones system, although the FCC phase is the most stable one, the surface of the nucleus is BCC-like ordered. Similar results and evidence for a rearrangement process of the particles during the nucleation was also found with molecular dynamics simulations [21]. The crucial and challenging part of all these investigations is the determination of crystal structures on an atomistic level. Most of the mentioned studies [18, 19, 20, 21] rely on the so called local bond order parameters [22]. These parameters allow one to determine the crystal structure of individual particles from the neighboring particles and therefore to analyze the composition of the nucleus. In this thesis these order parameters as well as an enhanced version of them are discussed in detail in Chapter 3. These enhanced order parameters allow a more accurate

distinction between different crystalline structures by taking into account not just the nearest neighboring particles, but also the second shell. With these enhanced order parameters the structure of each individual particle can be determined with high precision. This allowed us to study the structural composition of the critical nucleus on an atomistic level. The knowledge of the composition of the nucleus is the key to address the question whether Ostwald's step rule is applicable here. For example: a nucleus that consists of a core that is already in the thermodynamically stable phase with a surface in a different structure would be an indication that Ostwald's step rule applies. A homogeneous cluster in the thermodynamically stable phase speaks against Ostwald's step rule. Such a structural analysis is discussed in Chapter 2.

After the phase transition is completed a crystal originates from the once liquid system. In general, this crystal will contain defects like stacking faults, dislocations, or domains with an interface between them. In our simulations, we observed other common defects, namely vacancies and self-interstitials. It turns out that these defects are highly mobile and tend to form stable clusters. This surprising observation motivated us to study the attractive defect interactions that lead to defect aggregation and cluster formation in more detail.

The attraction between defects that is responsible for clustering was observed in two dimensional crystals as well [23, 24]. In this system, particles are added to or extracted from an otherwise perfect hexagonal lattice. The two dimensional case is of special interest, because recent technologies like optical tweezers and video microscopy allow experimentalists to study such crystals on an atomistic level [25, 26]. Employing these methods, experimentalists already studied the interaction between dislocations [27, 28] in colloidal crystals. These interactions, central to the Kosterlitz-Thouless-Halperin-Nelson-Young theory for two-dimensional melting [29], are well described by elasticity theory and therefore the question arises if such a description is also applicable to the interaction between interstitial and vacancies.

A central quantity of elasticity theory is the displacement field. Chapters

4 and 5 deal with the description of the displacement fields of interstitials and vacancies within the framework of elasticity theory and a comparison with simulation results. The displacement field consists of the vectors that point from the original positions of the particles in a perfect crystal to their positions in the crystal with defects. For vacancies as well as interstitials, the displacement field close to the defect strongly depends on the actual configuration of the defect. Different stable configurations exist that differ in energy as well as symmetry. In both cases, for vacancies and interstitials, the configuration with a twofold symmetry is the one with the lowest energy. However, far away from the defect the displacement field becomes radially symmetric. In this regime, elasticity theory is a good description of the system. In elasticity theory, interstitials and vacancies are modelled by two pairs of forces acting on an infinitely extended medium in x- and y-direction (see Fig. 1.2), where the strength F of the forces goes to infinity and their distance h goes to zero, such that, the product Fh is a constant. The result of such a defect is

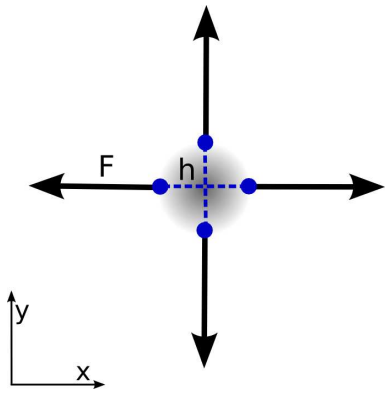

Figure 1.2: Model of a point defect in elasticity theory. Two pairs of forces act in opposite directions with a strength of F on points with a distance of h.

a displacement field that decays proportional to $1/r$, where r is the distance from the defect. In computer simulations this decay can not be observed, not even at temperature $T = 0$. Since usually computer simulations are carried out with periodic boundary conditions , this means that also the equations of elasticity theory have to be solved with periodic boundary conditions. This

can be achieved with the Ewald summation technique familiar from electrostatics with periodic boundaries [70]. The displacement field of interstitials far from the defect is in very good agreement with the simulation results, but close to the defect, large deviations occur. In contrast to interstitials, vacancies cannot be modeled as point defects in elasticity theory even far away from the defect center.

Now that we understand the displacement field of the defects, can we find a way to describe the interactions between interstitials and vacancies in the framework of elasticity theory? It turns out, however, that the interactions have a very short range and this is not the regime where elasticity theory is accurate. In Chapter 6 we study the effective interaction with Monte Carlo simulations. Defect interactions have been studied earlier in a Lennard-Jones system [23] and a Yukawa system [24]. Both investigations find a strong attractive interaction between the defects. In this thesis, the effective interaction of two defects is considered as a function of their distance r. This free energy is essentially the reversible work required to bring the defects from an infinite distance to distance r. In a Monte Carlo simulation, this free energy can be calculated from the the propability $P(r)$ of finding two defects at distance r. Then, $F(r) = -k_B T \ln P(r)$, where $F(r)$ is the free energy, T is the temperature, and k_B is Boltzmann's constant.

Our computer simulations show that the interaction between two defects is purely attractive and has a range of about 7 lattice spacings. The most favorable distance of two interstitials or two vacancies is at a distance of 1 lattice spacing, that is, the defects tend to form defect pairs. If one adds another defect of the same species, this additional defect is attracted by the defect pair. Surprisingly, the configuration of 3 defects is not a closed packed one, but rather has a string-like geometry. On both sides of the string, pairs of dislocations are attached that can be viewed as the two dimensional analogs of prismatic dislocation loops. Such dislocation loops form around platelets of vacancies that aggregate in metals after ion or neutron irradiation [30]. The strings that we have observed in our two-dimensional system are

highly mobile in the direction of the Burger's vectors of the dislocations that end the string. The strings are stable even for large numbers of defects (we observed string formation in systems with up to 40 defects). A typical snapshot of a defect string that consists of 5 vacancies is depicted in Fig. 1.3. A detailed analysis of the energetics, structure and dynamics of defect strings is provided in Chapter 6. We are planning a collaboration with an experimental group and we hope that the proposed defect strings will be observed in the experimental setup as well. In the experiments particles are confined by gravity to a water-air interface such that the mobility of the particles is limited to two dimensions. The particles are then traced individually with video microscopy. This allows a detailed analysis of the dynamics of defects in two dimensional colloidal crystals.

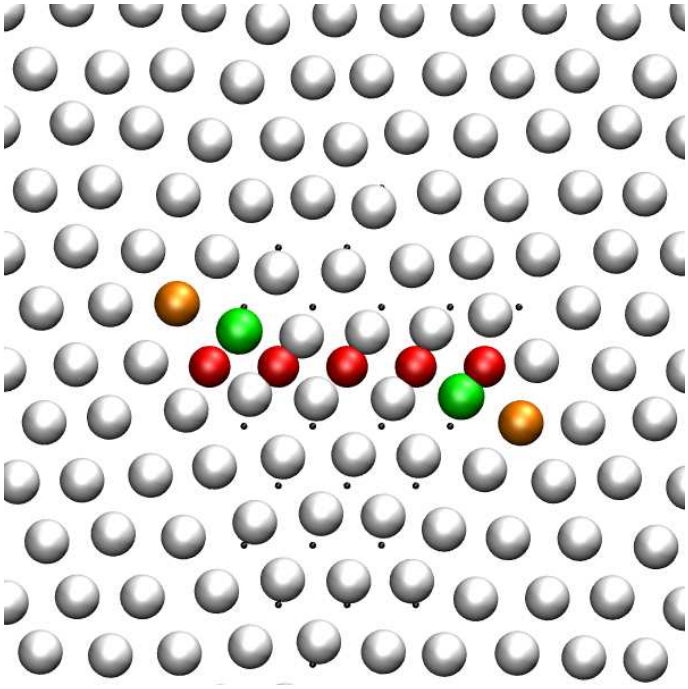

Figure 1.3: A typical snapshot of a defect string consisting of 5 vacancies. Red spheres denote unoccupied lattice points. White, green and orange spheres are particles with 6, 7 and 5 nearest neighbors. The number of nearest neighbors was determined using a Voronoi construction. The small black spheres denote lattice sites.

The studies on nucleation and defect interactions also raised questions that I will hopefully have the chance to study in the future. For the study of the nucleation process two separated structure analysis were required. First, the free energy barrier was calculated and then the structural composition of the clusters was determined (see Chapter 2 and 3). For the first part it is an advantage to use a method that is sensitive to the crystallinity of the particles but insensitive to the particular structure. This structure analysis is done in a second step. The enhanced order parameters discussed in Chapter 3 might have the potential to allow both steps at once in a consistent way. The advantage of such an approach would be a more consistent result. However, if crystal structures other than FCC,HCP, and BCC are involved in the transition this consistent method and the two step method would result in different free energies. The comparison of the two methods is an interesting study that hopefully will be addressed in the near future.

Another interesting question is the diffusion of the defect strings that we observed in the two dimensional colloidal crystals. Preliminary computer simulations have shown that the diffusion of strings consists of two parts. A gliding phase, characterized by fast movemet of the strings in one dimension, and a rare rotational phase that allows the whole string to change its direction. The frequency of the rotations seems to depend on the length of the strings: the smaller the strings, the more rotations were observed. Further investigations are required to quantify this behavior.

Part I

Nucleation

Chapter 2

Nucleation in the Gaussian-core model

2.1 Introduction

Pure water can be undercooled far below zero and still stay in a liquid metastable state. However, in such a metastable state a small disturbance can suffice to trigger the freezing of the whole system [31]. The reason for this intriguing behavior is a free energy barrier that separates the undercooled liquid state from the thermodynamically favorable solid state. The origin of this barrier can be best understood with classical nucleation theory. This theory posits that the free energetically most convenient transformation pathway involves the formation of a crystalline nucleus in the supercooled liquid. The barrier results from two competing terms:

$$\Delta G(r) = \frac{4}{3}\pi r^3 \rho_s \Delta\mu + 4\pi r^2 \gamma. \tag{2.1}$$

Here, r is the radius of the crystalline nucleus, which is assumed to be spherical, $\Delta\mu$ is the difference in the chemical potential between liquid and solid, γ is the surface free energy between liquid and solid, and ρ_s the density of the solid. The first term is proportional to the volume of the nucleus and

negative, because of the lower free energy of the solid cluster. The second term accounts for the interface energy and is proportional to the surface of the cluster. In the limit of a large cluster size the negative volume term dominates and the cluster will grow spontaneously. For small clusters, the surface term dominates and the system has to overcome a large barrier to finally freeze.

Classical nucleation theory has been compared earlier with results from computer simulations [2, 3, 4, 5, 6, 7, 8] and experiments [10, 11, 12] in various systems and for various transitions. This study deals with the liquid-solid transition in the Gaussian-core model [13, 14, 15] which serves here as a general model for colloidal particles [32]. Although the particles interact via a *simple* pair interaction, $v(r) = \varepsilon \exp[-r^2/\sigma^2]$, the phase diagram exhibits some surprising complexities. First, the phenomena of reentrant melting [13], and second, the existence of two different stable solid phases [13, 14]. At high pressure the system freezes into a FCC crystal, while at low pressure the BCC phase is favorable. This raises the question whether the nucleus of a transition in the two regimes differs in its structure or if the nucleus is unaffected by the final, thermodynamically most stable, phase. Also, it is not clear how this thermodynamically most favorable structure is reached. From a theoretical point of view these questions are directly related to Ostwald's step rule [16]. This theory states that the phase of the nucleus does not necessarily need to be the thermodynamically most stable one, the phase instead needs to be lying nearest to the bulk with respect to the free energy. Alexander and Tague [17] showed that in homogeneous system considering the liquid-solid transition this would always be the BCC phase, for small undercooling. In light of these predictions we will study the liquid solid transition in the BCC and FCC region of the Gaussian-core model with computer simulations.

2.2 Methods

The goal of this work is to calculate the free energy barrier of the liquid-solid transition in the Gaussian-core model and to analyze the crystal structure of the nucleus. Challenging problems arise in this task and in order to overcome these obstacles advanced simulation techniques are required. In the Monte Carlo simulation the free energy as a function of the size of the crystal nucleus can be inferred from

$$\Delta G(N_c) = -k_B T \log[P(N_c)]. \tag{2.2}$$

Here, ΔG is the Gibbs free energy, T is the temperature and $P(N_c)$ is the probability of finding a solid nucleus that consists of N_c particles. Note that the size of the nucleus is given as a function of the number of particles N_c in the nucleus and not as a function of the radius r. This means, unlike in Eq. (2.1), that the nucleus is not considered as a spherical object, but as a cluster of solid particles of any shape. This approach requires the knowledge of the crystallinity of each individual particle in the system. A method that allows such a distinction between solid and liquid particles will be discussed in Section 2.2.1. The second difficulty is an accurate sampling of $P(N_c)$. The nucleation event is a rare event, and a liquid will stay in an undercooled liquid state for a long time. This means that in a straight forward simulation only small cluster sizes can be sampled. Methods to overcome this difficulty are introduced in Section 2.2.2.

2.2.1 Order Parameter

Local bond order parameters are usually used to distinguish particles in a solid environment from those in a liquid one, and also to distinguish different crystalline phases. Local bond order parameters for a particular particle i

are defined as [22]

$$q_{lm}(i) = \frac{1}{N_b(i)} \sum_{j=1}^{N_b(i)} Y_{lm}(\vec{r}_{ij}). \tag{2.3}$$

Here, $N_b(i)$ is the number of particles within a given radius r_{nb} around particle i, $Y_{lm}(\vec{r}_{ij})$ are the spherical harmonics for separation $\vec{r}_{ij}$. The spherical harmonics are independent of the absolute value $r = |\vec{r}_{ij}|$ and depend on the relative angles $\phi = \arctan(y/x)$ and $\theta = \arccos(z/r)$ only. This definition of the bond order parameters q_{lm} is evaluated for all neighboring particles j of particle i. Thus, the bond order parameters q_{lm} depend on relative positions of the neighboring particles only. This definition allows the evaluation of the structure for different symmetries depending on the choice of l. With a choice of $l = 4$ or $l = 8$ the bond order parameters are sensitive to cubic symmetries, with $l = 6$ they are sensitive to hexagonal ones. The basic idea is to distinguish between liquid from solid particles by considering the correlation of the structure of particle i with that of all its nearest neighbors. In a solid these structures are highly correlated, while in a liquid they are rather uncorrelated. The degree of correlation of the structure of two particles i and j can be measured with the scalar product:

$$s = \vec{q}_6(i) \cdot \vec{q}_6(i) = \sum_{m=-6}^{6} \tilde{q}_{6m}(i) \cdot \tilde{q}^*_{6m}(j). \tag{2.4}$$

Here, l is chosen to be $l = 6$, $\tilde{q}_{6m}(i) = q_{6m}(i)/\sum_m \vec{q}_{6m}(i)$ is the normalized version of $q_{6m}(i)$ and the star indicates the complex conjugation. Two particles are considered to be correlated in their structure if $s > 0.5$ and their connection is called a solid bond [19]. The correlation is evaluated for all neighboring particles and if more than n_b of the them are connected by solid bonds, the particle is considered to be a solid particle, otherwise a liquid one. With a choice of $n_b = 8$ the liquid and the solid phase can be separated with high accuracy. The largest connected cluster of solid particles is then considered to be the solid nucleus.

The advantage of this definition of crystallinity is that it is independent of the specific crystal structure of the solid phase. Still, the particular crystal structure of the cluster is of special interest when one wants to gain insight into the nucleation process in the light of Ostwald's step rule [16].

Recently, ten Wolde and Frenkel [19] found evidence for the BCC favored nucleation process in a Lennard-Jones system. The authors studied the structural composition of the critical clusters and found that they can be described as FCC-like cores with a BCC-like surface. As a measure for the structural composition of the system they used the Steinhardt order parameter

$$q_l(i) = \sqrt{\frac{4\pi}{2l+1} \sum_{m=-l}^{l} |q_{lm}(i)|^2}. \tag{2.5}$$

Again, the parameter l controls the symmetry of $q_l(i)$. The authors first calculated the histogram of q_6 for the perfect BCC and FCC phase as well as for the liquid phase. Then, they obtained the solid clusters with the methods described above and calculated the histogram of q_6 for these clusters. This histogram is considered as the superposition of histograms of the perfect structures and the coefficients corresponding to the ratio of the structural composition of the cluster.

Desgranges and Delhommelle [21] used another approach to distinguish between different crystal structures. They defined regions in the two dimensional q_4-q_6-plane and q_4-w_4-plane with

$$w_l(i) = \frac{\sum\limits_{m_1+m_2+m_3=0} \begin{pmatrix} l & l & l \\ m_1 & m_2 & m_3 \end{pmatrix} q_{lm_1}(i) q_{lm_2}(i) q_{lm_3}(i)}{\left(\sum\limits_{m=-l}^{l} |q_{lm}(i)|^2 \right)^{3/2}}. \tag{2.6}$$

In a preliminary calculation the parameters q_4, q_6 and w_4 were calculated for particles in a perfect FCC, BCC, as well as, for a liquid. The parameters

q_4 and q_6 are then depicted as scatter plots. The points in the scatter plot populate delimited regions, and these emerging regions were then used as a reference for the distinction in the cluster analysis. The same was done with the parameters q_4 and w_4.

A similar technique was used in this thesis, based on the averaged order parameters discussed in Chapter 3. Here, we introduce the parameters

$$\bar{q}_l(i) = \sqrt{\frac{4\pi}{2l+1} \sum_{m=-l}^{l} |\bar{q}_{lm}(i)|^2}, \tag{2.7}$$

where

$$\bar{q}_{lm}(i) = \frac{1}{\tilde{N}_b(i)} \sum_{k=0}^{\tilde{N}_b(i)} q_{lm}(k). \tag{2.8}$$

Here, the sum goes over all neighboring particles of particle i, $\tilde{N}_b(i)$, plus the particle i itself. The parameters $\bar{q}_6$ and $\bar{q}_4$ are collected for a perfect FCC, HCP, and BCC structure as well as for the liquid phase. Figure 2.1 depicts the two dimensional reference scatter plot and the regions used to distinguish between the structures. The reference was taken from simulations at $P = 1\varepsilon/\sigma^3$ and $k_BT = 0.0016\varepsilon$.

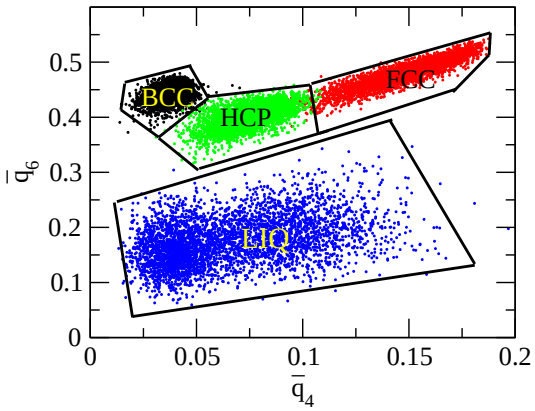

Figure 2.1: Definition of the regions in the $\bar{q}_4$-$\bar{q}_6$ plane for the distinction between different crystal structures and the liquid phase.

With this choice of parameters the different crystal structures can be distinguished almost unambiguously.

2.2.2 Sampling Techniques

At a small degree of undercooling the free energy barrier is high compared with the thermal energy of k_BT, and a spontaneous freezing event is difficult to observe in computer simulations. However, to determine the free energy barrier accurately all possible cluster sizes N_c need to be sampled. To overcome this sampling problem we used a combination of umbrella sampling and parallel tempering suggested by Auer and Frenkel [3]. We will summarize this approach in this section.

In a straightforward Monte Carlo simulation, the ensemble average of a observable A can be written as an average over a large number of measurements,

$$\langle A \rangle \approx \frac{1}{M} \sum_{i=1}^{M} A(r_i^N). \tag{2.9}$$

Here, M is the total number of measurements and r_i^N is the configuration of the system at the measurement i. The basic idea of the umbrella sampling technique of Torrie and Valleau [33] is to rewrite the ensemble average of observable A as

$$\langle A \rangle = \frac{\langle A/W(r^N) \rangle_W}{\langle 1/W(r^N) \rangle_W}. \tag{2.10}$$

Here, the angular brackets denote the ensemble average and $W(r^N)$ is the weighting function

$$W(r^N) = e^{-\beta\omega(r^N)}. \tag{2.11}$$

The function $\omega(r_i^N)$ is the bias function and can be chosen arbitrarily. In the following we will consider the harmonic function

$$\omega(r^N) = \frac{1}{2} k[N_c(r^N) - n_w]^2, \tag{2.12}$$

where k is a constant that can be chosen arbitrarily and regulates the effective width of the harmonic function $\omega(r^N)$. This definition of the bias function allows one to sample a restricted region in configuration space, a so called window. Instead of sampling the whole range of N_c in one single simulation, with this technique the simulation can be split up into many simulations, where each simulation samples a narrow windows around $n_{w,i}$. Here, $n_{w,i}$ is the center of window i. In practice such a window sampling can be implemented in a Monte Carlo simulation in the following way. First, $\omega_b = \omega(r^N)$ is evaluated for the particular configuration. Then, a fixed number of unbiased Monte Carlo moves are carried out according to the common Metropolis acceptance rule. After that, $\omega_a = \omega(r'^N)$ is evaluated, where r'^N are the positions of the particles after the MC moves. The whole trajectory is accepted or rejected with the acceptance probability

$$P_A = \min[1, \exp[-\beta(\omega_a - \omega_b)]], \tag{2.13}$$

This method allows one to sample cluster sizes around an arbitrary bias center $n_{w,i}$. The calculation of the size of the greatest cluster in the system $N_c(r^N)$ is computationally *expensive*, and therefore, this approach is more efficient than evaluating the cluster size after each MC move.

To facilitate large rearrangements in the cluster, Frenkel and Auer [3] used the parallel tempering scheme introduced by Geyer and Thompson [34] in addition to the umbrella sampling technique. Here, many window sampling simulations are performed simultaneously. All windows sample the same pressure and temperature, but different bias centers $n_{w,j}$. The index j denotes the different widows. During the simulation, neighboring windows are allowed to exchange their window centers $n_{w,j}$. The exchange move is implemented in the following way. First, window i is chosen at random. Then, the window center is exchanged with that of a neighboring window j with the probability

$$P_W = \min[1, \exp[-\beta(b_a - b_b)]], \tag{2.14}$$

where

$$b_b = \frac{k}{2}([N_{c,i} - n_{w,i}]^2 + [N_{c,j} - n_{w,j}]^2), \tag{2.15}$$

$$b_a = \frac{k}{2}([N_{c,j} - n_{w,i}]^2 + [N_{c,i} - n_{w,j}]^2). \tag{2.16}$$

$$\tag{2.17}$$

This acceptance probability is chosen such that detail balance is satisfied. The constant k and the individual window centers are chosen such that each window has a large overlap with its neighboring windows, thus resulting in a large number of exchange moves.

Finally, the individual parts of the free energy are unbiased and combined with the self-consistend histogram method [35].

2.3 Simulation Details

Let us now consider the concrete problem: the freezing in the Gaussian core model. In this model [13, 14, 15] particles interact via a pair-potential of Gaussian shape,

$$V(r) = \varepsilon e^{-(r/\sigma)^2}. \tag{2.18}$$

We considered a system consisting of $N = 10,976$ Gaussian core particles. The potential was truncated and shifted at a cutoff radius of $r_c = 3.0\sigma$, periodic boundary conditions were applied. The NPT ensemble was sampled using the Metropolis Monte Carlo rule with volume moves after every $10N$ MC steps. The simulation was performed at two particular pressures: at pressure $P_1 = 0.12\varepsilon/\sigma^3$ which corresponds to a density of approximately $\rho_1 = 0.1\sigma^3$ and pressure $P_2 = 1.0\varepsilon/\sigma^3$ which corresponds to a density of $\rho_2 = 0.6\sigma^3$. At P_1 at low temperatures the FCC structure is most stable and at P_2 the BCC structure. In order to speed up the simulation, cell lists with side length $l \approx r_c$ were used. In the high and low pressure simulation the

number of cells was $N_{L_1} = 8 \times 8 \times 8$ and $N_{L_2} = 12 \times 12 \times 12$, respectively. The high pressure nucleation was studied at temperatures $k_BT = 0.00168\varepsilon$ and $k_BT = 0.00160\varepsilon$. The low pressure nucleation at $k_BT = 0.0033\varepsilon$ and $k_BT = 0.0030\varepsilon$.

In order to distinguish particles in a solid environment from particles in a liquid environment the method based on the scalar product of q_6 described in subsection 2.2.1 was used. Two particles were considered to be nearest neighbors if their distance was below $r_{nb} = 1.7\sigma$ in the high pressure simulation. In the low pressure simulation r_{nb} was 3.0σ. Above the threshold $s > 0.5$ (see eq. (2.4)) a bond was considered to be solid. Particles with more than $n_b = 8$ bonds were considered to be solid particles. Altough the analysis of the crystallinity of the particles is rather unaffected by the choice the nearest neighbor distance, the structure analysis is sensitive to r_{nb}. The particular value of r_{nb} was obtainend from preliminary computer simulations where the nearest neighbor distance was adjusted such that the average number of nearest neighbors was 14 in a perfect BCC crystal and 12 in a FCC and HCP crystal.

Each simulation consisted of 20 windows with bias centers that were a multiple of 20. Therefore, the free energy was evaluated between $N_c = 0$ and approximately $N_c = 400$. The bias constant was set to $k_1 = 0.000033\varepsilon$ in the high pressure simulation and $k_2 = 0.00005\varepsilon$ in the low pressure simulation. In each simulation we carried out f $N_s = 2 \times 10^5$ MC sweeps and 1×10^5 volume moves in each of the 20 windows. An MC sweep consists of N (number of particles) MC moves. After every MC sweep the size of the clusters were evaluated and a swapping move was attempted.

2.4 Results

Figure 2.2 depicts a typical progress in the simulation. Each curve represents the actual clustersize of a particular computer node as a function of time measured in MC sweeps. Swapping the bias centers allowed each simulation to sample a large number of possible cluster sizes. Figure 2.3 depicts the bias center and the actual size of the cluster as a function of time for a particular computing node.

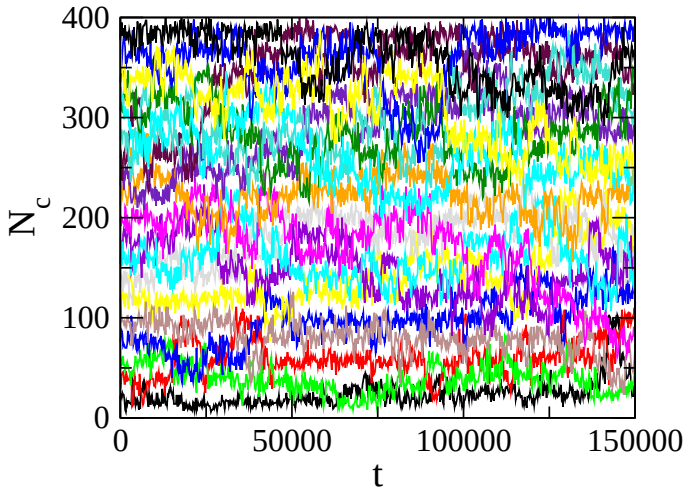

Figure 2.2: Typical progress of a windows sampling simulation as described above. Each curve represents the actual cluster size of each window. Every 100th MC sweep is plotted. Due to the possibility of window exchange moves, each individual trajectory can sample large parts of the configuration space. The time t is measured in MC sweeps of N MC steps each.

One main result of the simulation is the free energy barrier of the nucleation process as a function of N_c, the size of the largest cluster. Figure 2.4 depicts the free energy at temperatures $k_B T_1 = 0.0033\varepsilon$ and $k_B T_2 = 0.0030\varepsilon$ at a pressure of $P = 0.12\varepsilon/\sigma^3$. Under these conditions the most stable crystalline structure is the FCC structure [14]. The free energy exhibits a pronounced minimum at $N_c \approx 15$. This implies that in the undercooled liquid the most probable configuration is one with a cluster size of $N_c = 15$.

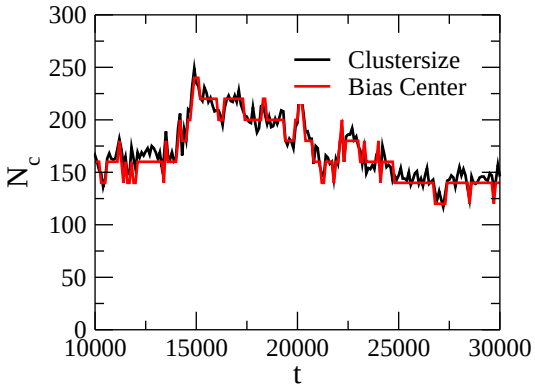

Figure 2.3: Clustersize as a function of time for a typical trajectory on one computing node. The actual clustersize (black) follows the bias center (red). The time t is measured in MC sweeps.

The height of the barrier is very sensitive to changes in the temperature. The barrier height changes from about $10k_BT$ to $25k_BT$ when going from T_1 to T_2. Also, the critical cluster size shifts from $N_c = 300$ to $N_c = 390$. Figure 2.5 shows the free energy barrier at pressure $P = 1.0\varepsilon/\sigma^3$ and a slightly larger undercooling than in the low pressure simulation. Again, the height and the critical size of the nucleus are sensitive to the degree of undercooling. At these conditions the free energy barrier is of size of $3 - 7k_BT$ and the critical nucleus is of size of $N_c = 120$ and $N_c = 200$.

The second question we addressed in this work is the applicability of Ostwald's step rule. This requires an analysis of the crystalline structure of the solid cluster with methods based on averaged local bond order parameters described in section 2.2.1. The regions in the $\bar{q}_4$-$\bar{q}_6$ plane (see Fig. 2.1) used as a reference were calculated as described in Chapter 3. Then, for each particle in the solid cluster the parameters $\bar{q}_4$ and $\bar{q}_6$ were determined after every MC sweep and analyzed with respect to the regions in the reference $\bar{q}_4$-$\bar{q}_6$ plane. Particles with a $\bar{q}_4$-$\bar{q}_6$ pair that does not fall into any of the regions were declared as particles with undefined crystal structure. With this method we studied the structural composition of the clusters taken from the simulations.

Figure 2.6 shows the ratio of different crystal structures in the solid

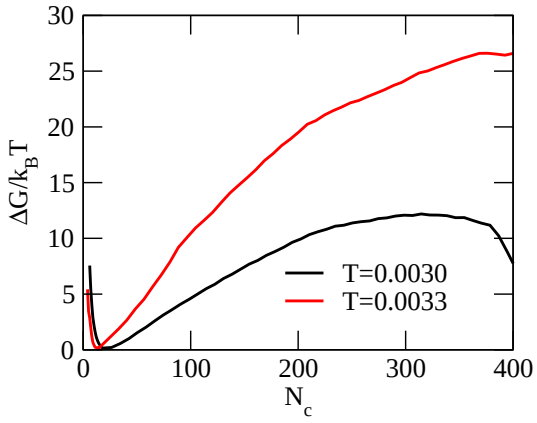

Figure 2.4: Free energy barrier of the nucleation process at a temperature $k_BT = 0.0030\varepsilon$ (black) and $k_BT = 0.0033\varepsilon$ and pressure $P = 0.12\varepsilon/\sigma^3$. At these conditions the crystalline phase with the lowest free energy is the FCC phase.

cluster as a function of the cluster size in the low pressure simulation at $k_BT = 0.0033\varepsilon$ and $P = 0.12\varepsilon/\sigma^3$. Most particles are identified as liquid ones, but the majority of crystal particles are HCP-like. The frequency of all other structures was below 1%. In the following we also determine the structural composition of the clusters as a function of the distance from the center of mass. Figure 2.7 depicts the structural composition of 100 independent clusters of size of about $N_c \approx 275$. The core is mostly HCP, but also BCC and FCC particles occur. For large distances most particles are identified as liquid ones. Clearly, the HCP phase is dominant one. BCC and FCC are only located a the centers of the cluster. In principle all particles in the solid cluster should be identified as one of the crystal structures. However, particles at the surface are often identified as liquid-like particles. This stems from the fact that two different methods are used to determine the crystallinity and to determine the actual structure. One single consistent method to do both analysis at once will be part of future work.

In the high pressure simulation at $k_BT = 0.00168\varepsilon$ and the pressure $P = 1.0\varepsilon/\sigma^3$ we obtained a different picture. Figure 2.8 shows the compo-

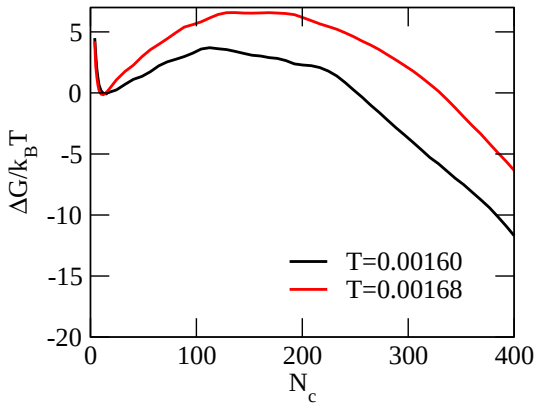

Figure 2.5: Free energy barrier of the nucleation process at a temperature $k_BT = 0.00160\varepsilon$ (black) and temperature $k_BT = 0.00165\varepsilon$ and pressure $P = 1.0\varepsilon/\sigma^3$. At these conditions the crystalline phase with the lowest free energy is the BCC phase.

sition of the crystalline structures as a function of the cluster size. Here, clusters up to $N_c \approx 200$ consist mainly of HCP and liquid particles. Above this size, which is about the critical cluster size, suddenly a large number of BCC particles emerges. We depicted the structural composition of the clusters in these two scenarios. Figure 2.9 depicts the composition for clusters of the size of about $N_c = 175$. The core consists both of BCC and HCP structures. Clusters above the critical size of $N_c = 200$ show a different composition (see. Fig. 2.10, where the composition of clusters of a size of about $N_c = 250$ are plotted). The core mainly consists of BCC-like particles. These BCC particles are surrounded by HCP particles. Their distribution has a maximum at a distance of $r \approx 3\sigma$. For large distances particles are identified as liquid particles. Figure 2.11 depicts a snapshot of a typical cluster of this size. Clearly, the core is BCC-like and the surface HCP-like (for the color code see text below the figure).

This observation suggests the following scenario for the Gaussian core model. In the low pressure regime, where the FCC structure is thermodynamically most stable, the particles freeze mainly into an HCP crystal. Even

for large clusters between $N_c = 250$ to $N_c = 300$ the core mainly consists of HCP. A rearrangement of the core to FCC was not observed in our simulations. In the high pressure simulation a two step nucleation can be observed. First, the cluster below the critical size freezes into the HCP structure. As the cluster grows, the center of the cluster transforms into a BCC structure, which is the thermodynamically stable one. Still, the surface is mainly HCP-like. This is a demonstration of Ostwald's step rule. Here, the particles first freeze into a HCP structure and then rearrange into a BCC structure. This is in contrast to the predictions of Alexander and Tague [17], where the authors argued that the BCC should be the most favorable for a liquid-solid transition, at least close to coexistence. Therefore, the surface should be BCC. This was also observed in a [18, 19, 20] Lennard-Jones system.

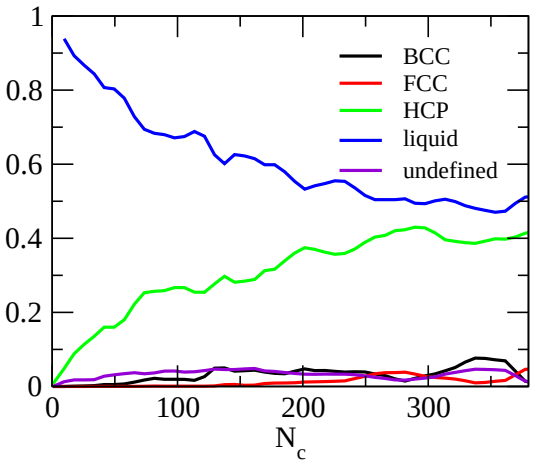

Figure 2.6: Fraction of solid cluster particles in the various structures as a function of the cluster size at $P = 0.12\varepsilon/\sigma^3$ and $k_BT = 0.0033\varepsilon$. Most particles are liquid-like or HCP-like. Only a small minority of particles form a BCC or FCC structure.

Another important part of the structure analysis is the shape of the nucleus. One of the assumptions of classical nucleation theory is that the cluster is of spherical shape. In order to test the simulation results against this assumption we studied the ratio between volume and surface of the cluster. Here, a surface particle is defined as a particle that is not part of the clus-

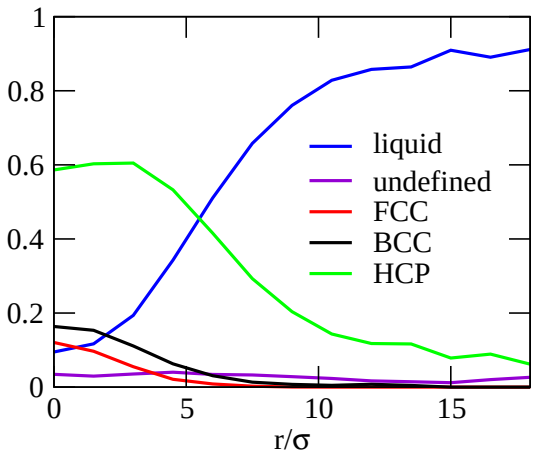

Figure 2.7: Ratio of different crystalline structures in the cluster as a function of the distance from the center of mass in the high pressure simulations with $P = 0.12\varepsilon/\sigma^3$ and $k_BT = 0.0033\varepsilon$. The average of 100 independent clusters was taken into account with a cluster size of about $N_c \approx 275$. The clusters consist of HCP cores. BCC structures are insignificant for this transition.

ter but has at least one nearest neighbor that is. The number of surface particles is N_s. Figure 2.12 depicts the ratio N_c/N_s of the cluster at pressure $P = 1.0\varepsilon/\sigma^3$ and $P = 0.12\varepsilon/\sigma^3$ and the ratio of a perfect spherical FCC crystal. This perfect spherical crystal was constructed by taking into account all particles from a perfect FCC crystal that lie within a certain radius r_c. The ratio of the perfect spherical crystal becomes linear in the limit of large r_c but for small numbers of particles the ratio exhibits fluctuations due to the cutoff. N_c/N_s of the clusters from the simulation is smaller than that of the expected perfect spherical shape. Therefore, the cluster is not of perfect spherical shape but has a rather rough surface. However, this rough surface can be reproduced by an artificial algorithm to generate clusters sketched in Fig. 2.13. The basic idea of this algorithm is to let a crystal grow by adding particles at its surface with a probability according to its number of bonds. Figure 2.13 shows the first 3 steps of this algorithm. For simplicity a two-dimensional quadratic lattice is used in the sketch. First, a single particle is defined to be solid and all its nearest neighbors are determined (see 2.13a). In a two dimensional quadratic lattice there are 4 neighbors with 1 bond

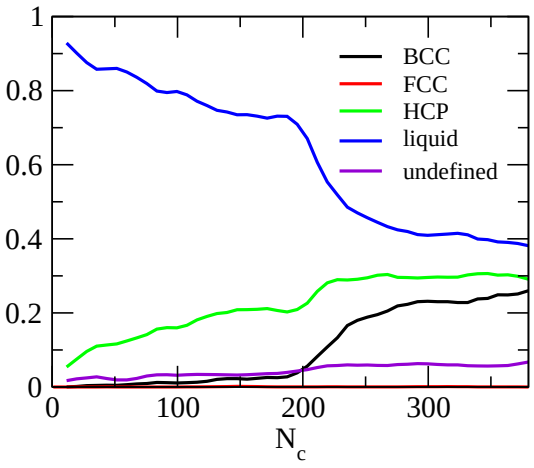

Figure 2.8: Fraction of solid cluster particles in the various structures as a function of the cluster size at $P = 1.0\varepsilon/\sigma^3$ and $k_BT = 0.00168\varepsilon$. Under these conditions small clusters are mostly liquid and HCP-like. For clusters larger than the critical size of about $N_c = 200$ BCC-like particles emerge.

each. Then one of these neighbors is chosen with a probability according to its number of bond and defined as solid particle. In this case all 4 neighbors have a probability of 1/4. The weight of probability to chose a particular neighbors is indicated by the numbers on top of the particles. In Fig. 2.13b the particle to the right of the original particle was chosen, and again all possible neighbors are determined. All 6 possible neighbors have again only one bond with the cluster and therefore their probability is 1/6 each. After the third particle is added (see Fig. 2.13c) 8 bonds are present where one of the possible neighbors is chosen with probability 2/8 and the rest of the particles are chosen with probability 1/8. This algorithm is followed up to a number of particles N_c^{max}. The ratio of N_c/N_s was evaluated for each cluster generated with this procedure and the average over many such realizations was taken. To compare the clusters with that from the simulation, the three dimensional FCC lattice was taken as reference system rather than a quadratic lattice as in Fig. 2.13. The result of this algorithm is depicted as the green curve in Fig. 2.12. This curve is in very good agreement with the ratio of the clusters from the simulation especially for small cluster sizes. Larger clusters are more

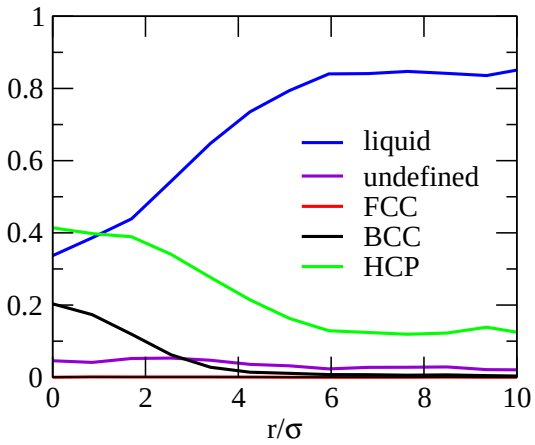

Figure 2.9: Ratio of different crystalline structures in the cluster as a function of the distance with respect to the center of mass in the high pressure simulation with $P = 1.0\varepsilon/\sigma^3$ and $k_BT = 0.00168\varepsilon$. The average of 100 independent clusters was taken into account with a cluster size between $N_c = 150 - 200$. The core of these clusters consisits of BCC and HCP particles. The particles away from the defect are mostly liquid-like.

compact in the simulation, this could be an indication for the rearrangement also observed in the structure analysis. Drawing conclusions from this model is not straightforward. The model generates clusters without any connection to the energy of the system. Therefore, the average over many realizations cannot be viewed as a genuine ensemble average. The clusters observed in the simulation are of course drawn from an equilibrium distribution. Still, the agreement of the two curves is promissing and further investigations are required to fully understand the structure of the clusters.

2.5 Conclusions

The free energy barrier of the nucleation process in the Gaussian-core model was calculated in the low and high pressure regime. To do that, the methods of Auer and Frenkel [3], a combination of umbrella sampling and parallel tempering, were successfully applied. At a similar degree of undercooling the free energy barrier exhibits a similar shape in the high and low pressure

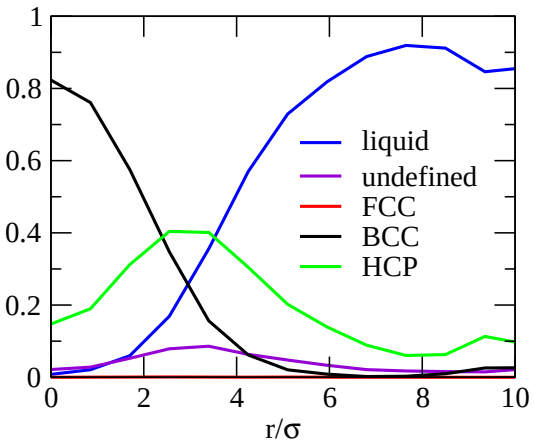

Figure 2.10: Ratio of different crystalline structures in the cluster as a function of the distance with respect to the center of mass in the high pressure limit $P = 1.0\varepsilon/\sigma^3$ and $k_BT = 0.00168\varepsilon$. The average of 100 independent clusters was taken into account with a cluster size between $N_c = 250 - 300$. Clusters of this size consist of a BCC core and HCP surface. Particles far away from the center of mass are mostly identified as liquid-like particles.

regime. The structure analysis introduced here based on averaged local bond order parameters was applied to the clusters. This analysis showed distinct differences between the low and the high pressure regime. In the low and in the high pressure regime the particles freeze into HCP, but in the high pressure simulations the core of the clusters rearranged into a BCC structure, the stable structure at the given pressure and temperature. In the high pressure regime, Ostwald's step rule can be clearly observed. The surface to volume ratio gives reason to the assumption that the typical cluster has a rather rough surface and is not of spherical shape as predicted by classical nucleation theory. Hopefully, our further investigations will answer the questions that emerged from this study.

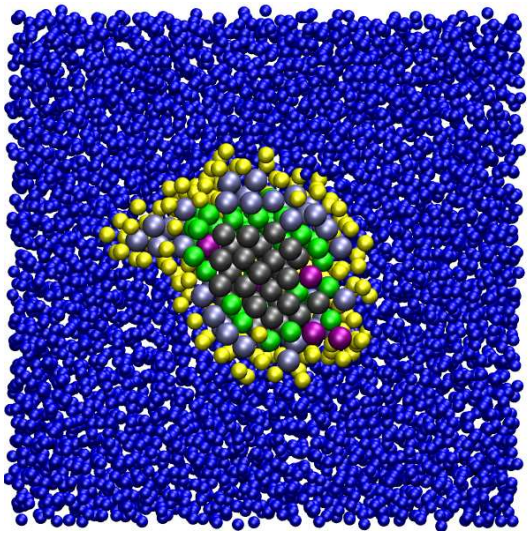

Figure 2.11: A snapshot of a typical cluster in the high pressure simulation. The core is already in the BCC phase (black particles), surrounded by HCP-like particles (green). At the surface particles are identified as liquid-like particles (light blue). FCC particles (red) and undefinable particles (violet) are insignificant in the solid cluster. The small blue particles are particles that are not part of the largest cluster. The yellow particles are surface particles, they are not part of the cluster, but do have a nearest neighbor that is.

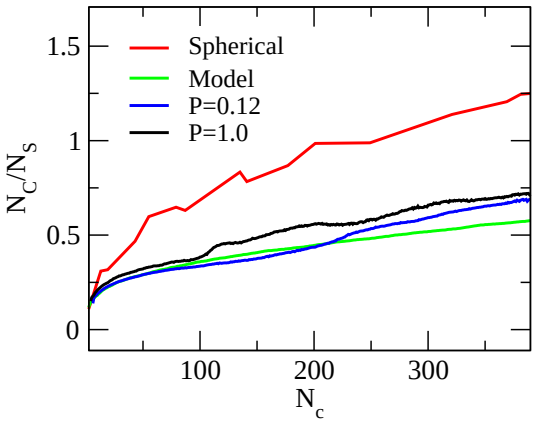

Figure 2.12: The ratio N_c/N_S as a function of the cluster size evaluated for perfect spherical crystal and the average over all clusters observed in the MC simulation.

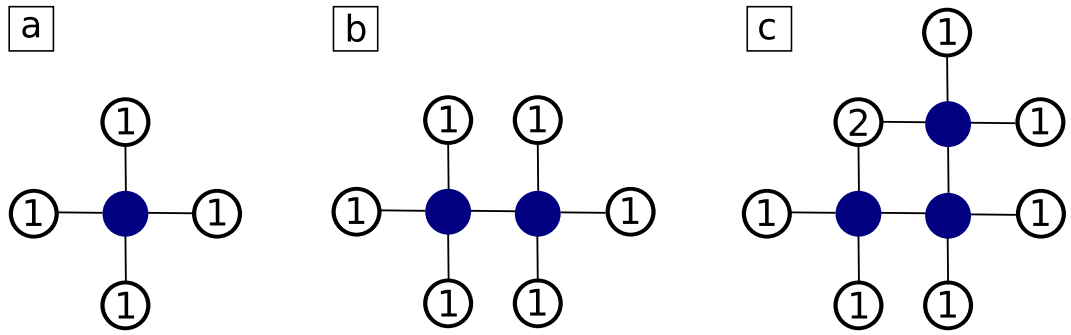

Figure 2.13: Two dimensional sketch used to illustrate the algorithm to generate clusters with a surface that corresponds to that of the clusters observed in the simulations. Blue particles are considered part of the solid cluster. The circles are neighboring particles that make the surface of the cluster. The straight lines indicate bond to these nearest neighbor particles. The numbers in the circles are the numbers of bonds of each of the surface particles.

Chapter 3

Accurate determination of crystal structures based on averaged local bond order parameters

Local bond order parameters based on spherical harmonics, also known as Steinhardt order parameters, are often used to determine crystal structures in molecular simulations. Here we propose a modification of this method in which the complex bond order vectors are averaged over the first neighbor shell of a given particle and the particle itself. As demonstrated using soft particle systems, this averaging procedure considerably improves the accuracy with which different crystal structures can be distinguished.

3.1 Introduction

In computational studies of crystallization from the undercooled liquid one needs to be able to distinguish particles that are part of the crystal from those that belong to the liquid. Ideally, such an assignment should be based on the local environment of the particles only. One method to do that,

which is independent of the specific crystal structure and does not require the definition of a reference frame, is provided by the following algorithm based on spherical harmonics [3]. First, the complex vector $q_{lm}(i)$ of particle i is defined as [22]

$$q_{lm}(i) = \frac{1}{N_b(i)} \sum_{j=1}^{N_b(i)} Y_{lm}(\mathbf{r}_{ij}). \tag{3.1}$$

Here, $N_b(i)$ is the number of nearest neighbors of particle i, l is a free integer parameter and m is an integer that runs from $m = -l$ to $m = +l$. The functions $Y_{lm}(\mathbf{r}_{ij})$ are the spherical harmonics and $\mathbf{r}_{ij}$ is the vector from particle i to particle j. Using the set of complex vectors q_{6m} one can then define the scalar product

$$S_{ij} = \sum_{m=-6}^{6} q_{6m}(i) q_{6m}^{*}(j), \tag{3.2}$$

which measures the correlation between the structures surrounding particles i and j. The $*$ indicates complex conjugation. Two particles i and j are defined to be *connected* if S_{ij} is larger than a given value, typically $S_{ij} > 0.5$. A particle is solid-like if the number of connections it has with its neighbors is above a certain threshold, typically between 6 and 8. If a particle is connected to less particles, it is considered to be liquid-like. Using this criterion to distinguish solid-like from liquid-like particles one can then search for clusters of connected solid-like particles. The size of the largest of these crystalline clusters $\hat{N}$ is often used as a reaction coordinate to follow the progress of the crystallization process. Provided that this reaction coordinate captures the essential physics of the crystal nucleation, the Gibbs free energy $G(\hat{N})$ calculated as a function of $\hat{N}$ provides a means to estimate the rate at which the nucleation of the crystalline phase occurs.

This procedure very efficiently distinguishes between solid-like and liquid-like particles, but does not discriminate between different crystal structures. A set of parameters which hold the information of the local structure are the

local bond order parameters, or Steinhardt order parameters, defined as [22]

$$q_l(i) = \sqrt{\frac{4\pi}{2l+1} \sum_{m=-l}^{l} |q_{lm}(i)|^2}. \tag{3.3}$$

Depending on the choice of l, these parameters are sensitive to different crystal symmetries. Each of them depends on the angles between the vectors to the neighboring particles only and therefore these parameters are independent of a reference frame. Different approaches based on these local bond order parameters were developed to analyze the structure of the crystalline nucleus during the freezing event. Especially q_4 and q_6 are often used as they are a good choice to distinguish between cubic and hexagonal structures [20, 36, 37].

In practice, local bond order parameters are used in different ways. Frenkel and coworkers [2, 18, 20, 38] analyzed the structure of crystalline clusters in terms of order parameter distributions. To do that, they first computed the distributions of q_4 and q_6 for the liquid and for perfect FCC and BCC crystals. Due to thermal fluctuations, these distributions can be rather broad. Then, they determined the distributions of the same order parameters in the crystalline cluster. These distributions are represented as a superposition of the distribution functions of the perfect phases. The superposition coefficients c_{FCC}, c_{BCC} and c_{LIQ}, determinded by mean square minimization, then yield information on the composition of the cluster. For instance, $c_{\mathrm{FCC}} \approx 0.5$, $c_{\mathrm{BCC}} \approx 0.5$,and $c_{\mathrm{LIQ}} \approx 0$ would be indicative of a cluster that is half in the FCC structure and half in the BCC structure.

Another bond order parameter method, used for instance in Ref. [21], defines regions in the two dimensional q_4-q_6-plane and q_4-w_4-plane. The crystalline structure around a given particle is characterized by its positions in

these planes. The parameter w_l necessary for that analysis is defined as

$$w_l(i) = \frac{\sum\limits_{m_1+m_2+m_3=0} \begin{pmatrix} l & l & l \\ m_1 & m_2 & m_3 \end{pmatrix} q_{lm_1}(i) q_{lm_2}(i) q_{lm_3}(i)}{\left(\sum\limits_{m=-l}^{l} |q_{lm}(i)|^2 \right)^{3/2}}. \tag{3.4}$$

Here, the integers m_1, m_2 and m_3 run from $-l$ to $+l$, but only combinations with $m_1 + m_2 + m_3 = 0$ are allowed. The term in brackets is the Wigner 3-j symbol [39]. Using this approach, one can determine the type of crystalline structure occurring around each individual particle.

As mentioned above, thermal fluctuations smear out the order parameter distributions such that it may be difficult to distinguish local crystalline structures based on Steinhardt bond order parameters. In the following we present a simple method to increase the accuracy of the crystal structure determination by averaging over the bond order parameters of nearest neighbor particles. This averaging procedure is discussed in Sec. 3.2 and validated for two different soft sphere systems in Sec. 3.3. Some conclusions are provided in Sec. 3.4.

3.2 Averaged Bond Order Parameters

The crystal structure determination described above can be improved by using the following averaged form of the local bond order parameters:

$$\bar{q}_l(i) = \sqrt{\frac{4\pi}{2l+1} \sum_{m=-l}^{l} |\bar{q}_{lm}(i)|^2}, \tag{3.5}$$

where

$$\bar{q}_{lm}(i) = \frac{1}{\tilde{N}_b(i)} \sum_{k=0}^{\tilde{N}_b(i)} q_{lm}(k). \tag{3.6}$$

Here, the sum from $k = 0$ to $\tilde{N}_b(i)$ runs over all neighbors of particle i plus the particle i itself. Thus, to calculate $\bar{q}_l(i)$ of particle i one uses the local orientational order vectors $q_{lm}(i)$ averaged over particle i and its surroundings. While $q_l(i)$ holds the information of the structure of the first shell around particle i, its averaged version $\bar{q}_l(i)$ also takes into account the second shell. One might say that using the parameter $\bar{q}_l$ instead of q_l increases the accuracy of the distinction of different structures at the price of a coarsening of the spacial resolution. In this sense, the averaged local bond order parameter is similar to the scalar product of Eq. (3.2) used to decide whether a particle is in a solid-like or liquid-like environment. Also in that case the second particle shell is effectively taken into account.
The averaged orientational order parameter $\bar{q}_{lm}$ can also be used to define an averaged version $\bar{w}_l$ of the order parameter w_l,

$$\bar{w}_l(i) = \frac{\sum\limits_{m_1+m_2+m_3=0} \begin{pmatrix} l & l & l \\ m_1 & m_2 & m_3 \end{pmatrix} \bar{q}_{lm_1}(i)\bar{q}_{lm_2}(i)\bar{q}_{lm_3}(i)}{\left(\sum\limits_{m=-l}^{l} |\bar{q}_{lm}(i)|^2 \right)^{3/2}}. \tag{3.7}$$

3.3 Results

In the following, we verify that these averaged forms of the bond order parameters indeed increase the accuracy of the crystal structure determination. The calculations are done for two distinct systems: one in which the particles interact via a Lennard-Jones potential and one in which the interaction is of the Gaussian core form [13, 14, 15].

3.3.1 Lennard-Jones system

For the calculations of the Lennard-Jones system [40] the temperature was $k_\mathrm{B}T = 0.92\epsilon$ and the pressure was $P = 5.68\epsilon\sigma^{-3}$, corresponding to 20% undercooling of the liquid phase [2]. The same conditions were used in Ref. [2] to study homogeneous crystal nucleation. This phase point corresponds

to a mean density of $\rho \simeq 1.05\sigma^{-3}$ in the FCC crystal, which is the most stable phase under these conditions. All simulations were carried out in the isobaric-isothermal ensemble, but calculations at constant volume for the corresponding densities yielded essentially identical results. The particle number was $N = 432$ in the BCC crystal, $N = 864$ in the FCC crystal, and $N = 512$ in the HCP crystal and in the undercooled liquid. Two particles were defined to be neighbors if their distance was smaller than $r_N = 1.4\sigma$.

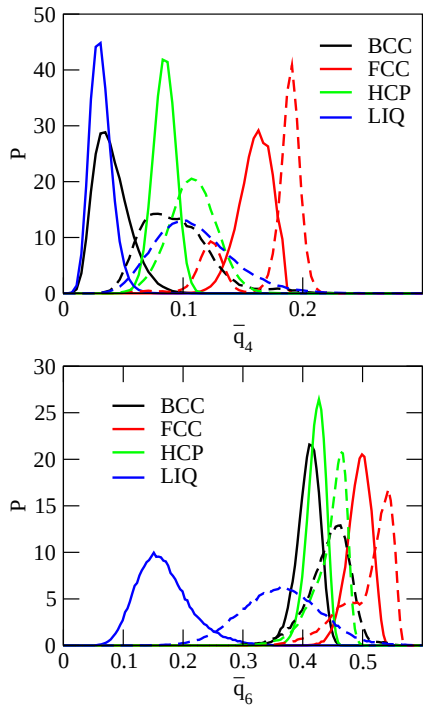

Figure 3.1: Top: Probability distributions of $\bar{q}_4$ (solid lines) and q_4 (dashed lines) for the FCC, BCC and HCP crystals and for the undercooled liquid (LIQ) in the Lennard-Jones system. Bottom: Probability distributions of $\bar{q}_6$ (solid lines) and q_6 (dashed lines) for the same phases.

In Fig. 3.1 we compare the distributions of the local bond order parameters q_4 and q_6 with those of the averaged bond order parameters $\bar{q}_4$ and $\bar{q}_6$. Due to the averaging procedure, the overlap between the distributions decreases considerably thus allowing one to distinguish between different structures more precisely. As can be inferred from Fig. 3.1, the reduced overlap

is due not only to a narrowing of the distributions but also to a shift of the means towards smaller values. While one would expect the order parameter distributions to narrow on the basis of the central limit theorem, one is tempted to attribute the shift of the means to local correlations. To test this speculation, we have artificially eliminated correlations by computing $\bar{q}_l$ from uncorrelated values of q_{lm} generated with the appropriate statistics. Also in this case the narrowing of the distributions was accompanied by a shift of the means indicating that this shift is not due to local correlations between the local order parameters of nearest neighbors but rather originates in the functional form of $\bar{q}_l$.

	q_4	$\bar{q}_4$	q_6	$\bar{q}_6$
BCC	0.089988	0.033406	0.440526	0.408018
FCC	0.170880	0.158180	0.507298	0.491385
HCP	0.107923	0.084052	0.445384	0.421813
LIQ	0.109049	0.031246	0.360012	0.161962

Table 3.1: Mean of the distributions of q_4, $\bar{q}_4$, q_6, and $\bar{q}_6$ for the BCC, FCC, and HCP crystals and the undercooled liquid in the Lennard-Jones system.

	q_4	$\bar{q}_4$	q_6	$\bar{q}_6$
BCC	0.026831	0.010782	0.034791	0.020516
FCC	0.032787	0.014346	0.043301	0.020566
HCP	0.019476	0.009434	0.028992	0.015965
LIQ	0.031992	0.008786	0.066518	0.039360

Table 3.2: Standard deviation of the distributions of q_4, $\bar{q}_4$, q_6, and $\bar{q}_6$ for the BCC, FCC, and HCP crystals and the undercooled liquid in the Lennard-Jones system.

Table 3.1 and Table 3.2 show the mean value and the standard deviation of the distributions of q_4, $\bar{q}_4$, q_6 and $\bar{q}_6$, respectively, for all four phases we studied. The standard deviation decreases by a factor of 2-4 in most cases. To quantify the improvement of the averaged order parameter we define the

overlap between two distributions as

$$O_{\alpha\beta} = \frac{1}{N_{\alpha\beta}} \int P_\alpha(x) P_\beta(x) \mathrm{d}x. \tag{3.8}$$

Here, the indices α and β denote the various crystal structures and $N_{\alpha\beta}$ is given by

$$N_{\alpha\beta} = \sqrt{\int P_\alpha^2(x) \mathrm{d}x \int P_\beta^2(y) \mathrm{d}y}. \tag{3.9}$$

	q_4	$\bar{q}_4$	q_6	$\bar{q}_6$
BCC-FCC	0.124377	0.000000	0.33959496	0.017147
BCC-HCP	0.738776	0.007880	0.94732246	0.866026
BCC-LIQ	0.881215	0.992978	0.46374455	0.000004
FCC-HCP	0.210924	0.000188	0.31311693	0.033288
FCC-LIQ	0.233250	0.000000	0.14914436	0.000000
HCP-LIQ	0.938029	0.001096	0.35744697	0.000000

Table 3.3: Overlap between the distributions of q_4, $\bar{q}_4$, q_6, and $\bar{q}_6$ for the various phases in the Lennard-Jones system.

In Table 3.3 we summarize the overlap between the distributions of q_4, $\bar{q}_4$, q_6, and $\bar{q}_6$ for BCC, FCC, and HCP crystals and the undercooled liquid. In most cases the overlap decreases by several orders of magnitude when going from the local order parameter to the averaged version. One exception are the q_4 distributions of the liquid and the BCC crystal, which have an overlap of nearly 1 even for the averaged order parameter. All phases are, however, resolved very well using two averaged bond order parameters. Figure 3.2 shows a comparison of the various crystalline and liquid phases as scatter plots in the q_4-q_6-plane, the $\bar{q}_4$-$\bar{q}_6$-plane, the q_4-w_4-plane, and the $\bar{w}_4$-$\bar{w}_4$-plane. For the averaged version of the order parameters (right) the four phases separate much better. In practice, the separation between BCC and HCP is the most difficult one. In the $\bar{q}_4$-$\bar{q}_6$-plane these two crystal structures can be distinguished easily and also in the $\bar{q}_4$-$\bar{w}_4$-plane they are well separated. When going from q_4 to $\bar{q}_4$ the overlap between these two structures decreases

by two orders of magnitude (see Tab. 3.3).

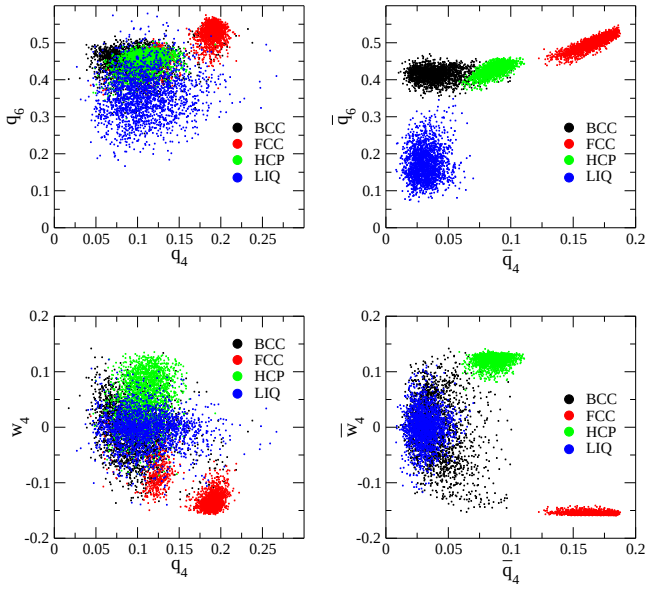

Figure 3.2: Top: Comparison between the q_4-q_6-plane (left) and the $\bar{q}_4$-$\bar{q}_6$-plane (right) for the Lennard-Jones system in three different crystalline structures and in the liquid phase. Each point corresponds to a particular particle, where 2000 points from each structure were chosen randomly. Bottom: q_4-w_4-plane (left) and the $\bar{q}_4$-$\bar{w}_4$-plane (right).

3.3.2 Gaussian Core Model

For the Gaussian core system, in which particles interact via the pair-interaction $v(r) = \varepsilon \exp[-(r/\sigma)^2]$ [13, 14, 15], we chose a temperature of $k_B T = 0.0033\varepsilon$ and pressure $P = 0.011\varepsilon\sigma - 3$ at which the thermodynamically most stable phase is an FCC crystal with density $0.11\sigma^{-3}$. These conditions correspond to the same level of undercooling as that of the Lennard-Jones system described above. All calculations were carried out in the isothermal-isobaric ensemble and the particle numbers for the various crystal structures where the same as in the Lennard-Jones system. The nearest neighbor distance was $r_N = 3.0\sigma$.

Also for the Gaussian core system we find a shift in the mean and a decrease in the width of the distributions (see Fig. 3.3). The mean and the

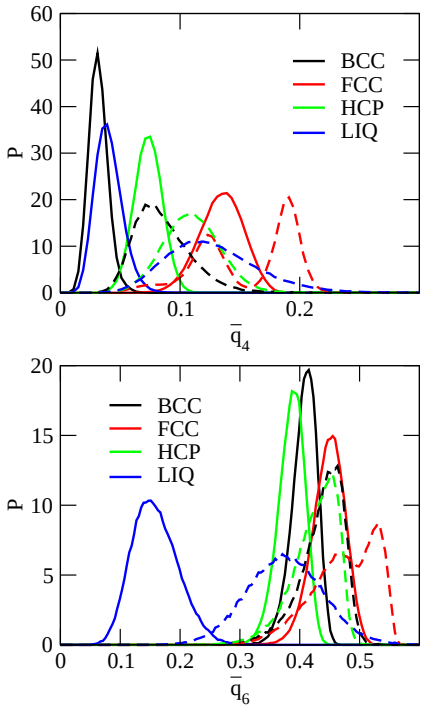

Figure 3.3: Top: Probability distributions of $\bar{q}_4$ (solid lines) and q_4 (dashed lines) for the FCC, BCC and HCP crystals and for the undercooled liquid (LIQ) in the Gaussian core system. Bottom: Probability distributions of $\bar{q}_6$ (solid lines) and q_6 (dashed lines) for the same phases.

standard deviation of the distributions for the various phases are listed in Tables 3.4 and 3.5, respectively. The overlap between the different structures is shown in Table 3.6. In most cases the overlap decreases by a large factor, only the overlap in q_4 between BCC and liquid increases. But as in the Lennard-Jones case all structures can be distinguished very well if two order parameters are taken into account (see Fig. 3.4).

3.4 Conclusions

The averaged bond order parameters proposed in this paper separate different crystal structures more accurately than regular bond order parameters. Instead of using the first shell of surrounding particles only, this method also

	q_4	$\bar{q}_4$	q_6	$\bar{q}_6$
BCC	0.085581	0.031728	0.437129	0.407515
FCC	0.155336	0.134388	0.474079	0.447782
HCP	0.109723	0.073369	0.424627	0.385720
LIQ	0.126950	0.040297	0.375121	0.158913

Table 3.4: Mean of the distributions of q_4, $\bar{q}_4$, q_6, and $\bar{q}_6$ for the BCC, FCC, and HCP crystals and the undercooled liquid in the Gaussian core system.

	q_4	$\bar{q}_4$	q_6	$\bar{q}_6$
BCC	0.023841	0.008024	0.037274	0.021006
FCC	0.039924	0.018200	0.053852	0.027126
HCP	0.023617	0.011605	0.038462	0.022251
LIQ	0.037891	0.011282	0.062874	0.038372

Table 3.5: Standard deviation σ of the distributions of q_4, $\bar{q}_4$, q_6, and $\bar{q}_6$ for the BCC, FCC, and HCP crystals and the undercooled liquid in the Gaussian core system.

takes into account the second shell, just as one usually does when distinguishing between solid-like and liquid-like particles (see Eq. (3.2)). Due to the averaging procedure, the overlap between the order parameter distributions belonging to different phases decreases by up to a few orders of magnitude. The sharper distinction between the different phases is obtained at the cost of a slightly reduced spatial resolution. We demonstrated the enhancement in the crystal structure determination for two systems of soft particles in-

	q_4	$\bar{q}_4$	q_6	$\bar{q}_6$
BCC-FCC	0.248341	0.000007	0.685253	0.462343
BCC-HCP	0.687131	0.015436	0.964792	0.753398
BCC-LIQ	0.619532	0.832443	0.581065	0.000006
FCC-HCP	0.496870	0.022218	0.624299	0.197885
FCC-LIQ	0.632466	0.000261	0.445508	0.000000
HCP-LIQ	0.928871	0.128086	0.682437	0.000018

Table 3.6: Overlap between the distributions of q_4, $\bar{q}_4$, q_6, and $\bar{q}_6$ for the various phases in the Gaussian core system.

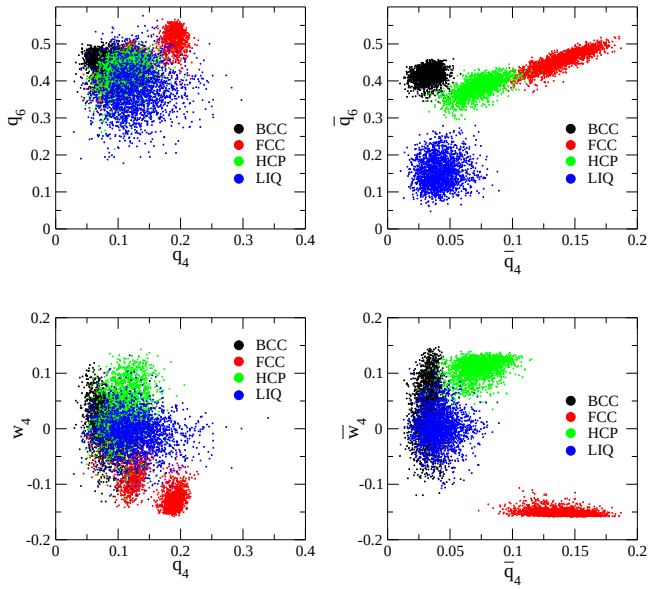

Figure 3.4: Top: Comparison between the q_4-q_6-plane (left) and the $\bar{q}_4$-$\bar{q}_6$-plane (right) in the Gaussian core system . Bottom: q_4-w_4-plane (left) and the $\bar{q}_4$-$\bar{w}_4$-plane (right).

teracting via a Lennard-Jones potential and a Gaussian core potential. For the same degree of undercooling the improvement is similar in both cases. Particularly in the $\bar{q}_4$-$\bar{q}_6$-plane the separation of the liquid phase from the solid phases is pronounced indicating that it might be possible to use this method also to distinguish between liquid and solid particles if only BCC, FCC and HCP structures are expected to be important for the process under study. We expect that the averaging procedure described in this paper lead to similar improvements also for other Steinhardt bond order parameters, e.g., q_8 and w_8.

Part II

Point Defects

Chapter 4

Displacement fields of point defects in two-dimensional colloidal crystals

Point defects such as interstitials, vacancies, and impurities in otherwise perfect crystals induce complex displacement fields that are of long-range nature. In the present paper we study numerically the response of a two-dimensional colloidal crystal on a triangular lattice to the introduction of an interstitial particle. While far from the defect position the resulting displacement field is accurately described by linear elasticity theory, lattice effects dominate in the vicinity of the defect. In comparing the results of particle based simulations with continuum theory, it is crucial to employ corresponding boundary conditions in both cases. For the periodic boundary condition used here, the equations of elasticity theory can be solved in a consistent way with the technique of Ewald summation familiar from the electrostatics of periodically replicated systems of charges and dipoles. Very good agreement of the displacement fields calculated in this way with those determined in particle simulations is observed for distances of more than about 10 lattice constants. Closer to the interstitial, strongly anisotropic displacement fields with exponential behavior can occur for certain defect configurations.

Here we rationalize this behavior with a simple bead-spring that relates the exponential decay constant to the elastic constants of the crystal.

4.1 Introduction

The properties of crystalline substances often crucially depend on the structure and dynamics of imperfections of the crystal lattice. In particular, point defects such as interstitials and vacancies play a pivotal role in determining the stability, transport properties, growth characteristics, and mechanical behavior of materials. Recent impressive experimental advances, such as optical tweezers and confocal microscopy [27, 26], now permit to study the fundamental properties of point defects in condensed matter systems with "atomistic" space and time resolution.

Recently, a number of experimental studies have focused on the structure and dynamics of point defects in two-dimensional assemblies of micrometer sized colloidal particles [41, 42, 43] and, in particular, on their effective interactions [44, 28, 45]. In studying such defect interactions the question arises to which degree they can be rationalized in terms of continuum elastic theory. As a first step towards answering this question, in this article we investigate numerically the disturbances caused by isolated interstitial particles and compare the results with the predictions of continuum theory. In carrying out such a comparison, it proves crucial that in solving the equations of elasticity theory boundary conditions are used that match those of the simulations. For the periodic boundary conditions usually applied in computer simulations, the displacement fields of single defects can be determined using the technique of Ewald summation familiar from electrostatics [46, 47]. While elasticity theory properly describes the disturbances and interactions created by lattice imperfections on a larger scale, discrete lattice effects dominate on spatial scales of the order of few lattice constants.

The remainder of this paper is organizes as follows. In Sec. 4.2 we define the model and describe the numerical methods. The treatment of point

defects in a two-dimensional elastic continuum is discussed in Sec. 4.3 and comparison with the numerical results is discussed in Sec. 4.4. For certain defect configurations one observes an exponential rather than algebraic decay of the displacement fields. This behavior can be understood in terms of a simple bead-spring model introduced in Sec. 4.5 with parameters related to the elastic constants of the material. Some concluding remarks are provided in Sec. 4.6.

4.2 Simulations

In this paper we study a two-dimensional crystal of soft particle interacting via the Gaussian potential [13, 14, 15]

$$v(r) = \epsilon \exp(-r^2/\sigma^2), \tag{4.1}$$

where r is the inter-particle distance and ϵ and σ set the energy and length scales, respectively. In the following, energies are measured in units of ϵ and distances in units of σ. This so-called Gaussian core model, used here as a generic model for a system of soft spheres, is a realistic description for the short-ranged effective interactions between polymer coils in solution [32]. In three dimensions, the Gaussian core model can exist as a fluid, a bcc- and an fcc-solid depending on temperature and density [14]. In two dimensions, the perfect triangular lattice is the lowest energy structure of Gaussian core particles at all densities [48]. Computer simulations indicate that also in this system of purely repulsive particles point defects such as interstitials, vacancies or impurity particles of different size display attractive (as well as repulsive) interactions both in two and three dimensions [49].

To study the displacement field of a single interstitial numerically, we prepare a configuration of particles arranged on the sites of a perfect lattice configuration and insert an extra particle of the same species. After insertion, the system is relaxed to a new minimum energy configuration by steepest descent minimization, i.e., we study the defect structure at $T = 0$. Typically,

70.000 steepest descent steps are carried out. The system we study here consists of $N = 199.680$ Gaussian core particles (without the extra particle) at a number density of $\rho = 0.6\sigma^{-2}$ corresponding to a lattice constant $a = (2/\sqrt{3}\rho)^{1/2} = 1.3872\sigma$. Periodic boundary conditions apply to the simulation box of length $L_x = 416a$ and height $L_y = (\sqrt{3}/2)480\,a = 415.692a$. The aspect ratio of the almost square simulation box is $L_y/L_x = 0.99926$.

We quantify the perturbation caused by the defect in terms of the displacement field [50]

$$\mathbf{u}(\mathbf{r}_i) \equiv \mathbf{r}'_i - \mathbf{r}_i. \tag{4.2}$$

Here, $\mathbf{r}'_i$ and $\mathbf{r}_i$ denote the position of particle i with and without the defect, respectively. As we will see in the following sections, simple point defects generate remarkably intricate displacement patterns that can be understood in terms of elasticity theory only on large length scales.

At $T = 0$, the elastic constants describing the macroscopic response of the system to perturbations can be calculated as a function of density from simple lattice sums. For a density of $\rho = 0.6\sigma^2$, the Lamé coefficients (see Sec. 4.3) of the perfect triangular lattice have values $\lambda = 1.1487\,\epsilon\sigma^{-2}$ and $\mu = 0.06018\,\epsilon\sigma^{-2}$. At this density, the pressure is $p = 0.5442\,\epsilon\sigma$ and the energy density is $e = 0.2691\,\epsilon\sigma^{-2}$ corresponding to an energy per particle of $E/N = 0.4485\epsilon$. The bulk modulus, which in two dimensions is related to the the Lamé coefficients by $K = \lambda + \mu$, has a value of $K = 1.2089\epsilon\sigma^{-2}$.

4.3 Elasticity Theory

While close to a point defect the displacement field is highly anisotropic and strongly dependent on the atomistic details of the interactions, for large distances elasticity theory is expected to be valid. The differential equations describing the equilibrium of an elastic continuum are usually expressed in terms of the strain tensor [50]

$$\epsilon_{ij}(\mathbf{r}) = \frac{1}{2}\left(\frac{\partial u_i}{\partial r_j} + \frac{\partial u_j}{\partial r_i}\right), \tag{4.3}$$

where u_i denotes the i-component of the displacement $\mathbf{u}$ and r_i the i-th component of the position $\mathbf{r}$. For a given external volume force $\mathbf{f}(\mathbf{r})$ with components f_i acting on an isotropic system such as a crystal on a triangular lattice, Hook's law leads to the equilibrium condition for the strain:

$$\lambda \frac{\partial}{\partial r_i} \epsilon_{kk} + 2\mu \frac{\partial \epsilon_{ij}}{\partial r_j} + f_i = 0. \tag{4.4}$$

Here, λ and μ are the so-called Lamé coefficients and summation over repeated indices is implied. Solving this equation for a singular force yields the Green's function from which the response of the elastic continuum to an arbitrary force can be obtained by integration.

To model the displacement field caused by the introduction of point defects using linear continuum elasticity theory, we determine the displacement field caused by two pairs of opposing forces, one pair acting along the x-axis and the other one along the y-axis [51, 52, 53]. This idealized model of a defect is equivalent to inserting a small circular inclusion into a hole of different size [52]. Each force of this pair is of equal magnitude F but with opposite sign acting on two points separated by a small distance h. Such a force pair exerts a zero net force on the material. In the limit $h \to 0$ where the force $F \to \infty$ in a way such that Fh remains constant, the equilibrium condition for the displacement can be written as

$$(\lambda + 2\mu) \frac{\partial u_j}{\partial r_j} = Fh\delta(\mathbf{r}). \tag{4.5}$$

Assuming that the displacement can be written as the derivative of a potential,

$$u_i = \frac{\partial \phi}{\partial r_i} \tag{4.6}$$

one obtains

$$\Delta \left(-\frac{\lambda + 2\mu}{Fh} \phi \right) = -\delta(\mathbf{r}). \tag{4.7}$$

This equation is the Poisson equation of electrostatics with a singular disturbance. Since, as noted above, $K(\mathrm{r}) = -\ln(r)/2\pi$ is a solution of $\Delta K = -\delta(\mathbf{r})$

(see, for instance, Ref. [54]), we obtain the Green's function

$$\phi(r) = \frac{Fh}{2\pi(\lambda + 2\mu)} \ln(r) \tag{4.8}$$

from which the displacement field $\mathbf{u}(\mathbf{r})$ follows by differentiation according to Equ. (4.6),

$$u_i = \frac{Fh}{2\pi(\lambda + 2\mu)} \frac{r_i}{r^2}. \tag{4.9}$$

In comparing the results of particle simulations with those of elasticity theory it is important to realize that the displacement fields predicted by continuum theory are of a long-range nature. Therefore, it is crucial that corresponding boundary conditions are used in both cases. All simulations discussed in this paper are done with periodic boundary conditions in order to minimize surface effects and preserve the translational invariance of the perfect lattice. Hence, also the continuum calculations need to be carried out with periodic boundary conditions.

Since the defect fields for the infinite material are long-ranged, the displacement field in the periodic system cannot be obtained by simply summing up the contributions of the periodic images. In fact, such a naive summation of the contribution of all image defects diverges. A more appropriate treatment that avoids this problem consists in determining the Green's function of the Poisson equation (4.7) for periodic boundary conditions. In this case, the solution of this equation in two dimensions, known from electrostatics [46, 47], can be written as Ewald sum of a logarithmic potential embedded in a neutralizing background,

$$\begin{aligned} \phi(\mathbf{r}) \;=\; & \frac{Fh}{2\pi(\lambda + 2\mu)} \left\{ \frac{1}{2} \sum_{\mathbf{l}} E_i[-\eta^2 |\mathbf{r} + \mathbf{l}|^2] \right. \\ & \left. - \frac{2\pi}{A} \sum_{\mathbf{k} \neq 0} \frac{e^{-k^2/4\eta^2}}{k^2} \cos(\mathbf{k} \cdot \mathbf{r}) + \frac{\pi}{2\eta^2 A} \right\}. \end{aligned} \tag{4.10}$$

Here, $E_i(x) = \int_{-\infty}^{x} (e^t/t)\, dt$ is the exponential integral. The first sum is over

all lattice vectors $\mathbf{l}$ in real space and the second sum is over all reciprocal vectors $\mathbf{k}$ in Fourier space. The adjustable parameter η, set to a value of $\eta = 6/L_x$ here, determines the rate of convergence of the two sums and A is the area of the rectangular simulation cell. The Fourier space sum can be evaluated accurately using about 2,500 reciprocal space vectors. From Equ. (4.10) for the scalar function $\phi(\mathbf{r})$ the displacement field of a point defect in a system with periodic boundary conditions is found by differentiation,

$$u_i(\mathbf{r}) = \frac{Fh}{2\pi(\lambda+2\mu)} \left\{ \sum_{\mathbf{l}} e^{-\eta^2|\mathbf{r}+\mathbf{l}|^2} \frac{r_i + l_i}{|\mathbf{r}+\mathbf{l}|^2} + \frac{2\pi}{A} \sum_{\mathbf{k}\neq 0} \frac{e^{-k^2/4\eta^2}}{k^2} k_i \sin(\mathbf{k}\cdot\mathbf{r}) \right\}. \quad (4.11)$$

For the systems considered in this paper, the real space sum may be truncated after the first term. Since the value of $Fh/2\pi(\lambda+2\mu)$ is undetermined, the parameter $\gamma \equiv Fh/2\pi(\lambda+2\mu)$ is treated as a fit parameter in the following. The Ewald sums of the above equations describe the effects of "image defects" at the center of the periodically replicated domains.

4.4 Results

First, we study the displacement field of a single interstitial. To generate such a defect, we insert an extra particle of the same species into a perfect 2d-crystal on a triangular lattice. After insertion, the system is relaxed to a new minimum energy configuration by steepest descent minimization, i.e., we study the defect structure at $T = 0$. Typically, 70.000 steepest descent steps are carried out. In each step each particle is moved in the direction of the force acting on the particle where the absolute value of the displacement in chosen to be small enough to ensure that the energy of the system decreases in each step.

The extra particle can deform the crystal in different ways [42] and produces displacement fields of different symmetries (see Fig. 4.1). In one

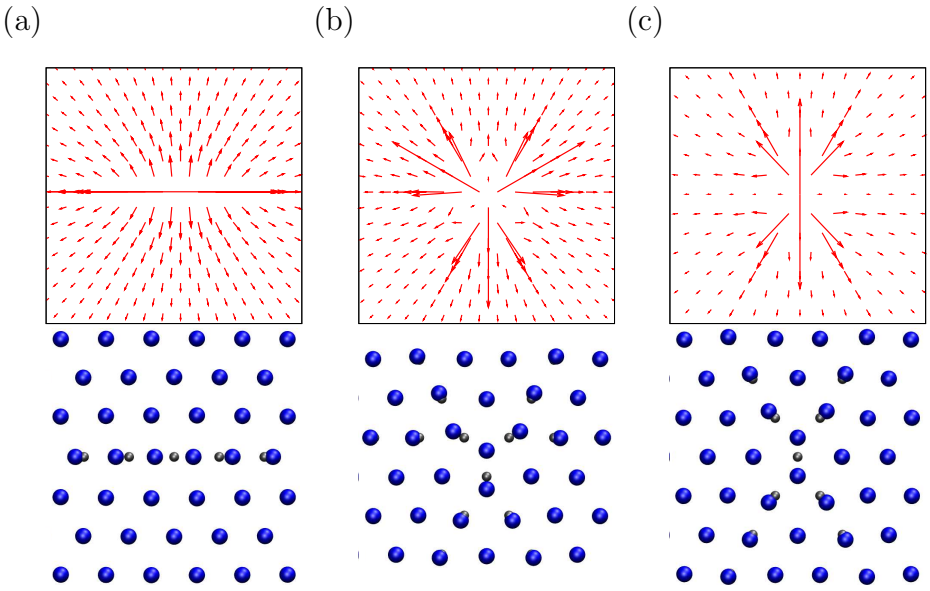

Figure 4.1: Displacement fields (top) and local defect configurations (bottom) for the I_2 (a), the I_3 (b) and the I_d (c) configurations. The length of the arrows representing the displacements of the particles from their position in the perfect lattice are exaggerated for better visibility. In the figures at the bottom the blue spheres represent the particles and the small gray spheres indicate the position of the lattice sites of the perfect crystal.

configuration, called I_2 interstitial or crowdion and shown in Fig. 4.1a, the additional particle pushes one particular particle of the crystal out of its equilibrium position. Both the original particle and the additional particle arrange themselves at equal distance around the lattice position of the original particle. The displacement pattern arising for this type of interstitial has two-fold symmetry and, of course, occurs in all three low-index lattice directions with equal probability. One may suspect that this defect configuration, with a symmetry that differs from the symmetry of the underlying triangular lattice, is caused by the rectangular periodic boundary conditions that are applied to the system. To rule out this possibility, we have repeated the calculation with hexagonal periodic boundary conditions obtaining the same result.

Another low-energy defect configuration is the I_3 interstitial with three-fold symmetry (see Fig. 4.1b). In this case the interstitial particle is located

at the center of a basic lattice triangle and pushes its neighbors outward from their original positions. A third important interstitial configuration is the I_d interstitial or dumbbell interstitial shown in Fig. 4.1c. In the 2d Gaussian-core model under the conditions studied here the I_2 pattern has a slightly lower energy than the I_3 interstitial and the I_d interstitial. The energy difference between a I_2 and a I_3 interstitial is 0.000674ϵ and the difference between I_2 and I_d is 0.000665ϵ. All three displacement patterns are important for the diffusion of interstitials. An I_2 interstitial is very mobile in the direction of its main axis. The I_3 and I_d forms are visited as intermediate configurations when the I_2 interstitial changes the orientation of its main axis and hence its direction of motion [55].

Next, we compare the displacement fields determined numerically with the predictions of elasticity theory. In particular, we verify to which extent the $1/r$-behavior modulated by the periodic boundary conditions and embodied in Equ. (4.11) is realized in the particle system. The complex displacement patterns of the various interstitial configurations shown in Fig. 4.1 obviously differ from this expectation, at least near the defect, and indicate that continuum theory is not applicable in this region. Far away from the defect, however, the perturbation caused by the defect is small and the response of the material should be described accurately by linear elasticity theory.

The magnitude $|\mathbf{u}(\mathbf{r})|$ of the displacement vector $\mathbf{u}(\mathbf{r})$ is shown as a function of the distance from the interstitial in Fig. 4.2 for the I_2 defect configuration. Each point in the figure corresponds to one individual particle. For short distances, the displacement magnitude is not a unique function of the distance r reflecting the anisotropic nature of the defect. For larger distances, however, the displacement magnitude is mostly determined by the distance r. Eventually, however, the periodic boundary conditions lead to a spread of the displacement magnitude for even larger distances and a splitting into two branches corresponding to the x- and y-directions and the directions along the diagonals, respectively. In the regime where $\mathbf{u}(\mathbf{r})$ behaves isotropically,

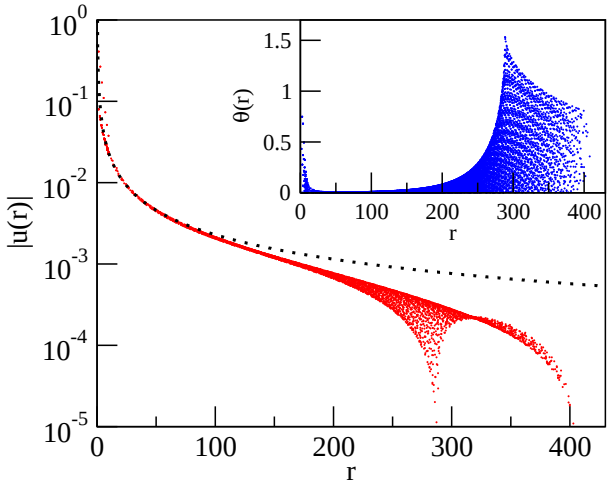

Figure 4.2: Displacement magnitude $|\mathbf{u}(\mathbf{r})|$ as a function of distance from the defect r for the I_2 interstitial. Each red dot corresponds to one particle. The solid line represents the γ/r behavior. Here, $\gamma = 0.2291\sigma^2$ was used as this value yields the best fit of the results obtained vie Ewald summation to the results of the particle simulations in the far field. Inset: angle θ between the displacement vector $\mathbf{u}$ the position vectors $\mathbf{r}$ as a function of the distance r from the defect site.

the displacement follows the approximately $1/r$-form predicted by elasticity theory for a point defect in an infinitely extended medium. The orientation of the displacement vector $\mathbf{u}(\mathbf{r})$, depicted in the inset of Fig. 4.2, behaves in an analogous way. The angle θ between $\mathbf{u}(\mathbf{r})$ and the position vector $\mathbf{r}$, shown as a function of the distance r from the defect, is not a unique function of r near the defect. For larger r, θ vanishes indicating that in this distance regime the displacement vector points straight away from the defect. At even larger distances, the periodic boundary conditions imposed on the system eventually cause the angle θ to spread again.

The displacement fields calculated according to Equ. (4.11) and numerically for an interstitial in the I_2 configuration are compared in Fig.4.3. In this figure, the displacement components u_x and u_y are depicted as a function of the distance from the defect along the x-axis and y-axis, respectively. The prediction of continuum theory, calculated using the Ewald summation of Equ. (4.11), agrees well with the displacement field of the particle system

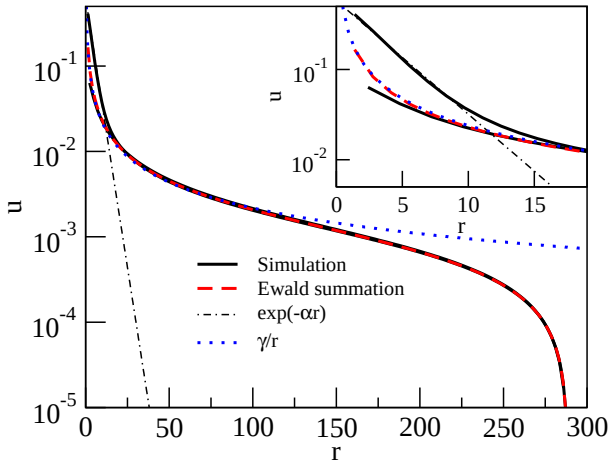

Figure 4.3: Displacement components u_x and u_y of the I_2 interstitial as s function the of the distance along the x-axis and y-axis, respectively (solid lines). Here, the direction of largest displacement of the I_2 defect is oriented in x-direction. Also plotted is the displacement computed from continuum theory according to Equ. (4.11) (dashed line), simple $1/r$-behavior (dotted line) and the displacement obtained for the simple mechanical model described in the main text (dash-dotted line). The inset shows the region close to the defect location. As in Fig. 4.2 a defect strength of $\gamma = 0.2291\sigma^2$ was used for the evaluation of the displacement from elasticity theory.

for distances larger than about 10 lattice constants.

4.5 Harmonic Model

Near the defect, the predictions of continuum theory differ from the simulation results. The deviation is particularly pronounced in the direction of the main axis of distortion of the I_2 defect, in which the displacement appears to decay exponentially up to a distance of about $\approx 10\,a$. This unexpected exponential behavior can be understood in terms of a simple model with harmonic interactions. This model consists of a one-dimensional chain of particles in which each particle is connected to its two neighbors with springs of force constant k_1 (except the first and last particle, which are coupled only to their neighbors on the right and left, respectively). In addition, each particle is

attached to a fixed lattice position with another spring of force constant k_2. The Hamiltonian of this system is

$$\mathcal{H} = \frac{k_1}{2}\sum_{j=0}^{N}(x_{j+1} - x_j - b)^2 + \frac{k_2}{2}\sum_{j=0}^{N+1}(x_j - bj)^2, \tag{4.12}$$

where $N+2$ is the number of particles, x_j is the position of particle j and b is the equilibrium distance between two neighboring particles. In the minimum energy configuration of this chain, the particles are arranged such that $x_j = jb$. We now imagine that particle 0 is pushed to the right by a distance of u_0 while particle $N+1$ is kept fixed at $x_{N+1} = (N+1)b$. If the system is then relaxed to a new energy minimum, all other particles will be displaced from their original positions too. For this simple model, the response of the system to the displacement of the first particle can be calculated analytically by direct matrix inversion (see 4.7). In the large N limit, one finds that the displacement of the particles from their original position decays exponentially with their position,

$$u_j = u_0 \exp(-\alpha j), \tag{4.13}$$

where u_j is the displacement of particle j due to the forced displacement u_0 of the first particle. The decay constant α is related to the force constants of the model by

$$\alpha = \cosh^{-1}\left(1 + \frac{k_2}{2k_1}\right). \tag{4.14}$$

To compare the prediction of this simple model with the simulation results we have to determine the force constants k_1 and k_2 felt by the particles in the main axis of the defect. While the force constant k_1 arises from interactions within this main axis, the force constant k_2 is related to interactions of the particles in the main axis with those from adjacent rows. Accordingly, we determine k_1 by calculating numerically the energy change caused by slightly displacing one single particle in a one-dimensional row of otherwise fixed Gaussian core particles without the presence of the neighboring rows. The distance of the particles in the row is chosen to be equal to the

lattice constant at the density $\rho = 0.6\sigma^{-2}$ considered throughout the paper. From the energy as a function of the displacement one obtains a force constant of $k_1 = 0.015\epsilon/\sigma^2$. To determine the force constant k_2 we calculate the energy change caused by translating a whole row of particles in the perfect crystal. The particles in the row are fixed with respect to each other and the remaining particles are kept at their lattice positions. From the energy change per moved particle a force constant of $k_2 = 0.0013\epsilon/\sigma^2$ follows. The decay constant of $\alpha = 0.29$ calculated according to Equ. (4.14) with these force constants is in perfect agreement with the computer simulation results shown in Fig. 4.3.

For a system in which only nearest neighbor interactions are important, the force constants k_1 and k_2 can be simply related to the bulk modulus K and the shear modulus μ. Then, the force constant k_1 is given by

$$k_1 = 2v''(a), \tag{4.15}$$

where $v(a)$ is the pair potential at distance a. Since in this case the elastic moduli are given by

$$K = \frac{\sqrt{3}}{2}\left\{v''(a) - \frac{v(a)}{a}\right\} \tag{4.16}$$

and

$$\mu = \frac{\sqrt{3}}{4}\left\{v''(a) + 3\frac{v(a)}{a}\right\} \tag{4.17}$$

one obtains

$$k_1 = \frac{2}{\sqrt{3}}\left(\mu + \frac{3K}{2}\right). \tag{4.18}$$

To the extent that the response of the system to shear is determined by the interaction of neighboring parallel rows of particles, the energy density caused by shifting a whole row of atoms between two fixed ones is the same as that of a shear of appropriate magnitude. Accordingly, the force constant k_2 is related to the shear modulus by

$$k_2 = \frac{4}{\sqrt{3}}\mu. \tag{4.19}$$

This expression remains also valid if interactions beyond nearest neighbors are included between adjacent rows of particles. In terms of the elastic constants, the constant α describing the exponential decay of the displacement field along the principal axis can be expressed as

$$\alpha = \cosh^{-1}\left(1 + \frac{2\mu}{2\mu + 3K}\right), \tag{4.20}$$

or, in terms of the Poisson ratio ν,

$$\alpha = \cosh^{-1}\left(\frac{7-\nu}{5+\nu}\right). \tag{4.21}$$

For a density of $\rho = 0.6\sigma^{-2}$, inserting the Poisson ratio of $\nu = 0.905151$ determined from a simple lattice sum yields $\alpha \approx 0.25$, only slightly different from the correct value $\alpha \approx 0.29$. This deviation occurs, because in the Gaussian core model at the density $\rho = 0.6\sigma^{-2}$ interactions between non-nearest neighbor particles are important in determining the elastic constants (in fact, considering only nearest neighbors would produce a negative shearing modulus μ in this case). For systems, in which only nearest neighbor interactions are relevant, the above expression is expected to hold accurately.

4.6 Conclusion

Point defects in two-dimensional crystals, such as interstitials and vacancies, can assume configurations with symmetries that vary from the symmetry of the underlying triangular lattice. While close to the defect the displacement field is highly anisotropic and strongly dependent on the atomistic details of the interactions, for large distances elasticity theory, which predicts isotropic behavior, is valid. For the particular I_2 interstitial configuration, the displacement decreases exponentially with distance along the main defect axis. The decay constant is simply related to the material properties via the Poisson ratio, which measures the ratio between transversal and axial strain

upon stretching. In comparing the displacement fields computed from particles simulations with those obtained with continuum elasticity theory it is crucial to use equivalent boundary conditions in both cases. Since particle simulations are usually carried out with periodic boundary conditions, also the differential equations of elasticity theory need to be solved for a periodic system. We have shown here that Ewald summation, a technique routinely used in computer simulations to determine the electrostatic interactions of charges and dipoles, can be used for this purpose. In this method the sum over all interactions with periodic image defects is split into two sums in real space and reciprocal space, respectively. This particular treatment of the long-ranged nature of displacement fields effectively introduces a neutralizing background that leads to convergent sums. Note that exactly the same expression apply also to a system that is enclosed in a rigid container. Outside a core region near the defect, displacement patterns determined using such Ewald summation agree perfectly with those calculated in particle simulations.

4.7 Springmodel

In this appendix we calculate the response at $T = 0$ of the one-dimensional bead-spring model of Sec. 4.5 to a forced displacement of the first particle in the chain. The potential energy of the $N + 2$ particles, located at positions x_j, is given by

$$\mathcal{H}(x) = \frac{k_1}{2}\sum_{j=0}^{N}(x_{j+1} - x_j - b)^2 + \frac{k_2}{2}\sum_{j=0}^{N+1}(x_j - bj)^2, \tag{4.22}$$

where b is the equilibrium distance and k_1 and k_2 are force constants. The vector $x = x_0, x_1, \cdots, x_{N+1}$ includes the positions of all particles. Minimizing the potential energy with respect to the particle positions x_j by requiring that

$$\left.\frac{\partial \mathcal{H}(x)}{\partial x_j}\right|_{x=\overline{x}} = 0 \tag{4.23}$$

for all j, one finds that at the potential energy minimum the particle positions are $\overline{x}_j = bj$. We now displace particle 0 by an amount u_0 from its original position $\overline{x}_0 = 0$ and keep particle $N + 1$ fixed at position $(N + 1)b$. If we hold particle 0 at this new position while minimizing the potential energy, all particles from 1 to N will move to new equilibrium positions. Thus, the minimum energy configuration of the system is a function of the displacement u_0 of particle 0, which may be viewed as a parameter that is controlled externally and perturbs the system. To make this distinction between the displacement of particle 0 and that of all other particles more explicit, we denote u_0 with an extra symbol, $\xi = u_0$. The displacement u_j of the particles $j = 1, \cdots, N$ is then a function of ξ,

$$u_j(\xi) = \overline{x}_j(\xi) - \overline{x}_j(0), \tag{4.24}$$

where $\overline{x}_j(\xi)$ and $\overline{x}_j(0)$ denote the particle position in the minimum energy configuration with and without perturbation, respectively. In the following, we will calculate the displacements $u_j(\xi)$ as a function of the perturbation

strength ξ.

Since condition (4.23) defines the position of the energy minimum as a function of the perturbation strength ξ, its derivative with respect to ξ must vanish,

$$\frac{d}{d\xi}\left(\left.\frac{\partial\mathcal{H}(\xi)}{\partial x_j}\right|_{x=\overline{x}(\xi)}\right)=0. \tag{4.25}$$

Application of the chain rule then leads to

$$\sum_j\left(\left.\frac{\partial^2\mathcal{H}}{\partial x_j\partial x_i}\right|_{x=\overline{x}(\xi)}\right)\frac{\partial\overline{x}_j(\xi)}{\partial\xi}+\left.\frac{\partial^2\mathcal{H}}{\partial\xi\partial x_i}\right|_{x=\overline{x}(\xi)}=0. \tag{4.26}$$

This condition must hold for all i. Defining

$$z_j \equiv \frac{\partial\overline{x}_j(\xi)}{\partial\xi}, \tag{4.27}$$

$$\mathcal{H}_{ij} \equiv -\left.\frac{\partial^2\mathcal{H}}{\partial x_j\partial x_i}\right|_{x=\overline{x}(\xi)}, \tag{4.28}$$

$$\tag{4.29}$$

and

$$y_i \equiv \left.\frac{\partial^2\mathcal{H}}{\partial\xi\partial x_i}\right|_{x=\overline{x}(\xi)}, \tag{4.30}$$

we can rewrite Equ. (4.26) as

$$y_i=\sum_j\mathcal{H}_{ij}z_j. \tag{4.31}$$

Inversion of the matrix $\mathcal{H}_{ij}$ then yields the vector z,

$$z_i=\sum_j\mathcal{H}^{-1}_{ij}y_j. \tag{4.32}$$

Once $z_j=\partial\overline{x}_j(\xi)/\partial\xi$ is known, $\overline{x}_j(\xi)$ can be obtained by integration.

For the bead-spring model considered here, the first and second deriva-

tives of the potential energy with respect to the particle coordinates are given by

$$\frac{\partial \mathcal{H}}{\partial x_i} = (2k_1 + k_2)x_i - k_1 x_{i+1} - k_1 x_{i-1} - k_2 bi, \tag{4.33}$$

$$\frac{\partial \mathcal{H}}{\partial x_i \partial x_j} = \begin{cases} 2k_1 + k_2 & \text{if } i = j, \\ -k_1 & \text{if } j = i+1 \text{ or } j = i-1, \\ 0 & \text{else,} \end{cases} \tag{4.34}$$

and

$$\frac{\partial \mathcal{H}}{\partial x_i \partial \xi} = \begin{cases} -k_1 & \text{if } i = 1, \\ 0 & \text{if } i > 0. \end{cases} \tag{4.35}$$

To solve Equ. (4.32) we have to invert the symmetric tridiagonal matrix H_{ij}. For this particular matrix, the inverse matrix is known analytically [56],

$$\begin{aligned} \mathcal{H}_{ij}^{-1} &= -\frac{1}{2k_1}\left\{ \frac{\cosh[(N+1-|j-i|)\alpha]}{\sinh(\alpha)\sinh[(N+1)\alpha]} \right. \\ &\qquad \left. -\frac{\cosh[(N+1-i-j)\alpha]}{\sinh(\alpha)\sinh[(N+1)\alpha]} \right\}, \end{aligned} \tag{4.36}$$

where

$$\alpha = \cosh^{-1}\left(1 + \frac{k_2}{2k_1}\right) \tag{4.37}$$

Since for our model $y = \{-k_1, 0, 0, \cdots, 0\}$, we obtain

$$\frac{\partial \overline{x}_i}{\partial \xi} = \sum_j H_{ij}^{-1} y_j = -H_{i0}^{-1} k_1. \tag{4.38}$$

and hence

$$\frac{\partial \overline{x}_i}{\partial \xi} = \frac{\cosh[(N+2-i)\alpha] - \cosh[(N-i)\alpha]}{2\sinh(\alpha)\sinh[(N+1)\alpha]}. \tag{4.39}$$

For large N, this equation simplifies to

$$\frac{\partial \overline{x}_i}{\partial \xi} = \exp(-i\alpha). \tag{4.40}$$

Integration with respect to ξ then yields

$$\overline{x}_i(\xi) = \xi \exp(-i\alpha) + C_i, \tag{4.41}$$

where the integration constant is given by $C_i = \overline{x}_i(0)$. Thus, the displacement of particle j is proportional to the displacement of particle 0 and decays exponentially with the distance from the origin,

$$u_i = u_0 \exp(-i\alpha), \tag{4.42}$$

with a decay constant α that depends on the force constants k_1 and k_2 only.

Chapter 5

Point defects in two-dimensional colloidal crystals: simulation vs. elasticity theory

Using numerical and analytical calculations we study the structure of vacancies and interstitials in two-dimensional colloidal crystals. In particular, we compare the displacement fields of the defect obtained numerically with the predictions of continuum elasticity theory for a simple defect model. In such a comparison it is of crucial importance to employ corresponding boundary conditions both in the particle and in the continuum calculations. Here, we formulate the continuum problem in a way that makes it analogous to the electrostatics problem of finding the potential of a point charge in periodic boundary conditions. The continuum calculations can then be carried out using the technique of Ewald summation. For interstitials, the displacement fields predicted by elasticity theory are accurate at large distances, but large deviations occur near the defect for distances of up to 10 lattice spacings. For vacancies, the elasticity theory predictions obtained for the simple model do not reproduce the numerical results even far away from the defect.

5.1 Introduction

Many properties of crystalline materials are strongly affected by the presence of imperfections in the crystal lattice. In particular, point defects such as vacancies and self interstitials have a profound influence on the mechanical, optical, and electrical behavior of the material. Recent advances in experimental techniques for the manipulation and observation of colloidal systems [27, 26] now permit to study the fundamental properties of point defects in condensed matter systems with "atomistic" space and time resolution. Using optical tweezers to manipulate individual colloidal particles, Pertsinidis and Ling [41, 42, 43] have generated point defects in two-dimensional crystals and have studied their stable structures, interactions and diffusion. In other experimental work, Maret, Grünberg and collaborators [44, 28, 45] have investigated the effective interactions of thermally excited topological defects in crystals of paramagnetic colloidal particles and discussed the significance of these interactions for 2d-melting, which according to the celebrated Kosterlitz-Thouless-Halperin-Nelson-Young theory [29], involves the formation and dissociation of topological defect pairs. Point defects also play an important role in the two-dimensional electron lattice, the so called Wigner crystal [57], in which they carry implication for the melting mechanism [58, 59, 60], and for the the conjectured supersolid phase of Helium 4 [61], in which case the attractive interactions of vacancies and interstitial may lead to expulsion of defects from the crystal thus preventing formation of a supersolid [23].

From experiments [41, 42, 43] and computer simulations [55, 24] it is known that vacancies and interstitials in 2d colloidal crystals can occur in various stable configurations with symmetries that differ from the symmetry of the underlying lattice. In the present article we study the structure and energetics of such point defects in a 2d crystal of soft spheres using computer simulations and analytical calculations. In particular, we address the question of how accurately the disturbances created by point defects can be rationalized in terms of elastic continuum theory. Due to the long range

nature of elastic displacement fields, in carrying out such a comparison it is critical to use corresponding boundary conditions in the particle and continuum calculation. Similar periodic image effects due to elastic interactions need to be taken into account also in the atomistic modeling of dislocations [62, 63]. As we show below, the structure of point defects in a system with periodic boundary conditions can be determined within elasticity theory with the technique of Ewald summation familiar from the computer simulation of systems with electrostatic interactions [35]. This technique has been used before to adapt the interaction of dislocations to periodic boundary conditions [57, 64, 65]. Here we use Ewald summation to solve the equilibrium condition of elasticity theory and calculate the displacement field of a simple point defect model under periodic boundary conditions. While elasticity theory accurately describes the lattice distortion caused by point defects in the far field, non-linearities and discrete lattice effects dominate the defect structure near the defect.

Although all the numerical studies discussed in this paper are carried out for two-dimensional crystals of soft spheres, simulations performed for three-dimensional crystals of various structures and with different interaction potentials, including Gaussian core, Lennard-Jones, screened electrostatic, and $1/r^3$-interactions, indicate that the phenomena described here are common to many atomic and colloidal systems.

The remainder of the paper is organized as follows. In Sec. 5.2 we describe how we determine the displacement fields of point defects numerically, discuss whether such calculations should be done at constant pressure or at constant volume, and present the displacement fields caused by interstitials and vacancies in various configurations. The elasticity theory formalism we use to analyze the displacement patterns of point defects is developed in Sec. 5.3. In this section, we also discuss the analogy between elasticity theory and electrostatics that enables us to use the method of Ewald summation to obtain displacement fields from elasticity theory. These displacement fields are compared to those obtained numerically in Sec. 5.4. A summary and

conclusions are provided in Sec. 5.5.

5.2 Displacement fields

Throughout this paper, we use the Gaussian core model as a generic model for a system of soft spheres [13, 14, 15]. In this purely repulsive system, pairs of particles interact via

$$v(r) = \varepsilon \exp(-r^2/\sigma^2) \tag{5.1}$$

where r is the inter-particle distance and ε and σ set the energy and length scales, respectively. In the following, energies are measured in units of ε and distances in units of σ. The Gaussian core model, often studied in soft condensed matter science, accurately describes the short-ranged effective interactions between polymer coils in solution [32]. Depending on temperature and density, the three-dimensional Gaussian core model can exist as a fluid, a bcc- or an fcc-solid [14]. In two dimensions, the perfect triangular lattice is the lowest energy structure at all densities [48]. Since Gaussian core particles are purely repulsive, they can form stable crystals only at pressures larger than zero. The two-dimensional Gaussian core model, which approaches the hard disk system in the limit of low temperature and low density [48], has been used previously to study the melting transition in two dimensions [48, 66].

To make contact between numerical calculations in the particle system and continuum elasticity theory, we determine, at $T = 0$, the displacement field [50]

$$\mathbf{u}(\mathbf{r}_i) \equiv \mathbf{r}_i' - \mathbf{r}_i \tag{5.2}$$

caused by the introduction of the defect into the system. Here, $\mathbf{r}_i'$ and $\mathbf{r}_i$ denote the position of particle i with and without the defect, respectively. The displacemet field completely describes the response of the system's structure to the perturbation introduced by the defect. Numerically, we determine

displacement fields by inserting a particle into or removing it from a perfect crystal on a triangular lattice. The system is then relaxed to a new minimum energy configuration by steepest descent minimization at constant volume of the simulation box. Periodic boundary conditions apply. Typically, about tens of thousands of steepest descent steps are required to determine minimum energy structures accurately. In each minimization step, each particle is moved in the direction of the force acting on the particle where the absolute value of the displacement in chosen to be small enough to ensure that the energy of the system is reduced in each step. The displacement $\mathbf{u}(\mathbf{r}_i)$ of particle i is then simply the vector which connects the position of particle i before the minimization, $\mathbf{r}_i$, with its position after the minimization, $\mathbf{r}'_i$.

The largest system we study here consists of $N = 199,680$ Gaussian core particles (without the extra particle) at a number density of $\rho = 0.6\sigma^{-2}$ corresponding to a lattice constant of $a = 1.3872\sigma$. The almost square simulation box has length $L_x = 416a$ and height $L_y = (\sqrt{3}/2)480a = 415.692a$ with aspect ratio $L_y/L_x = 0.99926$.

5.2.1 Constant V or constant p?

In calculating the displacement fields caused by point defects the question naturally arise whether one should do that at constant volume V or at constant pressure p. Naturally, the choice should depend on the particular experimental situation one is interested in. As we will show here, however, the displacement fields caused by a point defect at constant pressure and at constant volume are simply related. To determine how they are related, consider a perfect triangular crystal at $T = 0$ enclosed in a rectangular cell of volume V_0 with appropriate aspect ratio. For this particular volume, the crystal is under the hydrostatic pressure p_0. Insertion of a point defect into the crystal at a fixed total volume distorts the crystal and atom i is displaced by

$$\mathbf{u}_{V_0}(\mathbf{r}_i) = \mathbf{r}'_i(V_0) - \mathbf{r}_i(V_0), \tag{5.3}$$

where the subscript V_0 indicates that the displacement field $\mathbf{u}_{V_0}(\mathbf{r}_i)$ is obtained at constant volume V_0. In the above equation, $\mathbf{r}'_i(V_0)$ and $\mathbf{r}_i(V_0)$ are the positions of atom i in the system of volume V_0 with and without the defect, respectively. If one requires, however, that the defects is created at constant pressure p_0, the volume of the simulation cell changes from V_0 to V_1 (typically, it will increase for an interstitial and decrease for a vacancy) and the atoms are displaced by a different amount,

$$\mathbf{u}_{p_0}(\mathbf{r}_i) = \mathbf{r}'_i(V_1) - \mathbf{r}_i(V_0), \tag{5.4}$$

where the subscript p_0 implies that the displacement field is considered at constant pressure. Note that here we assume that during the generation of the defect the simulations cell only expands or contracts, but does not change its shape. This assumption can be lifted as discussed below. We now imagine that the defect generation at constant pressure is carried out in two steps: first the system is homogeneously dilated without defect from volume V_0 to volume V_1; in the second step, the defect is inserted at constant volume V_1. This two step operation corresponds to adding and subtracting $\mathbf{r}_i(V_1)$, i.e., the position of atom i at volume V_1 in the absence of the defect, to the right hand side of the above equation,

$$\mathbf{u}_{p_0}(\mathbf{r}_i) = \mathbf{r}_i(V_1) - \mathbf{r}_i(V_1) + \mathbf{r}'_i(V_1) - \mathbf{r}_i(V_0). \tag{5.5}$$

What one obtains in this way is

$$\mathbf{u}_{p_0}(\mathbf{r}_i) = \mathbf{u}_{V_1}(\mathbf{r}_i) + \mathbf{u}_h(\mathbf{r}_i, V_0, V_1), \tag{5.6}$$

where $\mathbf{u}_{V_1}(\mathbf{r}_i) = \mathbf{r}'_i(V_1) - \mathbf{r}_i(V_1)$ is the displacement field obtained by inserting the defects at volume V_1 for fixed simulation cell and $\mathbf{u}_h(\mathbf{r}_i, V_0, V_1) = \mathbf{r}_i(V_1) - \mathbf{r}_i(V_0)$ is the displacement field corresponding to a homogeneous dilatation (or contraction) of the perfect crystal without defect from volume V_0 to volume V_1. This simple deformation corresponds to a displacement

$\mathbf{u}_h(\mathbf{r}_i, V_0, V_1) = (V_1/V_0)^{1/2}\mathbf{r}_i$ (in three dimensions the exponent is 1/3). Hence the displacement fields for constant pressure and constant volume are related by:

$$\mathbf{u}_{p_0}(\mathbf{r}_i) = \mathbf{u}_{V_1}(\mathbf{r}_i) + \sqrt{\frac{V_1}{V_0}}\mathbf{r}_i. \tag{5.7}$$

Thus, one can determine the constant-pressure displacement at pressure p_0 by calculating the constant-volume displacement at volume V_1, the volume at pressure p_0 in the presence of the defect.

Similar considerations can be used to relate the constant-pressure and constant-volume displacement fields if the simulation cell is permitted to change shape as well as volume during the constant-pressure defect insertion. In this case, the simulation cell is characterized by the vectors **a** and **b** along its edges [67]. It then turns out that the displacement field of a defect inserted into an initially rectangular simulation cell with edge vectors **a** and **b** at constant hydrostatic pressure is simply related to the displacement field for fixed cell vectors $\mathbf{a}'$ and $\mathbf{b}'$ which, in general, differ from **a** and **b**. For sufficiently large systems, however, a fixed shape of the simulation cell is only a very weak constraint. In particular, a displacement field which tends to be isotropic at large distances may lead to a change in aspect ratio of the simulation cell at constant pressure, but not to a change in the relative orientation of the edge vectors. All calculations of this paper are carried out for fixed and nearly square simulation cells.

5.2.2 Interstitials

We first determine the displacement field of a single interstitial particle. This type of point defect can exist in different configurations [42] with displacement fields of different symmetries [68]. The three lowest energy structures are shown in Fig. 5.1. In one minimum-energy configuration, termed I_2 interstitial and shown in Fig. 5.1a, the extra particle and one of the original particles arrange themselves at equal distance around the lattice position of the original particle leading to a two-fold symmetry. This is the two dimen-

sional analogue of the crowdion in an fcc crystal [69]. The displacements are largest on the main defect axis, which can be aligned in any of the three low-index directions of the lattice. Since the defect symmetry differs from that of the underlying triangular lattice, one may wonder whether the rectangular periodic boundary conditions used in the calculation favor the two-fold defect symmetry. Calculations carried out with hexagonal boundary conditions, however, yield identical results demonstrating that the defect symmetry is not imposed by the symmetry of the boundary conditions.

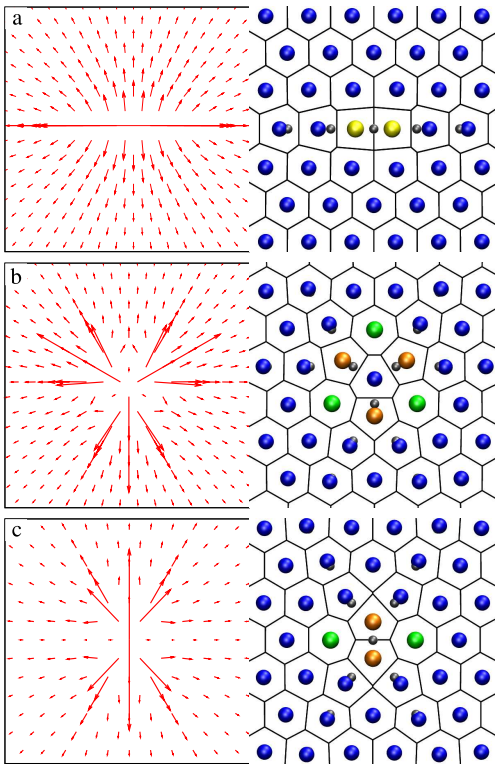

Figure 5.1: Displacement fields (left hand side) and particle configurations (right hand side) of the I_2 interstitial (a), the I_3 interstitial (b) and the I_d interstitial (c). The arrows representing the particle displacements are exaggerated in length by a factor of 20 for better visibility. On the right hand side, the small grey spheres indicate the sites of the perfect triangular lattice. The blue spheres represent particles with 6 neighbors according to the Voronoi construction (black lines). Yellow spheres are particles with 4 neighbors, orange and green spheres represent particles with 5 and 7 neighbors, respectively.

Other low-energy defect configurations include the I_3 interstitial with three-fold symmetry shown in Fig. 5.1b and the I_d interstitial or dumbbell interstitial shown in Fig. 5.1c. In the I_3 configuration, the extra particle is located at the center of a triangle spanned by three nearest neighbor lattice points and the surrounding particles are displaced outward with respect to their original positions. In the dumbbell configuration, the interstitial particle and one of the original particles compete for one lattice position as in the I_2 interstitial, but the line connecting them is orthogonal to one of the low-index lattice directions. In contrast to the I_2 interstitial, the I_d is not concentrated on one single axis.

The interstitial configurations observed in the Gaussian core model have energies that differ by less than 0.1% of the total defect energy. These energy difference correspond to roughly 20% of the thermal energy $k_{\mathrm{B}}T$ at melting. At finite temperatures that are not too low, interconversion between the various defect configurations is facile and all three of them play an important role during defect diffusion [55].

5.2.3 Vacancies

Also vacancies can occur in various configurations with displacement fields displaying quite complex patterns and symmetries lower than that of the underlying lattice. Three minimum energy configurations are shown in Fig. 5.2. In the the vacancy configuration V_2 (see Fig. 5.2a), particles move mainly on the x-axis to partially fill the void left by a removed particle. As a result, particles above and below the void site move outward generating a vortex-like displacement field. This two-fold vacancy V_2 has the same symmetry as the I_2 interstitial, but their displacement patterns are not simply related by inversion. In particular, the vortex structure observed for the vacancy is absent in the interstitial case. In the configuration V_3 with threefold symmetry, particles partially fill the vacancy void by moving in along three axes rather than two. On the other three low-index axes, particles are moved outward in response to the removed particle. A vacancy configuration analogous to the

I_d interstitial seems not to be stable even at $T = 0$. A configuration prepared in this symmetry ends in an antisymmetric configuration V_a (see Fig.5.2c). Energetically, configurations V_2 and V_a are equal and lower than configuration V_3 by more than twice the thermal energy $k_\mathrm{B}T$ at melting thus exceeding the energy difference of the corresponding interstitial configurations by more than an order of magnitude. This energy difference is less than 10% of the total defect energy.

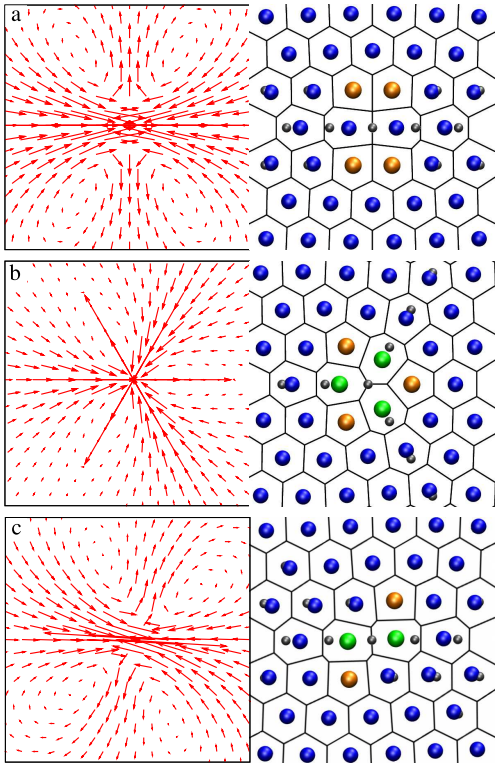

Figure 5.2: Displacement fields (left hand side) and particle configurations (right hand side) of the V_2 vacancy (a), and the V_3 vacancy (b) and the V_a vacancy (c). The arrows representing the particle displacements are exaggerated in length by a factor of 20 for better visibility. The color code is the same as in Fig.5.1.

5.3 Elasticity Theory

Near the defect site non-linearities and discrete lattice effects dominate the displacement pattern as evidenced by the highly anisotropic local structure of vacancies and interstitials. Far away from the defect, however, the perturbation of the 2d-crystal should be described accurately by continuum elasticity theory. In this regime, the response of the system to a point defect should depend on the specific form of the interaction potential only through the particular values of the elastic constants. To verify to which extent elasticity theory is valid for two-dimensional colloidal crystals of soft particles, we first review the basic equations of elasticity theory and then solve them for an idealized singular defect model consisting of a pair of singular forces of equal magnitude and opposite direction [51, 52, 53].

Linear elasticity theory is usually formulated in terms of the symmetric strain tensor [50]

$$\epsilon_{ij} = \frac{1}{2}\left(\frac{\partial u_i}{\partial r_j} + \frac{\partial u_j}{\partial r_i}\right), \tag{5.8}$$

where u_i and r_i are the i-th component of the displacement and the position, respectively. For small strains, Hook's law applies and the stress σ_{ij} is linearly related to the strain ϵ_{ij},

$$\sigma_{ij} = C_{ijkl}\epsilon_{kl}, \tag{5.9}$$

where C_{ijkl} is the stiffness tensor. Here and in the following, summation over repeated indices is implied. For isotropic materials, such as two-dimensional crystals with triangular lattice, this relation reduces to

$$\sigma_{ij} = \lambda\delta_{ij}\epsilon_{kk} + 2\mu\epsilon_{ij}, \tag{5.10}$$

where λ and μ are the so-called Lamé coefficients. The Lamé coefficient μ is also called the shear modulus.

In order to calculate the displacement field generated by a point defect one must be able to determine how the elastic continuum reacts to external forces. The condition that the forces on each infinitesimal volume element

balance leads to

$$\frac{\partial \sigma_{ij}}{\partial r_j} + f_i = 0, \tag{5.11}$$

where f_i is component i of a given volume force $f(\mathbf{r})$ acting at $\mathbf{r}$. Using the stress-strain relation from Equ. (5.10), these equilibrium conditions can be formulated in terms of the strains rather than the stresses,

$$\lambda \frac{\partial}{\partial r_i} \epsilon_{kk} + 2\mu \frac{\partial \epsilon_{ij}}{\partial r_j} + f_i = 0, \tag{5.12}$$

Inserting the definition of the strain into this equation one obtains the equilibrium conditions for the displacement field $\mathbf{u}(\mathbf{r})$,

$$(\lambda + \mu) \frac{\partial}{\partial r_i} \frac{\partial u_j}{\partial r_j} + \mu \Delta u_i + f_i = 0, \tag{5.13}$$

where $\Delta = \partial^2/\partial x^2 + \partial^2/\partial y^2$ is the Laplace operator. Solving this equation for a particular arrangement of forces used to model the point defect then yields the displacement field caused by the forces.

From the displacement field one can then determine the energetics of the point defect. In terms of the strain tensor and the Lamé coefficients the elastic free energy density of the system is given by

$$g = \frac{\lambda}{2} \epsilon_{kk}^2 + \mu \epsilon_{ij}^2. \tag{5.14}$$

Accordingly, the energy density at $T = 0$ is given by

$$e = \frac{\lambda}{2} \epsilon_{kk}^2 + \mu \epsilon_{ij}^2 - p \epsilon_{kk}. \tag{5.15}$$

The last term of this equation stems from the work done against the pressure p by the dilatation ϵ_{kk}. The strain tensor can also be written as the sum of a trace-free shear and a homogeneous dilation leading to the expression

$$g = \mu \left(\epsilon_{ij} - \frac{1}{2} \delta_{ij} \epsilon_{kk} \right)^2 + \frac{K}{2} \epsilon_{kk}^2, \tag{5.16}$$

where K is the so-called bulk modulus related to λ and μ by

$$K = \lambda + \mu. \tag{5.17}$$

The Poisson ratio ν, i.e., the negative ratio of transverse strain to axial strain upon uniaxial loading, is given by

$$\nu = \frac{\lambda}{\lambda + 2\mu} = \frac{K - \mu}{K + \mu} \tag{5.18}$$

and describes how a material reacts when stretched. In the next subsection we will calculate the elastic constants for our system at $T = 0$.

5.3.1 Elastic moduli

For a crystal in which particles interact with a pair potential $v(r)$ depending only on the interparticle distance r the total energy E of N particles is given by

$$E = \frac{1}{2} \sum_{i \neq j} v(|\mathbf{r}_i - \mathbf{r}_j|), \tag{5.19}$$

where $\mathbf{r}_i$ and $\mathbf{r}_j$ are the positions of particles i and j respectively. In this case and for $T = 0$, the energy density e_0 of the undistorted lattice, the pressure p, as well as the elastic constants K and μ can be calculated from simple lattice sums:

$$e_0 = \frac{\rho}{2} \sum_i{}' v(r_i), \tag{5.20}$$

$$p = -\frac{\rho}{4} \sum_i{}' v'(r_i) r_i, \tag{5.21}$$

$$K = \frac{\rho}{8} \sum_i{}' \left[v''(r_i) r_i^2 - v'(r_i) r_i \right], \tag{5.22}$$

and

$$\mu = \frac{\rho}{2} \sum_i{}' \left[v''(r_i) \left(\frac{x_i y_i}{r_i} \right)^2 + v'(r_i) \frac{y_i^4}{r_i^3} \right]. \tag{5.23}$$

Here, $v'(r)$ and $v''(r)$ are the first and second derivative of the pair po-

tential, respectively, ρ is the number density, r_i is the distance of particle i from the origin, and x_i and y_i are its Cartesian coordinates. The lattice position is chosen such that there is one particle at the origin. The sums in the above equations must include a sufficient number of particles to ensure convergence of the sums. (The prime on the sum symbol indicates that the particle at the origin is not included in the sum).

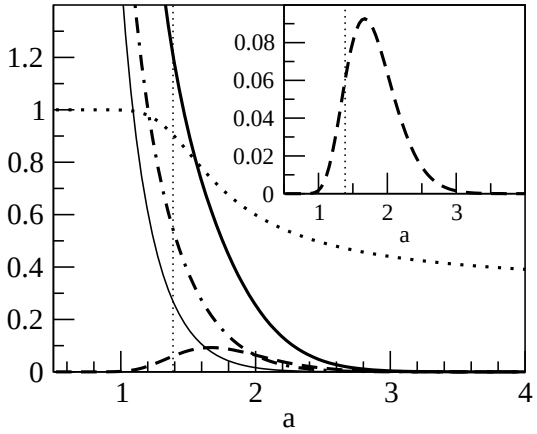

Figure 5.3: Bulk modulus K (solid line), shear modulus μ (dashed line), pressure p (dash-dotted line), energy density e (thin solid line), and Poisson ratio ν (dotted line) as a function of the lattice constant a. The moduli are given in units of ε/σ^2 and the lattice constant in units of σ. In the inset, the shear modulus μ is displayed on a larger scale. The vertical thin dotted line indicates the lattice constant $a = 1.3872\sigma$ corresponding to the density $\rho = 0.6\sigma^{-2}$, at which all calculations discussed in this article are carried out.

The elastic constants μ, and K as well as the Poisson ratio ν, the pressure p and the energy density e, calculated using such sums, are shown in Fig. 5.3 as a function of the lattice constant a, which, in a triangular lattice, is related to the density by $\rho = 2/\sqrt{3}a^2$. At a density of $\rho = 0.6\sigma^2$, the density at which all calculations presented in this article are carried out, the elastic constants have the values $K = 1.2089\,\varepsilon\sigma^{-2}$ and $\mu = 0.060183\,\varepsilon\sigma^{-2}$, the pressure is $p = 0.544245\,\varepsilon\sigma^{-2}$, and the Poisson ratio is $\nu = 0.905151$. The energy density is $e_0 = 0.269125\,\varepsilon\sigma^{-2}$ corresponding to an energy per particle of $E/N = 0.448542\varepsilon$. Note that at this density, the system is stabilized against shear only by interactions beyond nearest-neighbor contributions; estimation

of μ from nearest neighbor interactions only yields a negative shear rate at this density. While the bulk modulus K increases monotonically with the density (and, as the pressure p, is proportional to ρ^2 for small densities), the shear modulus reaches a maximum at $a \approx 1.67$ and then rapidly decays to zero for lattice constants larger and smaller than that. This behavior of the shear modulus is a reflection of the phenomenon of reentrant melting observed in the three-dimensional Gaussian core model [13, 14] and indicates that also in two dimensions a Gaussian core crystal melts if sufficiently compressed.

5.3.2 Point defect model

We next use elasticity theory to determine the displacement field created by introducing an idealized point defect into a perfect isotropic crystal. The dilatation (or contraction) caused by the defect is modeled by two orthogonal pairs of forces. Each pair consists of two forces of equal magnitude F but opposite directions acting at two points separated by the distance h. If one assumes that one force pair acts in x-direction and the other one in y-direction and that the defect is centered a the origin, the total force density is given by

$$\begin{aligned} \mathbf{f}(\mathbf{r}) &= -F\delta(\mathbf{r})\mathbf{e}_x + F\delta(\mathbf{r} - h\mathbf{e}_x)\mathbf{e}_x \\ &\quad -F\delta(\mathbf{r})\mathbf{e}_y + F\delta(\mathbf{r} - h\mathbf{e}_y)\mathbf{e}_y. \end{aligned} \tag{5.24}$$

Here, $\mathbf{e}_x$ and $\mathbf{e}_y$ are the unit vectors in x- and y-direction, respectively, and $\delta(\mathbf{r})$ is the Dirac delta-function in two dimensions. One then lets the separation h go to zero and the force F go to infinity in a way such that Fh remains constant. This defect model, in which the net force acting on the material vanishes, is equivalent to inserting a small circular inclusion into a hole of different size [52].

The displacement field caused by this type of point defect can be determined by first calculating the Green's function for a singular force and than carrying out the limit $h \to 0$. Alternatively, one can carry out the limit

$h \to 0$ first and then solve the equilibrium condition for the force density obtained in that way. In the following we will calculate the displacement field of the point defect model using this second approach, in which periodic boundary conditions can be taken into account particularly easily.

Carrying out the limit $h \to 0$ as described above the total force density of Equ. (5.24) reduces to

$$\mathbf{f}(\mathbf{r}) = -Fh\nabla\delta(\mathbf{r}). \tag{5.25}$$

Inserting this expression into Equ. (5.13) one obtains the equilibrium condition for this simple point defect model,

$$(\lambda+\mu)\frac{\partial}{\partial r_i}\frac{\partial u_j}{\partial r_j} + \mu\Delta u_i = Fh\frac{\partial}{\partial r_i}\delta(\mathbf{r}). \tag{5.26}$$

Taking the divergence on both sides yields

$$\Delta(\lambda+2\mu)\frac{\partial u_j}{\partial r_j} = Fh\Delta\delta(\mathbf{r}). \tag{5.27}$$

To solve this equation it suffices to find a displacement field that obeys

$$(\lambda+2\mu)\frac{\partial u_j}{\partial r_j} = Fh\delta(\mathbf{r}). \tag{5.28}$$

Using the Helmholtz-decomposition in two dimensions, we now write the displacement in terms of the gradients of two scalar functions $\phi(\mathbf{r})$ and $A(\mathbf{r})$ as a sum of an irrotational and a divergence-free part,

$$u_i = \frac{\partial\phi}{\partial r_i} + \omega_{ij}\frac{\partial A}{\partial r_j}, \tag{5.29}$$

where the matrix ω_{ij} exchanges the components of the gradient and changes the sign of one of them: $\omega_{11} = \omega_{22} = 0$ and $-\omega_{21} = \omega_{12} = 1$. Then, Equ. (5.28) becomes

$$\Delta\phi(\mathbf{r}) = 2\pi\gamma\delta(\mathbf{r}), \tag{5.30}$$

where we have used the fact that $\omega_{ij}\partial A/\partial r_j$ is divergence-free and the parameter γ, which has the dimension of an area, is given by

$$\gamma = \frac{Fh}{2\pi(\lambda + 2\mu)}. \tag{5.31}$$

Equation (5.30) is the Poisson equation of electrostatics for a point charge of strength $-\gamma$ in two dimensions.

A similar equation can be derived for the the scalar function $A(\mathbf{r})$ by taking the 2d-vorticity, defined as $\omega_{ij}\partial v_j/\partial r_i$ for an arbitrary vector field $\mathbf{v} = (v_1, v_2)$, of both sides of Equ. (5.26). Since the vorticity of a gradient field vanishes, one obtains the biharmonic equation

$$\mu\Delta(\Delta A(\mathbf{r})) = 0. \tag{5.32}$$

This equation is obeyed if the scalar field $A(\mathbf{r})$ is a solution of the Laplace equation

$$\Delta A(\mathbf{r}) = 0. \tag{5.33}$$

In the following, we will use the trivial solution $A(\mathbf{r}) = \text{const}$ and satisfy the boundary conditions through proper solution of the Poisson equation (5.30) for the scalar field ϕ.

To do that, we note that $K(\mathrm{r}) = \ln(r)/2\pi$ is a solution of $\Delta K = \delta(\mathbf{r})$ (see, for instance, Ref. [54]), and hence we obtain the Green's function

$$\phi(r) = \gamma \ln(r). \tag{5.34}$$

The corresponding displacement field $\mathbf{u}(\mathbf{r})$ follows by differentiation according to Equ. (5.34),

$$\mathbf{u}(\mathbf{r}) = \gamma\frac{\mathbf{r}}{r^2}. \tag{5.35}$$

Thus, the displacement field caused by the point defect is isotropic and long-range with a magnitude that is proportional to $1/r$. This result is valid for an infinitely extended elastic medium where the boundary conditions $\mathbf{u} = 0$ ap-

ply at infinity. This situation, however, does not correspond to the boundary conditions applied in computer simulations. In the following section we will discuss how to solve Equ. (5.30) with the appropriate boundary conditions.

5.3.3 Boundary conditions

In comparing the results of particle simulations with those of elasticity theory it is important to realize that the displacement fields predicted by continuum theory are of long-range nature. Therefore, it is crucial that corresponding boundary conditions are used in both cases. All simulations discussed in this paper are done with periodic boundary conditions in order to minimize finite size effects and preserve the translational invariance of the perfect lattice. Hence, also the continuum calculations need to be carried out with periodic boundary conditions. For a rectangular system with side lengths L_x and L_y, periodic boundary conditions require that $\mathbf{u}(\mathbf{r}) = \mathbf{u}(\mathbf{r} + \mathbf{l})$, where $\mathbf{l} = (iL_x, jL_y)$ is an arbitrary lattice vector with integer i and j. In the following, we will solve the Poisson equation (5.30) for this type of boundary conditions.

We start by noting that the homogenous part of the Poisson equation (5.30) admits the non-trivial solution $\phi_0(\mathbf{r}) = \text{const}$ that satisfies the boundary conditions. Therefore, one needs to consider the *extended* Green's function for the solution of the general Poisson equation $\Delta\phi(\mathbf{r}) = 2\pi\rho(\mathbf{r})$ [54, 70]. In this case, the right hand side of the Poisson equation must be orthogonal to the solution $\phi_0(\mathbf{r})$,

$$\int \mathrm{d}\mathbf{r}\, \phi_0(\mathbf{r})\rho(\mathbf{r}) = \text{const} \int \mathrm{d}\mathbf{r}\, \rho(\mathbf{r}) = 0. \tag{5.36}$$

In electrostatics, this condition corresponds to charge neutrality (the physical meaning of this condition in our case will be discussed below). To satisfy this orthogonality condition we must modify the Poisson equation (5.30) by subtracting $1/A$ from the delta function,

$$\Delta\phi(\mathbf{r}) = 2\pi\gamma \left[\delta(\mathbf{r}) - \frac{1}{A}\right], \tag{5.37}$$

where A is the area of the rectangular basic cell. In this modified equation, the right hand side contains a homogeneous "neutralizing background" that exactly compensates for the "charge" of the delta function. Solution of this equation yields the extended Green's function of the problem. To obtain a unique solution $\phi(\mathrm{r})$ of this equation one must furthermore require that this solution be orthogonal to $\phi_0(\mathrm{r})$,

$$\int \mathrm{d}\mathbf{r}\, \phi_0(\mathbf{r})\phi(\mathbf{r}) = \mathrm{const} \int \mathrm{d}\mathbf{r}\, \phi(\mathbf{r}) = 0. \tag{5.38}$$

For our case this condition is irrelevant, as only derivatives of $\phi(\mathbf{r})$ carry physical significance. Once the function $\phi(\mathrm{r})$ has been determined by solving Equ. (5.37), the displacement field follows by differentiation.

Rigid circular container

Before we embark on the solution of the extended Poisson equation (5.37) for periodic boundary conditions, we illustrate the concepts introduced above by determining the displacement field of a point defect in an elastic material enclosed in a container with rigid walls. Due to these walls, the component of the displacement field normal to walls must vanish at the wall, $u_\perp = 0$. No condition applies for the parallel component $u_{||}$. For a rectangular container such rigid wall boundary conditions are equivalent to periodic boundary conditions. If we assume, without loss of generality, that the point defect is located at the center of the rectangular periodic cell, the component of the displacement field normal to the boundary of the periodic cell vanishes also in this case. In the following, we will determine the effect of such rigid boundary conditions on the displacement field of a point defect located at the center of a circular cavity enclosed by hard walls. For this case, which exhibits all complications mentioned above, a simple analytical solution can be easily obtained.

Consider a two-dimensional elastic isotropic material enclosed in a circular container of radius R. We choose the coordinate system such that the

origin is at the center of the container. To determine the displacement field caused by a point defect of strength γ placed at the origin we need to solve Equ. (5.37) under the condition that the at distance R from the origin the displacement $u_\perp$ normal to the wall vanishes. We construct a solution by superposing the solution for the extended material, $\mathbf{u}_\infty(\mathbf{r}) = \gamma\mathbf{r}/r^2$, and a homogeneous contraction, $\mathbf{u}_\mathrm{c}(\mathbf{r}) = -\alpha\mathbf{r}$,

$$\mathbf{u}(\mathbf{r}) = \mathbf{u}_\infty(\mathbf{r}) + \mathbf{u}_\mathrm{c}(\mathbf{r}) = \gamma\frac{\mathbf{r}}{r^2} - \alpha\mathbf{r}. \tag{5.39}$$

While $\mathbf{u}_\mathrm{c}(\mathbf{r})$ corresponds to a homogeneous contraction without shear, $\mathbf{u}_\infty(\mathbf{r})$ corresponds to a pure shear without dilatation (except for $r = 0$). To satisfy the boundary conditions at $r = R$, we set $\alpha = \gamma/R^2$ obtaining

$$\mathbf{u}(\mathbf{r}) = \gamma\mathbf{r}\left(\frac{1}{r^2} - \frac{1}{R^2}\right). \tag{5.40}$$

This displacement field corresponds to the "potential"

$$\phi(\mathbf{r}) = \phi_\infty(\mathbf{r}) + \phi_\mathrm{c}(\mathbf{r}) = \gamma\left(\ln\frac{r}{R} - \frac{1}{2}\frac{r^2}{R^2} + \frac{3}{4}\right), \tag{5.41}$$

where the last constant on the right hand side takes care of the condition expressed in Equ. (5.38). It is straightforward to verify that

$$\Delta\phi(\mathbf{r}) = \Delta\phi_\infty(\mathbf{r}) + \Delta\phi_c(\mathbf{r}) = 2\pi\gamma\delta(\mathbf{r}) - \frac{2\pi\gamma}{A}, \tag{5.42}$$

such that the potential from Equ. (5.41) satisfies the extended Poisson equation (5.37).

A comparison of results obtained numerically for an I_2 interstitial and the prediction of elasticity theory (Equ. (5.40)) is shown in Fig. 5.4. For the particle system the rigid container was realized by carrying out the calculation in a larger system in which all particles beyond a distance of R from the origin where kept at fixed positions. The displacements obtained from particle and continuum calculations agree very well for all defect distances

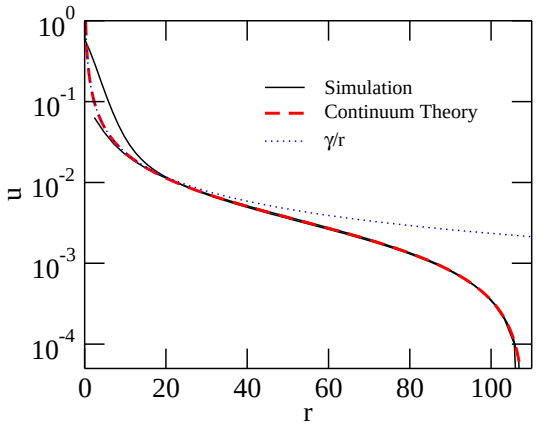

Figure 5.4: Displacement components u_x and u_y as a function of the distance r (thin solid lines) for an I_2 interstitial with its main axis oriented in x-direction. The circular hard wall container has a radius of $R = 106.8\sigma$. Also plotted is the displacement computed from continuum theory according to Equ. (5.40) (dashed line) for a defect strength of $\gamma = 0.234495\sigma^2$ which best fits the numerical results in the far field and the simple $1/r$-behavior (dotted line).

larger than about 15 lattice constants. In Fig. 5.5 we depict the relative error which we define in the following way:

$$\xi \equiv \frac{|\mathbf{u}_p(\mathbf{r}) - \mathbf{u}_c(\mathbf{r})|}{|\mathbf{u}_c(\mathbf{r})|}. \tag{5.43}$$

Here, $\mathbf{u}_p(\mathbf{r})$ and $\mathbf{u}_c(\mathbf{r})$ are the displacement fields obtained from the particle system and from the predictions of continuum theory, respectively. The relative error close to the defect can be larger than 100% (red). For distances of $r > 20\sigma$ with find an error of approximately $1 - 5\%$ (green). Close to the rigid container the relative error increases again due to discrete lattice effects.

Similar agreement is found also for the energy density as shown in Fig. 5.6. For the displacement field of Equ. (5.40) one finds, using Equ. (5.15) the energy density

$$e(r) = 2\mu\frac{\gamma^2}{r^4} + 2K\frac{\gamma^2}{R^4} + 2p\frac{\gamma}{R^2}. \tag{5.44}$$

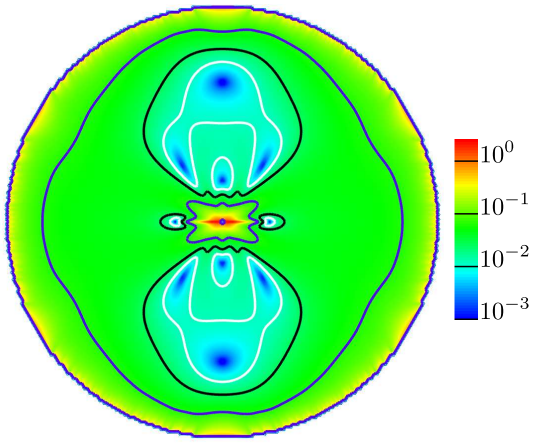

Figure 5.5: Color coded relative deviation ξ calculated according to Equ. (5.43) of an I_2 interstitial at the origin of a rigid circular box with radius $R = 108.19\sigma$. The fit parameter $\gamma = 0.234495\sigma^2$ was found by minimizing the sum of the relative error of particles at distances larger than 30σ. The contour lines in white, black, and blue represent an error of 1%, 2%, and 5%, respectively.

This prediction of elasticity theory matches the energy density determined numerically in y-direction (see Fig. 5.6). Due to the strong anisotropy of the I_2 defect, larger deviations are observed in x-direction. For distances of more than about 15 lattice spacings the energy density plateaus at a constant value. In this regime, the energy density is essentially constant, $e = 2p\gamma/R^2$, and corresponds to the work done by the defect against the pressure p. As discussed below, the plateau value of the density is related to the neutralizing background on the right hand side of Equ. (5.37).

Ewald summation

For an isolated defect at the center of a rectangular cell, the symmetry imposed by periodic boundary conditions requires that the components of the displacement field orthogonal to the surface of the cell vanish. In a first attempt to obtain the displacement field for such boundary conditions one may start from the solution for the extended material and satisfy the boundary conditions by placing "image defects", each of which carries the displace-

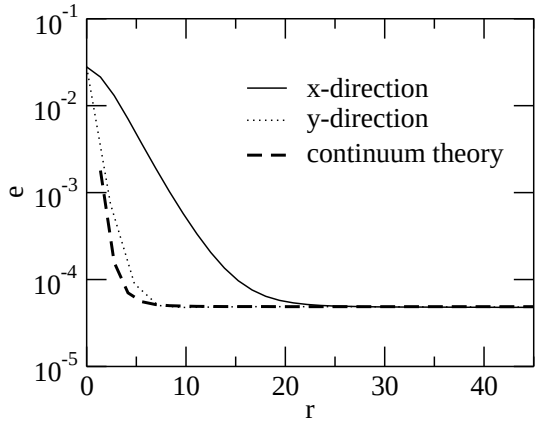

Figure 5.6: Energy density e as a function of distance r measured along the x-axis (solid line) and the y-axis (dotted line) for the particle system in a circular container with hard walls and radius $R = 71.91\sigma$. Also shown is the energy density calculated from continuum theory according to Equ. (5.44) (dashed line).

ment field for the infinitely extended material, at appropriate positions. For a rectangular cell, an infinite number of image defects arranged on a regular lattice with lattice constants L_x and L_y in x- and y-direction, respectively, are required. These image defects, which are analogous to the image charges of electrostatics, correspond to the defects in the periodic images of the basic simulation cell. Superposition of the displacement fields of all image defects then yields the displacement field for periodic boundary conditions.

Due to the long-range nature of the defect field for the infinite material, however, such a summation of the contribution of all image defects leads to displacement fields that are only conditionally convergent. A more appropriate treatment that avoids this problem consists in determining the Green's function of the Poisson equation (5.37) for periodic boundary conditions. The requirement imposed by the periodic boundary conditions can be easily satisfied by expressing the solution as a Fourier series and solving the Poisson equation in Fourier space. This treatment, however, leads to series that are only conditionally convergent with values that depend on the summation order. The solution of this problem using so called Ewald sums is known

from electrostatics [46, 47, 70] and consists in separating the conditionally convergent series into a real space and and a Fourier space part,

$$\phi(\mathbf{r}) = \gamma \left\{ \frac{1}{2} \sum_{\mathbf{l}} E_i[-\eta^2 |\mathbf{r}+\mathbf{l}|^2] \right. \\ \left. - \frac{2\pi}{A} \sum_{\mathbf{k}\neq 0} \frac{e^{-k^2/4\eta^2}}{k^2} \cos(\mathbf{k}\cdot\mathbf{r}) + \frac{\pi}{2\eta^2 A} \right\}. \tag{5.45}$$

Here, $E_i(x) = \int_{-\infty}^{x} (e^t/t)\, dt$ is the exponential integral and A is the area of the rectangular cell. The first sum is over all lattice vectors $\mathbf{l}$ and the second sum is over all reciprocal vectors $\mathbf{k}$ consistent with the periodic boundary conditions. The adjustable parameter η, set to a value of $\eta = 6/L_x$ here, determines the rate of convergence of the two sums, but the value of the sums does not depend on η. The exclusion of the $\mathbf{k} = 0$ term in the above equation stems from the requirement that both $\phi(\mathbf{r})$ and the right hand side of the Poisson equation need to be orthogonal to $\phi_0(\mathbf{r})$ as expressed in Eqs. (5.36) and (5.38). It is easy to show by direct calculation of the Laplacian $\Delta\phi$ that the above expression for $\phi(\mathbf{r})$ indeed obeys Equ. (5.37) and thus implies a neutralizing background of magnitude γ/A as in the previous example.

From Equ. (5.45) for the scalar function $\phi(\mathbf{r})$ the displacement field of a point defect in a system with periodic boundary conditions is determined by differentiation,

$$u_i(\mathbf{r}) = \gamma \left\{ \sum_{\mathbf{l}} \frac{r_i + l_i}{|\mathbf{r}+\mathbf{l}|^2} e^{-\eta^2 |\mathbf{r}+\mathbf{l}|^2} \right. \\ \left. + \frac{2\pi}{A} \sum_{\mathbf{k}\neq 0} \frac{e^{-k^2/4\eta^2}}{k^2} k_i \sin(\mathbf{k}\cdot\mathbf{r}) \right\}. \tag{5.46}$$

For the systems and parameters considered in this paper, the real space sum can be truncated after the first term and the Fourier space sum can be evaluated accurately using about 50×50 reciprocal vectors.

As mentioned above, exactly the same boundary conditions apply if the

system is constrained by hard walls to reside in an area of given size. Also in that case, the boundary conditions require that the component of the displacement field orthogonal to the walls vanishes. Hence, in the continuum description, hard walls have the same effect as an infinite array of image "charges" (plus "neutralizing background") placed on a regular lattice with a geometry determined by the wall positions. The effect of such image charges and the neutralizing background is, therefore, not a pure artifact of the periodic boundary condition applied in the simulations, but occurs also in experimental realizations of colloidal crystals of purely repulsive particles which need to be kept together by confining walls. Accordingly, the analysis of displacement patterns (and defect interactions) observed experimentally requires a similar treatment as that used here for the interpretation of our simulation results.

5.3.4 Electrostatic analogy

In electrostatics, the technique of Ewald summation is used to determine the energetics of periodic systems containing point charges and dipoles. When one uses this technique, one implicitly stipulates that the charges are immersed in a homogeneous background that compensates for the point charges and establishes overall charge neutrality. This neutralizing background is imposed by the periodic boundary conditions; without it, no periodic solution of the Poisson equation exists. Since mathematically the situation we face when determining the displacement field of point defects is identical to that of electrostatics, one may wonder about the physical meaning of the neutralizing background in our Equ. (5.37).

To address this question, we note that the local volume change, or dilatation, due to a displacement field $\mathbf{u}(\mathbf{r})$ is given be the trace ϵ_{kk} of the corresponding strain tensor [50]. The total change in volume ΔV of a certain region G is then given as the integral over the dilatation,

$$\Delta V = \int_G \mathrm{d}\mathbf{r}\, \epsilon_{kk}(\mathbf{r}). \tag{5.47}$$

On the other hand, it follows from the definition of ϕ (see Equ. (5.29)) that the trace of the strain tensor is equal to the Laplacian of ϕ,

$$\Delta\phi(\mathbf{r}) = \epsilon_{kk}(\mathbf{r}). \tag{5.48}$$

Thus, the Poisson equation (5.37) is an equation for the local dilatation. According to this equation, at the defect site the dilatation is required to have a delta like peak of strength $2\pi\gamma$. The total volume change caused by this singular dilatation, $\Delta V = \int_A \mathrm{d}\mathbf{r}\, 2\pi\gamma\delta(\mathbf{r}) = 2\pi\gamma$, is exactly compensated by the total volume change originating from the constant neutralizing background, $\Delta V = -\int_A \mathrm{d}\mathbf{r}\, 2\pi\gamma/A = -2\pi\gamma$. (Calculating the strain tensor directly from the displacement field of Equ. (5.46) indeed yields $\epsilon_{kk} = -2\pi\gamma/A$.) Therefore, the condition of charge neutrality of electrostatics corresponds to the requirement of constant volume in our case. In this analogy, the charge density of electrostatics corresponds to the local dilatation (the charge corresponds to the volume change) and the role of the electric field is played here by the displacement field.

This interpretation of the Poisson equation (5.37) also suggests a definition of the defect volume V_d. As mentioned above, introduction of a point defect of strength γ leads to a total volume change which can be viewed as the volume of the defect,

$$V_d = 2\pi\gamma. \tag{5.49}$$

With periodic (or rigid) boundary conditions the system as a whole is prevented from changing volume and the volume change due to the defect is exactly compensated by the homogeneous neutralizing background. This defect volume is also what one gets when calculating the expansion of a circle under the $1/r$-deformation caused by the idealized defect model (see Equ. (5.35)). Measuring the parameter γ, for instance by fitting the displacement field far from the defect to the continuum theory results, thus permits to determine the defect volume. For the I_2 at a density of $\rho = 0.6\sigma^{-2}$, for example, we found a volume of $V_d = 1.44\sigma^2$, which is slightly smaller then

$V_0 = 1.66\sigma^2$, the volume per particle in the perfect lattice.

The neutralizing background appearing in the Poisson equation (5.37) also figures in the energy density and can contribute considerably to the total defect energy. According to Equ. (5.15), the energy density includes the term $e_p = -\epsilon_{kk}p$ arising from the work carried out by the defect against the pressure p. Away from the singularity at the origin, this component of the energy density is constant, $e_p = 2\pi\gamma/A$, and it dominates for large distances from the defect. Although e_p is proportional to $1/A$ and therefore small in general, integrating it over the entire area (leaving out the unphysical singularity at the origin) yields an energy contribution of $E_p = 2\pi\gamma$ which is independent of system size and can be substantial. For an I_2 interstitial in our Gaussian core system at $\rho = 0.6\sigma^{-2}$, for instance, this contribution amounts to more than 50% of the total defect energy. Interestingly, no such pressure contribution arises for the displacement field of Equ. (5.35) obtained for the infinitely extended material. Thus, the condition of fixed volume imposed by the periodic boundary conditions leads to measurable effects also in the large system limit and even boundary conditions applied at infinity matter.

5.4 Comparison of simulation and continuum theory

In this section we compare the results of the particle-based simulations with the predictions of continuum elasticity theory obtained in the previous section. In particular, we verify at which distances from the point defect elasticity theory becomes valid and which effect boundary conditions have on the displacement fields. We first consider the displacement fields of interstitials, then those of vacancies.

5.4.1 Interstitials

As discussed in Sec. 5.2, insertion of an interstitial particle into a perfect lattice can lead to different displacement patterns, all of which are highly anisotropic near the defect site. Farther away from the defect the anisotropy should subside as the isotropic behavior expected from elasticity theory sets in. This is indeed what is observed for intermediate distances from the defect as shown in Fig. 5.7 for an I_2 defect. In the bottom panel of this figure, the displacement magnitude $|\mathbf{u}(\mathbf{r})|$ is plotted as a function of the distance r from the defect. Each dot corresponds to one particular particle. While for short distances the displacement magnitude is not a unique function of r due to the anisotropy of the defect, at larger distances $|\mathbf{u}(\mathbf{r})|$ is essentially determined by r. In this intermediate regime, the displacement magnitude seems to follow the $1/r$-behavior predicted by elasticity theory for the infinitely extended material. Due to the periodic boundary conditions, however, the displacement magnitude cannot remain isotropic as the boundary is approached. In fact, the periodic boundary conditions lead to a spread of $|\mathbf{u}(\mathbf{r})|$ at larger distances. The two prongs observed in the bottom panel of Fig. 5.7 correspond to the directions along the x- and y-axes and along the diagonals.

This kind of behavior is observed even more clearly for the displacement directions. In the top panel of Fig. 5.7, the angle θ between the displacement $\mathbf{u}(\mathbf{r})$ and the position vector $\mathbf{r}$ is plotted as a function of distance r. As in the bottom panel, each dot corresponds to an individual particle. For an isotropic displacement field, the displacement and the position vector are perfectly aligned and $\theta = 0$. Thus, non-zero angles θ are an indication of anisotropy. For small distances r angles θ larger than $\pi/4$ occur. For intermediate distances, $20 < r < 150$, the angle θ is small since in this regime the displacements approximately points away from the origin. For larger distances, the periodic boundary conditions then lead to a spread in θ and deviations of up to $\theta = \pi/2$ are possible.

The long-distance behavior described above is perfectly reproduced by linear elasticity theory. As shown in Fig. 5.8 for I_2 interstitials and in

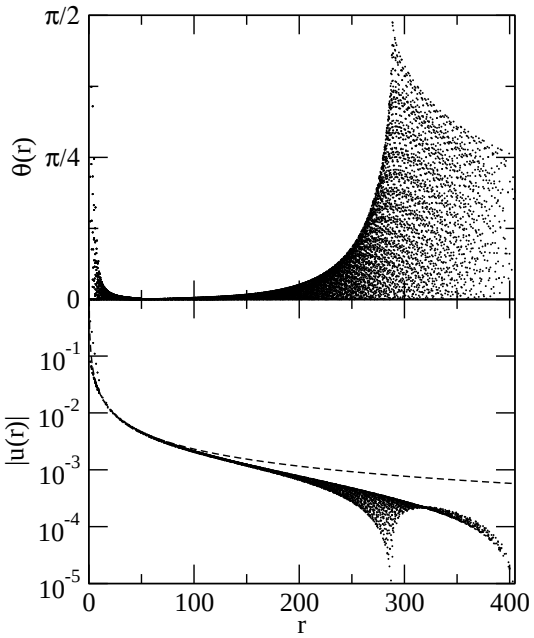

Figure 5.7: Top: Angle θ between the displacement vector $\mathbf{u}$ and the position vector $\mathbf{r}$ as a function of the distance r from the defect for an I_2 interstitial in a 208×240 particle system. Each dot corresponds to one particle. Bottom: Displacement magnitude $|\mathbf{u}(\mathbf{r})|$ as a function of r. Also shown as a dashed line is the γ/r-line for $\gamma = 0.23165\sigma^2$.

Fig. 5.9 for I_3 and I_d interstitials, respectively, the displacement calculated using Ewald summation according to Equ. (5.46) agrees very well with the numerical results for all distances larger than about $10 - 15$ lattice spacings. In particular, the deviations from the $1/r$-behavior near the cell boundary are perfectly captured by elasticity theory with periodic boundary conditions. For small distances, on the other hand, the displacement field in the particle system is highly anisotropic with strong deviations between the x- and y-direction. In this non-linear core region elasticity theory is not applicable and the displacements of the three configurations differ. The exponential short-range dependence of u_x on the distance r for I_2 interstitials is, however, captured by a simple bead-spring model discussed in Ref. [68]. In this model, the exponential decay constant can be related to the elastic constants of the material.

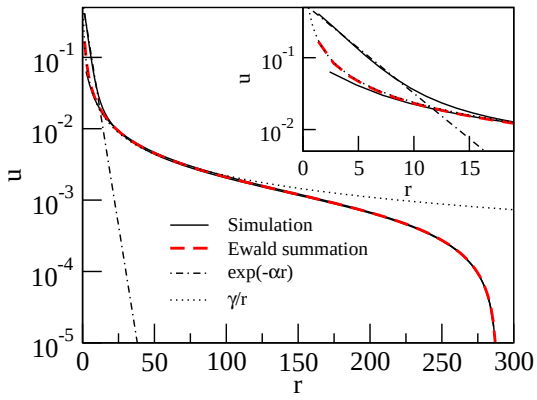

Figure 5.8: Displacement components u_x and u_y of the I_2 interstitial as a function of distance r along the x-axis and y-axis, respectively (solid lines). The main axis of the I_2 defect is oriented in x-direction. Also plotted are the displacement computed from continuum theory by Ewald summation according to Equ. (5.46) (dashed line), and simple $1/r$-behavior (dotted line). For short distances, the behavior of the displacement along the x-axis is exponential (dash-dotted line) as described by a simple bead-spring model [68]. The inset shows the region close to the defect location. A defect strength of $\gamma = 0.23165\sigma^2$ was used here since this value yields the best fit of the results obtained from elasticity theory and the numerical results at large distances from the defect.

In the comparison of the results obtained for the particle system with those of continuum theory the defect strength γ is treated as an adjustable parameter. For each configuration, I_2, I_3, and I_d, the particular displacement strength γ was found by optimizing the relative error (see Equ. (5.43)) at distances larger than 30.0σ from the origin of the defect. For the I_2 defect, a value of $\gamma = 0.23165\sigma^2$ yields the best fit. I_3 and I_d interstitials produce a slightly larger displacement with a strength of $\gamma = 0.2347\sigma^2$ and $\gamma = 0.2425\sigma^2$, respectively. The question arises if this fit is independent on the size of the box. In Fig. 5.10 we depict the displacement of an I_2 defect for different box sizes together with the results from the Ewald summation. The displacements plotted in the inset of Fig. 5.10 on a doubly-logarithmic scale clearly indicate that the algebraic $1/r$ behavior is observed, if at all, only for large system sizes and in a limited distance range.

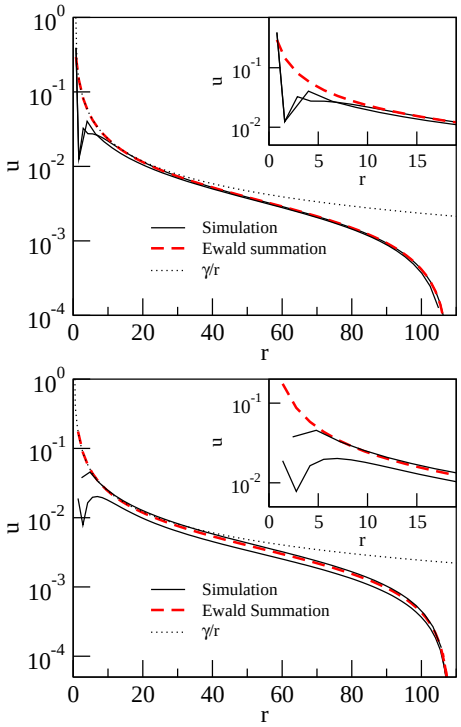

Figure 5.9: Top: Displacement components u_x and u_y of the I_3 interstitial as a function of distance r along the x-axis and y-axis, respectively (solid lines). Also plotted are the displacements computed from continuum theory by Ewald summation according to Equ. (5.46) (dashed line), and simple $1/r$-behavior (dotted line). The inset shows the region close to the defect location. A defect strength of $\gamma = 0.2347\sigma^2$ was used. Bottom: Displacement components as above for an I_d interstitial with $\gamma = 0.2425\sigma^2$.

A comparison of the Ewald summation results with the numerical calculations over the whole simulation cell is shown in Fig. 5.11. The color coded map represents the relative deviation (see Equ. (5.43)) of $\mathbf{u}_p(\mathbf{r})$ from $\mathbf{u}_c(\mathbf{r})$. In the figure, regions of large and small relative deviation are colored in red and blue, respectively. We find that the I_2 and I_3 configuration show a relative deviation between 1% to 5% over the whole range. Only in the core region of the defect the deviations are larger. For the I_d defect the deviations are larger and between 10% to 20% also far away from the defect. These deviations are due to discrepancies both in orientations as well as magnitude.

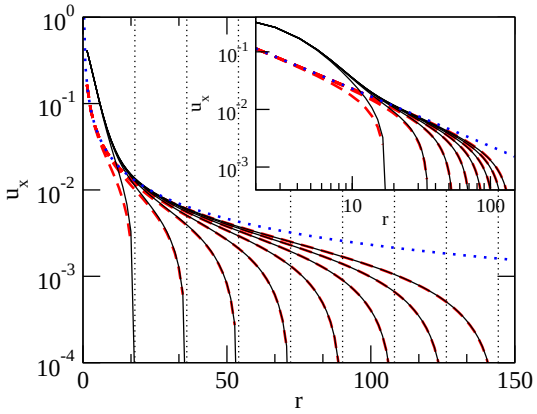

Figure 5.10: Displacement component u_x as a function of distance r from the defect along the x-axis obtained from simulations (solid lines) and according to Equ. (5.46) (dashed lines) for system sizes $N = 26 \times 30, 52 \times 60, 78 \times 90, 104 \times 120, 130 \times 150, 156 \times 180, 182 \times 210, 208 \times 240$. Also shown is the γ/r behavior expected in an infinitely extended material (dotted line). The same value of $\gamma = 0.23165\sigma^2$ was used in all cases. The vertical dotted lines indicate the distances of the cell boundaries from the origin for the various system sizes. In the inset the same curves are displayed on a logarithmic scale.

The energy density of a point defect with periodic boundaries, calculated from Equ. (5.15) for the displacement field of Equ. (5.46), is depicted in Fig. 5.12. As for the point defect in a circular rigid container discussed in Sec. 5.3.3, the energy density becomes constant for large distances. This constant term arises from the work performed by the defect against the external pressure.

5.4.2 Vacancies

In the system studied in this paper, vacancies generate displacement patterns that are considerably more intricate than those of interstitials, as can be inferred from a comparison of Figs. 5.1 and 5.2. While in the case of interstitials the displacement vectors essentially point away from the defect site, vacancies have displacement fields which point outward or inward depending on the position relative to the defect. For instance, in the V_2 vacancy shown

in Fig. 5.2a the displacement vectors point towards the defect site along the x-axis, but away from the defect along the y-axis. Between the two axes, vortex like structures occur. A similar displacement pattern with alternating displacement directions forms also for the V_a vacancy shown in Fig. 5.2c. This behavior observed in the core region around the defect can not be reproduced by the simple defect model used here for the continuum theory calculations. The displacement field obtained in this model is either oriented towards the defect or away from it depending on the sign of the defect strength γ. For the V_3 vacancy, on the other hand, all displacement vectors point inward and no such complications occur. The displacement magnitude shown in Fig. 5.13(middle) follows qualitatively the form predicted by continuum theory. Here, a defect strength of $\gamma = -0.294\sigma^2$ was used as determined by minimizing the relative deviations between particle and continuum calculation over the whole xy-plane. For the V_2 and V_a vancancy, (see Fig. 5.13), one can only obtain agreement either in x- or y-direction by varying the defect strength γ, but not in both.

In Fig. 5.14 we depict the relative deviations of the displacement of the particle simulation from the continuum theory calculated according to Equ. 5.43. Even far from the defect the displacement field obtained from the particle simulation does not become isotropic such that it cannot be reproduced by the continuum theory calculations. The best agreement is found for V_3 (Fig. 5.14, center), in which case the anisotropy of the displacement field is less pronounced. The failure of the point defect model to reproduce the displacement patterns of vacancies, however, does not imply that elasticity theory is unsuitable for the description of such defects. Rather, the point defect model used here, which consists of two orthogonal pairs of opposing forces, appears to be to simple to capture the complex displacement patterns induced by vacancies.

5.5 Conclusion

Interstitials and vacancies occur in various configurations generating displacement fields with symmetries that differ from the symmetry of the underlying triangular lattice. Near the defect, the displacement fields are highly anisotropic and strongly dependent on the atomistic details of the interactions. In this distance regime, linear elasticity theory brakes down due to discrete lattice effects and non-linearities of the potential. For distances larger than about 10-15 lattice spacings, however, elasticity theory is valid. To establish this validity, it is crucial that corresponding boundary conditions are used both in the continuum calculations and the particle-based numerical simulations. Since simulations are usually carried out with periodic boundary conditions in order to minimize finite size effects, the same boundary conditions must be employed also in the continuum calculation. If different boundary conditions are used, the long-range nature of elastic displacement fields can lead to considerable discrepancies even at length scale where elasticity theory is expected to hold.

In this paper we have formulated the elastic theory problem in a way that makes it formally identical to the problem of determining the potential of a point charge in electrostatics. While here we have focused on two-dimensional systems, the same formalism applies also to three dimensions. Under periodic boundary conditions, this two-dimensional electrostatics problem has been solved using the method of Ewald summation [46, 47], in which the solution is expressed in terms of two rapidly convergent sums, one in real space and one in reciprocal space.

The solution of the electrostatics problem can be simply transferred to the continuum theory of the point defect. In this case, the role of the charge density in electrostatics is played by the dilatation, i.e. the local relative volume change. Accordingly, the charge neutrality required by the periodic boundary conditions in electrostatics corresponds to the condition of fixed volume in the elasticity theory. This requirement leads to a homogeneous neutralizing background that is seamlessly incorporated in the Ewald sum

solution. The neutralizing background satisfies the condition of fixed volume by exactly compensating for the volume change caused by the introduction of the point defect. The volume compensation leads to an additional term in the energy density related to the work done by the defect against the external pressure. Depending on the pressure, this energy can contribute significantly to the total defect energy.

While for interstitials the elasticity theory calculations carried out for a simple point defect model lead to good agreement with the particle calculations in the core region around the defect, large deviations are observed for vacancies. These discrepancies are due to the more complex displacement patterns of vacancies and better defect models are required to capture this behavior.

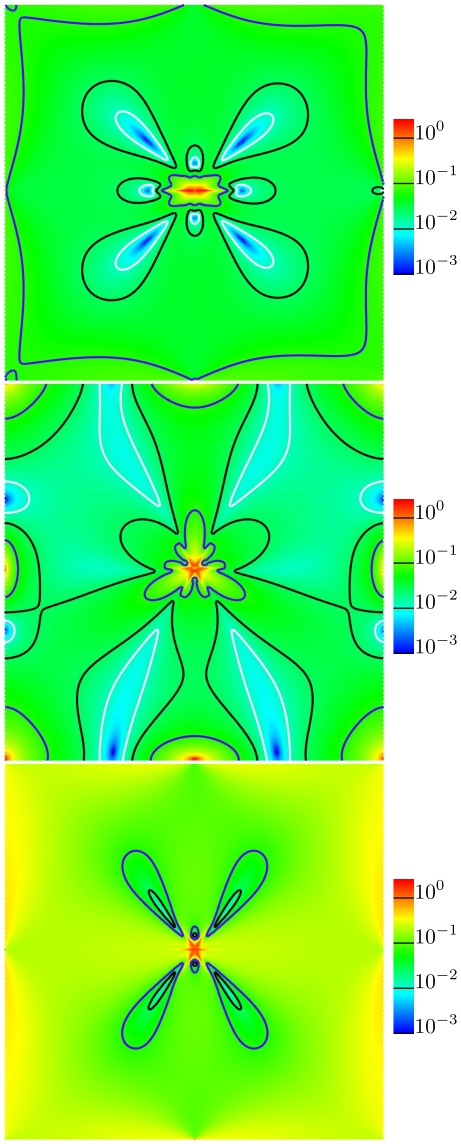

Figure 5.11: Color coded relative deviations of the displacement $\mathbf{u}_p(\mathbf{r})$ obtained numerically from the continuum theory prediction $\mathbf{u}_c(\mathbf{r})$ as a function of x and y calculated according to Equ. (5.43). From top to bottom, the figures depict the relative deviations for the I_2 interstitial ($\gamma = 0.23165\sigma^2$), the I_3 interstitial ($\gamma = 0.2347\sigma^2$), and the I_d interstitial ($\gamma = 0.2425\sigma^2$). The whole simulation cell of dimensions $L_x = 215.28\sigma$ and $L_y = 215.12\sigma$ is shown. Colors are assigned on a logarithmic scale which runs from 10^{-3} (blue) to 10^1 (red). The white, black, and blue contour lines represent a relative error of 1%, 2% and 5%, respectively.

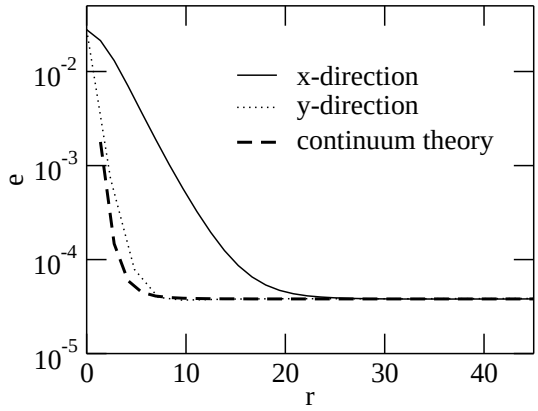

Figure 5.12: Energy density e of an I_2 interstitial in a periodic box as a function of the distance r measured along the x-direction (solid line) and the y-direction (dotted line). Also shown is the energy density obtained from continuum theory (dashed line) according to Equ. (5.15) for the displacement of Equ. (5.46).

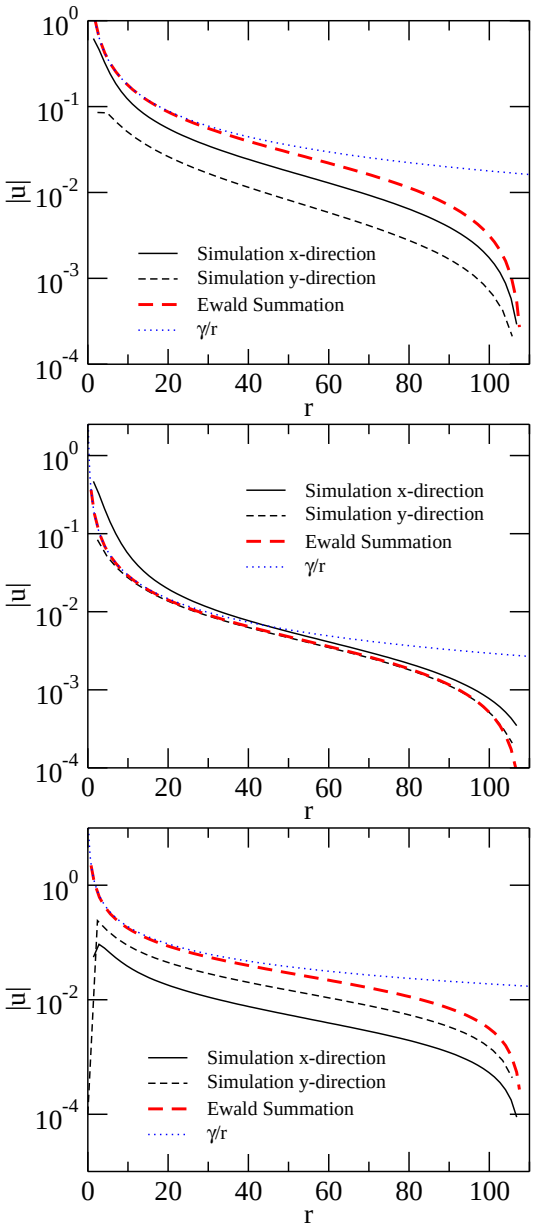

Figure 5.13: From top to bottom: Absolute value of the displacement components u_x (black solid line) and u_y (black dashed line) of a V_2, V_3 and V_a vacancy. Also plotted are the absolute values of the predicted displacement field from the Ewald summation Equ. (5.46) for the corresponding values of γ, found by minimizing the relative error of Equ. 5.43 over the whole xy-plane (dashed line), and $1/r$ behavior (dotted line).

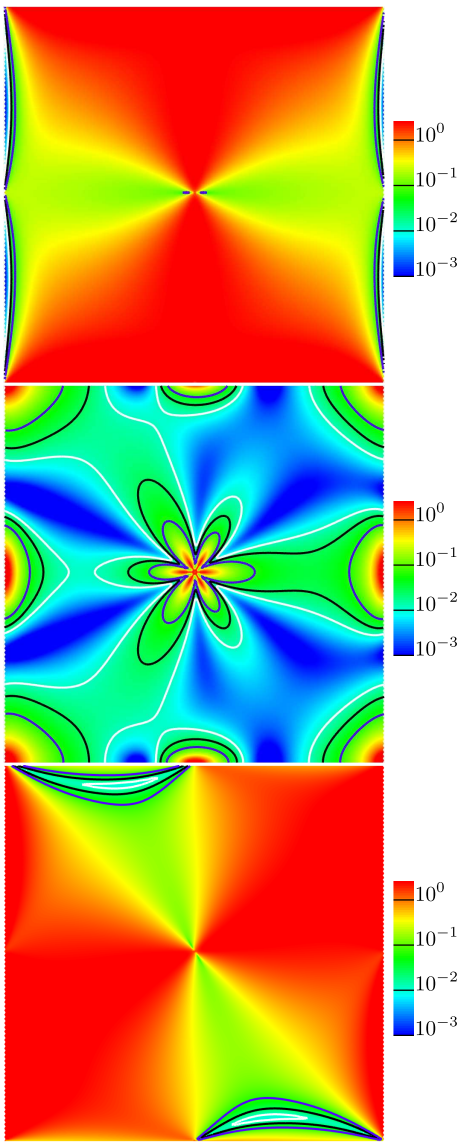

Figure 5.14: Color coded relative deviations Equ. (5.43) of the displacement obtained numerically for three different vacancy configurations from the prediction of continuum theory as a function of x and y. Color code and system size is the same as in Fig. (5.11). From top to bottom: V_2 vacancy ($\gamma = -1.78\sigma^2$), V_3 vacancy ($\gamma = -0.294\sigma^2$), and V_a vacancy ($\gamma = -1.89\sigma^2$).

Chapter 6

Interaction of point defects in two-dimensional colloidal crystals: formation of vacancy and interstitial clusters

We study the effective interactions between interstitials and vacancies in two-dimensional colloidal crystals with Monte Carlo simulations. For both types of defects the interactions are strongly attractive leading to the formation of defect strings. These highly mobile strings, two-dimensional analogs of prismatic dislocation loops observed in irradiated metals, arise from forces mediated by the lattice that cannot be reduced to effective pair interactions between defects.

6.1 Introduction

Colloidal suspensions with particle sizes in the micrometer regime often serve as analogs of condensed matter systems whose basic constituents, atoms and molecules, are many orders of magnitude smaller [71, 72]. With interactions that are usually known and frequently even controllable, such colloidal liquids

and crystals provide ideal experimental model systems in which concepts and theories, originally developed for atomic and molecular materials, can be probed with "atomistic" time and space resolution. Modern microscopic techniques now permit to track individual particles with high accuracy over long times providing a complete description of the microscopic processes that give rise to the macroscopic materials properties [28, 26, 27, 42, 43].

Recently, these tools of colloid physics have been applied to study the structure, dynamics and interactions of point defects in two-dimensional crystals. For example, using superparamagnetic colloidal particles confined to the air-water interface and observed with video microscopy, Maret and coworkers [28] have studied in detail the interactions of dislocation pairs that play a fundamental role in the Kosterlitz-Thouless-Halperin-Nelson-Young (KTHNY) theory of two-dimensional melting [29, 71, 73, 75]. Effective interactions obtained in these experiments from the statistics of defect separation essentially confirm elastic theory predictions of Taylor and Eshelby [76, 51] in a wide temperature range up to melting [28]. In other work, the diffusion of point defects was studied in experiments [41] as well as computer simulations [55] for colloidal particles interacting via a screened Coulomb repulsion. Both for vacancies and interstitials, the diffusion consists of fast uni-directional gliding phases punctuated by reorientation events. During the reorientation, the defects pass through various intermediate and less mobile configurations [68, 77].

In the present article, we study the interactions of interstitials and vacancies in two-dimensional colloidal crystals using computer simulations. Interactions of such point defects were studied earlier by various authors. Troyer and collaborators determined the binding energy of vacancies and interstitials in a system of particles interacting via a Lennard-Jones potential and found evidence of strong attraction, carrying implications for the supersolidity of Helium-4 [23]. A similar attractive interaction mediated by the lattice was found for both interstitials and vacancies by DaSilva and coworkers in the case of Yukawa interactions [24]. Here, we study defect interactions in a

system of particles interacting via $1/r^3$ dipole-dipole interactions as realized in the experiments of Maret and collaborators [78, 71, 73, 75, 28]. The strong attractive defect interactions found in our simulations lead to coalescence of defects and formation of highly stable defect clusters. Due to the non-linear character of the interactions, which cannot be represented as a superposition of pair interactions, the clusters have a string-like shape and are highly mobile in one dimension. Since the superposition principle is not valid for the interactions of defect clusters, these effective forces cannot be understood in terms of linear elasticity theory.

The defect strings observed in our simulations can be viewed as two-dimensional analogs of defect clusters that are produced in metals under irradiation or plastic deformation and are responsible for material embrittlement [79, 81, 80]. At high temperatures, the freely migrating vacancies and interstitials generated in radiation damage cascades during ion or neutron irradiation tend to aggregate and form planar clusters. These defect platelets, which can consist of hundreds of atoms, result in a prismatic dislocation loop around their perimeter [30]. Recently, it was found experimentally and in simulations that these dislocation loops exhibit one-dimensional diffusion with unusual high mobility comparable to that of a single defect [82, 83]. In two dimensions, the defect platelet reduces to a defect string and the prismatic dislocation loop becomes a pair of dislocations positioned at the ends of the strings. Just as the prismatic dislocation loops in three dimensions, the defect strings forming in the two-dimensional system are highly mobile in the direction of the Burgers vector of the dislocation pair. The formation of defect strings and their dynamics should be easily observable in experiments on two-dimensional lattices of superparamagnetic particles [71, 28].

The remainder of the paper is organized as follows. In Section 6.2 we define the model and explain how to locate defects and determine the effective interactions in our simulations. Effective interactions between vacancies and interstitials are studied in Sec. 6.3 and in Sec. 6.4 we investigate how these attractive interactions lead to the formation of string-like defect clusters. A

discussion and concluding remarks are provided in Section 6.5.

6.2 Methodology

The system we study here consists of particles in two dimensions interacting via the pair potential

$$v(r) = \frac{v_0}{r^3}, \tag{6.1}$$

where r is the interparticle distance and the parameter v_0 with dimensions of energy $\times$ volume controls the interaction strength. In experiments, such an interaction can be realized with superparamagnetic colloids confined to a flat air-water interface and exposed to a magnetic field B perpendicular to the interface [78, 71, 75, 28]. The magnetic field induces magnetic dipole moments $M = \chi B$ on the particles with effective susceptibility χ, leading to a dipole-dipole repulsion between the particles that can be controlled in magnitude by tuning the magnetic field. With appropriate scaling of the spatial dimensions, the structure and thermodynamics of the system solely depend on the dimensionless coupling parameter $\Gamma = \beta(\mu_0/4\pi)(\chi B)^2(\pi\rho)^{3/2}$, where β is the inverse temperature, μ_0 is the permeability of free space, and $\rho = 2/(\sqrt{3}a^2)$ is the two-dimensional number density [75]. Since in this paper we use the lattice spacing a of a perfect hexagonal lattice with density $\rho = 2/(\sqrt{3}a^2)$ as the unit of length, we write the pair potential as

$$\beta v(r) = \frac{3^{3/4}\Gamma}{(2\pi)^{3/2}} \left(\frac{a}{r}\right)^3 \tag{6.2}$$

such that the interaction strength from Equ. (6.1) is given by

$$v_0 = k_\mathrm{B}T 3^{3/4}\Gamma a^3/(2\pi)^{3/2}. \tag{6.3}$$

The coupling parameter Γ, which is the only relevant parameter in the simulation, can be viewed as an inverse temperature. For $\Gamma > 60$, the system exists as a hexagonal crystal [71, 73]. In the experiments, Γ can be tuned

over a wide range, at least from 10 to 300 [74].

We study the effective interaction between interstitials and vacancies and the structure of defect clusters using Monte Carlo simulations in the NVT ensemble. The particle number is $N = 52 \times 60 = 3120$ plus/minus the number of interstitials/vacancies introduced into the system. Periodic boundary conditions apply to the almost square simulation box with aspect ratio 0.9992 and the cutoff radius for the pair interactions is $5a$. Energies are expressed in units of $\epsilon = v_0/a^3 = k_\mathrm{B}T 3^{3/4}\Gamma/(2\pi)^{3/2}$. Thus, the thermal energy is given by $k_\mathrm{B}T = (2\pi)^{3/2}\epsilon/3^{3/4}\Gamma$.

For the analysis of defect interactions, one needs to specify the number and positions of all defects in the system. To do that, we introduce an underlying perfect hexagonal lattice consisting of n lattice sites. Each of the particles is assigned to the lattice site nearest to it. As a result, each lattice site has either zero, one, or two particles assigned to it. Lattice sites with zero or two particles are identified as vacancies or interstitials, respectively. The positions of these point defects are defined to coincide with the corresponding lattice sites with anomalous occupation. From this algorithm, one obtains the numbers N_V and N_I of vacancies and interstitials, respectively, as well as their positions. Accordingly, the total number of particles in the system is $N = n - N_V + N_I$.

Each simulation is started with particles located at the sites of the perfect lattice, possibly with a few empty sites and a few particles in off-lattice positions depending on the type of defects one wants to study. In the course of the Monte Carlo simulation, however, the crystal slowly diffuses as a whole with respect to the lattice such that the position of the underlying lattice must be regularly adjusted to compensate for this diffusive motion. This is done by translating the underlying lattice such that the average distances in x- and y-direction of the lattice sites from their assigned particles vanishe. This synchronization is done every 100 MC Steps.

Based on the above definition of the defect positions, the free energy as a function of the separation vector $\mathbf{r}$ between two point defects present in the

system is given by

$$\hat{F}(\mathbf{r}) = -k_{\mathrm{B}}T \ln \hat{P}(\mathbf{r}). \tag{6.4}$$

Here, $\hat{P}(\mathbf{r})$ is the probability to find the two point defects at positions separated by $\mathbf{r}$. Note, that with our definition of the defect positions only discrete defect separations $\mathbf{r} = \mathbf{r}_i - \mathbf{r}_j$ are possible, where $\mathbf{r}_i$ and $\mathbf{r}_j$ are lattice vectors and the minimum image convention applies.

It is also instructive to consider the free energy as a function of the distance $r = |\mathbf{r}|$ rather than the separation vector,

$$F(r) = -k_{\mathrm{B}}T \ln \frac{P(r)}{n(r)}. \tag{6.5}$$

In the definition of this effective interaction we have divided $P(r)$, the probability to observe the defect pair at distance r, by the number $n(r)$ of lattice points at distance r. For the perfect hexagonal lattice, the first few distance degeneracies are $n(1) = 6$, $n(\sqrt{3}) = 6$, $n(2) = 6$, $n(\sqrt{7}) = 12$, $n(3) = 6$, $n(2\sqrt{3}) = 6$, $n(\sqrt{13}) = 12$, and $n(4) = 6$. Due to this normalization, which corresponds to measuring the distance distribution $P(r)$ relative to the distribution of a non-interacting defect pair, the effective interaction $F(r)$ is the reversible work required to transport the defects from infinite distance to distance r. Interstitials and vacancies can occur in a number of distinct configurations [68, 77]. Here, however, we do not distinguish between these configurations and the free energies defined above can be viewed as resulting from a weighted average over all possible combinations of defect configurations.

Since the effective interactions we study here are strongly attractive with magnitudes that can by far exceed the thermal energy $k_{\mathrm{B}}T$, a straightforward Monte Carlo simulation started from two point defects in close proximity would fail to yield sufficient statistics for larger defect separations. To circumvent this sampling problem, we have determined $P(r)$ using window sampling [35] with 10 overlapping hard wall windows. Each window has a width of 4 lattice spacings and overlaps with each neighboring window by 3

lattice spacings. In each window, 10^7 Monte Carlo sweeps were carried out. Other than the window restrictions, no bias is applied in the simulations. Due to thermal fluctuations, additional pairs of interstitials and vacancies can form spontaneously. However, the difference between the number N_0 of unoccupied lattice sites and the number N_2 of doubly occupied lattice sites $N_2 - N_0 = N_I - N_V$ remains constant. Configurations with more than the two defects introduced at the beginning were not taken into account for the free energy calculation. In all cases, these configurations amounted to less than 1% of all configurations.

6.3 Effective interactions

Using the methods described in the previous section we have determined the effective interactions of interstitials and vacancies.

The effective interactions of two interstitials computed for interaction strengths from $\Gamma = 80$ to $\Gamma = 140$ are depicted in the top panel of Fig. 6.1. For these particular values of Γ, which are all accessible experimentally [28], the system resides in the crystalline phase. As can be inferred from the figure, for all inverse temperatures Γ, the interaction between two self interstitials is attractive overall and has a range of about $6 - 7$ lattice spacings. The minimum of the effective interaction occurs at a separation of one lattice spacing for all values of Γ except for $\Gamma = 80$. In this case, which corresponds to the highest temperature, the minimum is located at a separation of $r = \sqrt{3}a$. Note that the strong irregularities of the curves arise from the projection of the two dimensional lattice to one dimension and do not represent local minima that stabilize particular defect separations. This absence of local minima is evident in Fig. 6.2a where the full two dimensional free energy $\hat{F}(\mathbf{r})$ landscape is depicted as a function of x and y. For all temperatures, the particular distance dependence is very similar up to a factor that varies with temperature. Most likely, this effect is due to the temperature dependence of the elastic properties of the crystal.

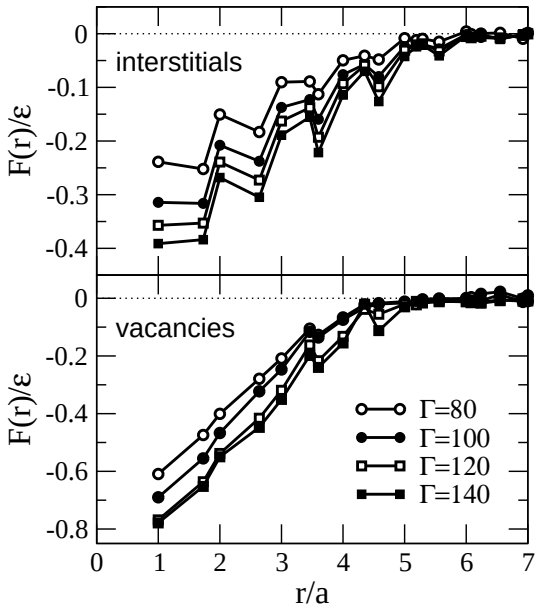

Figure 6.1: Effective interaction $F(r)$ between two single interstitials (top) and two single vacancies (bottom) as a function of distance r for various interaction strengths ranging from $\Gamma = 80$ up to $\Gamma = 140$. These values of Γ correspond to thermal energies ranging from $k_{\mathrm{B}}T = 0.086\epsilon$ to $k_{\mathrm{B}}T = 0.049\epsilon$.

Even stronger attractive interactions act between vacancies. Effective interactions $F(r)$ as a function of the distance between two vacancies are shown in the bottom panel of Fig. 6.1 for different interaction strengths Γ. Compared to the interstitial case, the interactions of two vacancies are about twice as strong and have a less structured distance dependence, as is evident also from the two-dimensional free energy landscape shown in Fig. 6.3. The interaction range is comparable and also the temperature dependence of $F(r)$ is of similar magnitude. While the interaction between vacancies is considerably stronger than that between interstitials, it is still smaller by a factor of about 2 than the vacancy-interstitial interaction as depicted in the bottom panel of Fig. 6.5.

If multiple vacancies or interstitials are present in the system, they tend to aggregate and form defect clusters. To investigate attractive effective forces that lead to this behavior in more detail we have studied the interactions

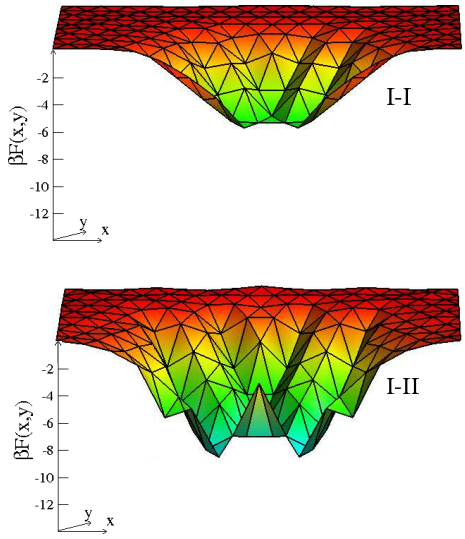

Figure 6.2: Effective interaction $F(\mathbf{r})$ between two interstitials (I-I) and an interstitial pair in contact and an additional interstitial (I-II) plotted as a function of x and y for $\Gamma = 120$.

of more than two defects using Monte Carlo simulations. In particular, we have determined the effective interaction of an interstitial with a pair of interstitials in close contact. As in the case of the defect pair, we collected statistics on the separation between the single interstitial and the interstitial pair and determined from it the free energies $\hat{F}(\mathbf{r})$ and $F(r)$. As sketched in Fig. 6.4, here the separation $\mathbf{r}$ is the vector from the center of mass (S) of the interstitial pair (A and B) to the third interstitial (C), and $r = |\mathbf{r}|$. Also for this type of interaction the distances r can take only discrete values. However, the possible distances differ from those between two interstitials due to the intermediate position of the center of mass S between two lattice points. Also the number $n(r)$ of separation vectors with length r needs to be adapted accordingly.

The effective interaction between an interstitial pair in contact and a third interstitial is depicted in the top panel of Fig. 6.5 with open squares connected by straight lines. Again, this seemingly rough energy profile does not exhibit any local minima in the two dimensional representation of $\hat{F}(\mathbf{r})$ shown in Fig. 6.2b. In this figure, the center of mass of the defect pair is

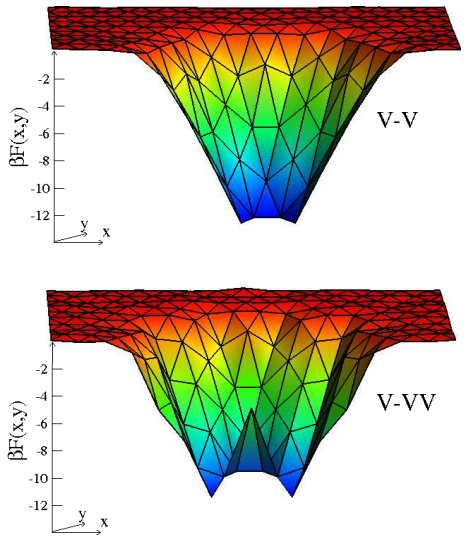

Figure 6.3: Effective interaction $F(\mathbf{r})$ between two vacancies (V-V) and a vacancy pair in contact and an additional vacancy (V-VV) plotted as a function of x and y for $\Gamma = 120$.

located at the origin and the pair is oriented along the x-axis. The points in the xy-plane represent the position of the third interstitial with respect to S. The effective interaction $F(r)$ between the pair and the single interstitial has a minimum at a distance of $r = 1.5a$ from S, corresponding to the locations denoted by M_1 and M_2 in the sketch of Fig. 6.4. These positions are in line with the axis of the interstitial pair. The defect positions D_1 and D_2 directly above and below S are the defect positions closest to S with a distance of only $r = \sqrt{3}/2a \approx 0.866a$. Even so, they have a free energy that is about 5 $k_\mathrm{B}T$ higher than the minimum. In other words, the most favorable configuration of a cluster of three interstitials is linear rather than triangular reflecting the tendency of defects to form strings.

To investigate the nature of the forces favoring the linear arrangement of interstitials, we have determined the free energy expected if linear elasticity theory is valid. In this case, the displacement field caused by the three interstitials is the superposition of the displacement fields of the individual defects. Consequently, the effective interactions of the single interstitial (C) with the defect pair (A & B) can be obtained as a sum of the interactions

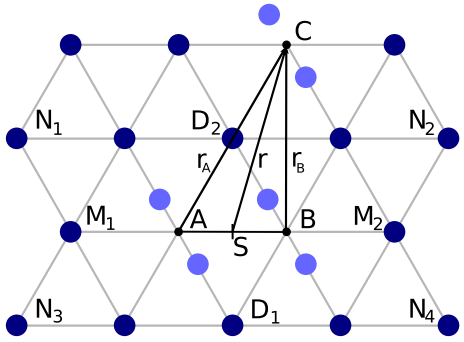

Figure 6.4: Schematic sketch of the geometry of the interaction of a single defect with a defect pair. Large blue circles denote the particles and small black dots the lattice points. Particles belonging to the interstitial defects are shown in a lighter shade. The system consists of three interstitials, A,B and C, located at the positions of the doubly occupied lattice points. The vector $\mathbf{r}$ connects the center of mass S of the defect pair and the additional interstitial C. The vectors $\mathbf{r}_A$ and $\mathbf{r}_B$ are the distances between the individual interstitials A and B, and the additional interstitial C. The significance of the sites D_i, M_i, and N_i is explained in the main text. Note that for given positions A and B, the defect pair has two equivalent orientations. In contrast, a single interstitial has three possible orientations. The free energies presented in this paper are obtained from averages over all different defect configurations.

of C with A and C with B. The effective interaction obtained in this superposition approximation is shown in the top panel of Fig. 6.5 as full squares connected with straight lines. For large distances, the superposition approximation yields an effective interaction that differs only little from the exact interaction, for short distance, however, important deviations occur. In contrast to the exact interaction, the superposed free energy has its minimum for the smallest possible distance corresponding to the positions D_1 and D_2. So in the superposition approximation the most favorable defect arrangement is triangular rather than linear. The formation of interstitial strings observed in our simulations can therefore be viewed as a non-linear effect.

Also vacancies tend to aggregate due to attractive interactions between them. The bottom panel of Fig. 6.5 shows the interaction between two vacancies (V-V) and the interaction between a pair of vacancies in close

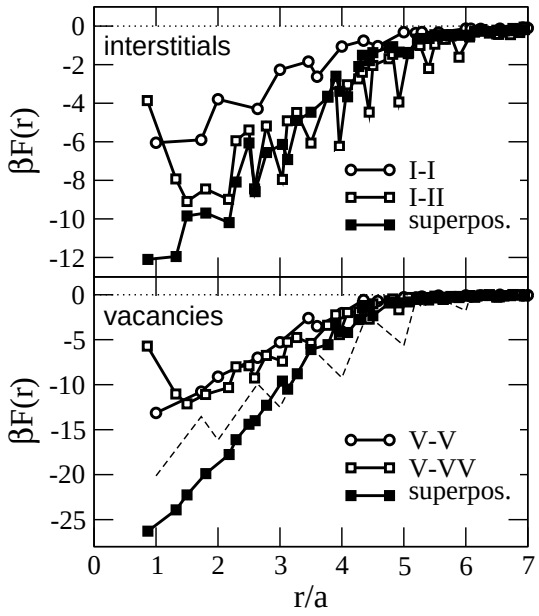

Figure 6.5: *Top:* Effective interaction $F(\mathbf{r})$ for $\Gamma = 120$ between two individual interstitials (I-I) and between a pair of two interstitials in close contact and an additional interstitial (I-II). Also shown is the superposition of two pair interactions (superpos.) as described in detail in the text. *Bottom:* Effective interaction for $\Gamma = 120$ between two individual vacancies (V-V) and between a pair of two vacancies and an additional vacancy (V-VV). Also shown is the superposition of two pair interactions (superpos.). For comparison, the dashed line denotes the interaction of a vacancy with an interstitial.

contact and an additional vacancy (V-VV). Also shown in this figure is the interaction between the contact pair and the extra vacancy obtained in the superposition approximation (superpos.). The interaction between two single vacancies is remarkably strong compared to the interaction of interstitials. At their minimum, the effective interactions of vacancies exceed those of interstitials by more than a factor of two. In contrast to interstitials, however, the interaction of a single vacancy with a pair of vacancies in close contact is comparable with that of two vacancies. Therefore, the superposition of two pair interactions exceeds the true interaction strength by about a factor of 2. Also for vacancies, the minimum free energy between a single vacancy and a pair of vacancies in contact is at a separation of $1.5a$ with respect to S.

Therefore, also vacancies have the tendency to form strings, as the free energy difference between the triangular configuration and the linear configuration is about $7k_BT$. The effective interaction $F(\mathbf{r})$ for the pair and the triple of vacancies are shown in Fig. 6.3 in the xy-plane. Compared to the interstitial case, this free energy is less structured.

6.4 Defect strings

If multiple interstitials or vacancies are introduced into the crystal, they rapidly coalesce forming defect clusters with string-like geometry. A few snapshots, taken from Monte Carlo simulations, of typical configurations of interstitial and vacancy clusters are shown in Figs. 6.6 and 6.7, respectively. In our simulations we have studied systems with up to 40 interstitials and vacancies and have observed string formation in all cases.

More details about the structures of defect strings are revealed using a Voronoi cell construction employed previously in studies of two dimensional crystals [28, 43, 55]. This kind of analysis permits to determine the number of neighbors of each particle. While in a perfect crystal each particle is coordinated by exactly 6 neighbors, at the two endpoints of the string pairs of particles coordinated by 5 and 7 particles occur shown in Figs. 6.6 and 6.7 as orange and green spheres, respectively. These 5-7 pairs are a manifestation of dislocations, which are point defects in two dimensions. These dislocations, characterized by Burgers vectors of unit length orthogonal to the vector from the 5- to the 7-coordinated particle, can be viewed as arising from the addition or removal of a string of particles to/from the perfect lattice. Two 5-7 pairs occur already for one single interstitial or vacancy. While in the case of interstitial strings the vectors from the 5- to the 7-coordinated particles points outward with respect to the string, they point inward in the case of vacancies. In both cases, the sum of the two Burgers vectors belonging to the two dislocations at the string ends vanishes. Similar dislocation pairs consisting of 5-7 combinations can arise also spontaneously in the absence

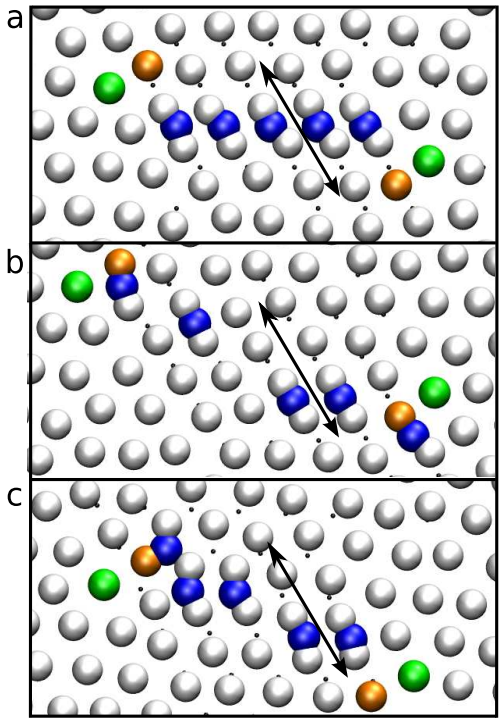

Figure 6.6: Snapshot of three typical configurations taken from a Monte Carlo simulation of a system with five interstitials. The small black dots correspond to the lattice sites. Large white spheres are particles with 6 Voronoi neighbors. Orange and green spheres denote particles with 5 and 7 Voronoi neighbors, respectively, and the blue spheres represent the interstitial positions. The defect string is highly mobile in the direction of the arrow, which points into the direction of the Burgers vector of the 5-7 pairs.

of interstitials and vacancies and the thermal unbinding of such dislocation pairs is at the center of the KTHNY-theory of two-dimensional melting [29]. In contrast to these dislocation pairs arising by thermal excitation, the dislocation pairs at the string end-points can not annihilate with each other.

At finite temperature, the defect strings are not rigid but fluctuate about the perfect string configurations shown in Figs. 6.6a and 6.7a for interstitials and vacancies, respectively. In these configurations, which arise from the motion of the defects in direction of the Burgers vectors, the strings shapes deviate from the linear structure as shown in panels b and c of the figures. To quantify the deviations from the perfect linear shape we have studied the

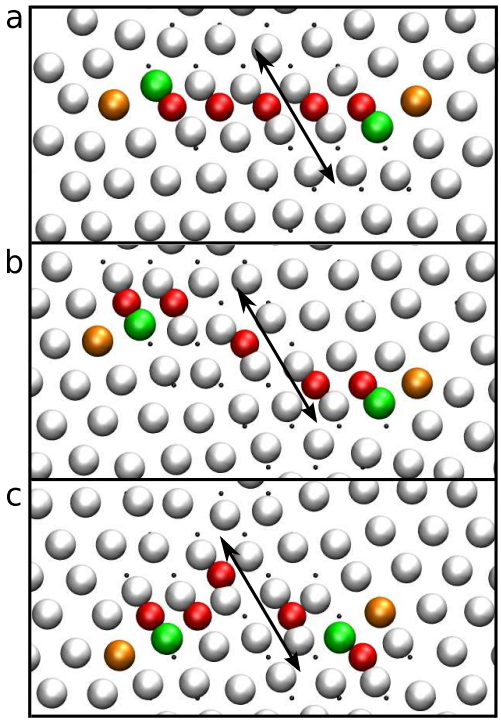

Figure 6.7: Snapshots of three typical defect cluster configurations taken from a Monte Carlo simulation of a system with five vacancies. Red spheres denote unoccupied lattice sites corresponding to vacancies and the color code for the other particles is the same as in Fig. 6.6. The defect string is highly mobile in the direction of the arrow, which points into the direction of the Burgers vector of the 5-7 pairs.

statistics of the end-to-end distance R of the strings. For interstitial strings, the end-to-end distance R is the distance between the two 5-coordinated particles whereas for vacancy strings R is given by the distance between the two 7-coordinated particles. As displayed in the bottom panel of Fig. 6.8, the average end-to-end distance of interstitial and vacancy strings grows about linearly with the defect number N_d. Due to the thermal fluctuations of the string shape, the average end-to-end distance exceeds the length of the straight string as reflected by a slope larger than unity of the $\langle R \rangle$ vs. N_d curves. This effect is more pronounced for interstitial than for vacancy strings and can be understood in terms of the effective potentials of a defect pair with an additional defect as shown in Fig. 6.5. While for interstitials the

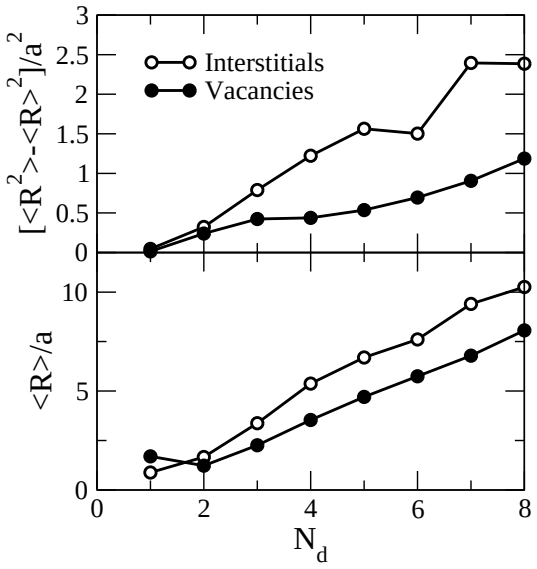

Figure 6.8: Average end-to-end distance $\langle R \rangle$ (bottom) and fluctuations of the end-to-end distance $\langle R^2 \rangle - \langle R \rangle^2$ (top) as a function of the string size N_d, *i.e.*, the number of defects in the string. For interstitial strings the end-to-end distance is defined to be the distance between the two 5-coordinated particles at the string ends and for vacancy strings it is the distance between the 7-coordinated particles.

minimum of the effective interaction is rather broad encompassing more than one configuration, the minimum is narrow for vacancies. As a consequence, vacancy strings are stiffer than interstitial strings. The different stiffness of interstitial and vacancy strings is also reflected in larger fluctuations of the end-to-end distance for interstitial than for vacancy strings (see top panel of Fig. 6.8).

The defect strings observed in our Monte Carlo simulations are surprisingly mobile. The highly anisotropic gliding of single interstitials and vacancies [55, 41] occurs also for defect strings. The strings move predominantly in the direction of the Burgers vectors as indicated by the arrows in Figs. 6.6 and 6.7. In all other directions diffusion is very slow. Reorientations of the strings, or, equivalently, of the Burgers vectors, into another one of the three equivalent directions occurs very rarely with a rate that decreases with increasing string length. This type of motion is reflected by the traces shown

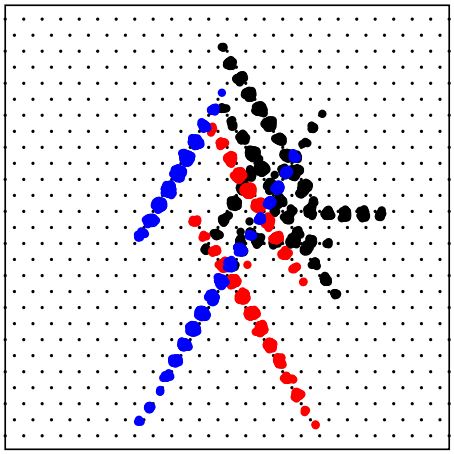

Figure 6.9: Traces of interstitial strings of different length over a time period of 200,000 Monte Carlo steps per particle. The circles mark the positions of the string endpoints identified with the 5-coordinated particles for $N_I = 3$ (black), $N_I = 5$ (red), and $N_I = 8$ (blue) defects. The points indicate the lattice sites of the underlying perfect lattice.

in Fig. 6.9 of interstitial strings of length $N_I = 3$, 5, and 7 followed over 200,000 Monte Carlo sweeps. One sweep corresponds to one attempted move per particle in the average. Depicted as full circles are the two 5-coordinated particles residing at both string ends. For all string lengths, the motion is highly anisotropic and the strings essentially move only in the direction of the Burgers vectors pointing in one of the three equivalent low-index lattice directions. During the time of the simulation, equal for all string sizes, only the shortest strings reorient into directions different from the initial one. The longer strings do not reorient and move with mobility comparable to that of the short string. Vacancy strings behave similarly. Such high one-dimensional mobility has also been observed in interstitial clusters in face-centered cubic metals [82].

6.5 Conclusion

Interstitials and vacancies introduced into two-dimensional colloidal crystals interact strongly and attractively with defects of the same species despite of

the purely repulsive forces between the particles. These interactions lead to the aggregation of defects and the formation of defect clusters. Due to the particular form of the interactions, which is a non-linear effect that cannot be understood in terms of linear elasticity theory, the clusters are shaped like strings that fluctuate around the straight shape at finite temperatures. At both ends of the strings dislocations occur, that can be viewed as the two-dimensional analogs of prismatic dislocation loops arising along the circumference of platelet-shaped interstitial or vacancy clusters forming, for instance, in irradiated metals [84, 82, 83]. The motion of the defect strings is characterized by rapid diffusion along the direction of the Burgers vectors of the dislocations punctuated by rare rotations, during which the strings change the main direction of motion. A more quantitative study of the diffusive motion of defect strings will be the subject of future studies.

The formation of string-like defect clusters of interstitials and vacancies is robust with respect to the choice of interaction potential determining the forces between the particles and also with respect to the thermodynamic state. For the $1/r^3$ potential, defect strings form over the whole range of Γ investigated here, *i.e.*, between $\Gamma = 80$ to $\Gamma = 200$. We have observed string formation also using various other potentials including the Lennard-Jones, the Yukawa, and the Gaussian core potential. However, exceptions exist. In the Lennard-Jones system at zero temperature and pressure, for instance, three vacancies or interstitials form a triangular cluster rather than a string [23]. However, our Monte Carlo simulations show that at finite temperature the triangular configuration becomes unstable and the string is the most favorable configuration. Since defect strings form for various particle interactions and wide parameter ranges, we are confident that these defect structures will be found also experimentally in colloidal crystals.

Bibliography

[1] K.F. Kleton, *Solid State Physics* **45**, 75 (1991).

[2] P. R. ten Wolde, M. J. Ruiz-Montero, and D. Frenkel, *J. Chem. Phys.* **104**, 9932 (1996).

[3] S. Auer and D. Frenkel, *Adv. Polym. Sci* **173**, 149 (2005).

[4] J. S. van Duijneveldt and D. Frenkel, *J. Chem. Phys.* **96**, 4655 (1992).

[5] P. Bhimalapuram, S. Chkrabarty, and B. Bagchi, *Phys. Rev. Lett.* **98**, 206104 (2007).

[6] P. R. ten Wolde, M. J. Ruiz-Montero, and D. Frenkel, *J. Chem. Phys.* **110**, 1591 (1999).

[7] J. A. van Meel, A. J. Page, R. P. Sear, and D. Frenkel, *J. Chem. Phys.* **129**, 204505 (2008).

[8] B. Chen, H. Kim, S. J. Keasler, and R. B. Nellas, *J. Phys. Chem. B* **112**, 4067 (2008).

[9] S. Luo, L. Zheng, A. Strachen, and D. C. Swift, *J. Chem. Phys.* **126**, 034505 (2007).

[10] P. G. Debenedetti, *Nature* **441**, 168 (2006).

[11] A. C. Pan, T. J. Rappl, D. Chandler, and N. P. Balsara, *J. Phys. Chem.* **110**, 3692 (2006).

[12] U. Gasser, E. R. Weeks, A. Schonfield, P. N. Pusey, and D. A. Weitz, *Science* **292**, 258 (2001).

[13] F. H. Stillinger, *J. Chem. Phys.* **65**, 3968 (1976).

[14] S. Prestipino, F. Saijta, and P. V. Giaquinta, *Phys. Rev. E* **71**, 050102(R) (2005).

[15] S. Prestipino, F. Saijta, and P. V. Giaquinta, *J. Chem. Phys.* **123**, 144110 (2005).

[16] W. Ostwald, *Z. Phys. Chem.* **22**, 289 (1897).

[17] S. Alexander and J. McTague, *Phys. Rev. Lett.* **41**, 702 (1978).

[18] P. R. ten Wolde and D. Frenkel, *Phys. Chem. Chem. Phys.* **1**, 2191 (1999).

[19] P. R. ten Wolde, M. J. Ruiz-Montero and D. Frenkel, *Phys. Rev. Lett.* **75**, 2714 (1995).

[20] D. Moroni, P. R. ten Wolde, and P. G. Bolhuis, *Phys. Rev. Lett.* **94**, 235703 (2005).

[21] C. Desgranges and J. Delhommelle, *J. Phys. Chem. B* **111**, 1465 (2007).

[22] P. Steinhardt, D. R. Nelson, and M. Ronchetti, *Phys. Rev. B* **28**, 784 (1983).

[23] P. N. Ma, L. Pollet, M. Troyer, and F. C. Zhang, *J. Low Temp. Phys.* **152**, 156 (2008).

[24] L. C. DaSilva, L. Candido, L. D. F. Costa, and O. N. Oliveira, *Phys. Rev. B* **76**, 035441 (2007).

[25] A. Ashkin, J. M. Dziedzic, J. E. Bjorkholm, and S. Chu, *Opt. Lett.* **11**, 288 (1986).

[26] V. Prasad, D. Semwogerere, and E. R. Weeks, *J. Phys.: Cond. Mat.* **19**, 113102 (2007).

[27] U. Gasser, E. R. Weeks, A. Schofield, P. N. Pusey, and D. A. Weitz, *Science* **292**, 258 (2001).

[28] C. Eisenmann, U. Gasser, P. Keim, G. Maret, and H.-H. von Grünberg, *Phys. Rev. Lett.* **95**, 185502 (2005).

[29] J. Kosterlitz and D. Thouless, *J. Phys. C* **6**, 1181 (1973); B. Halperin and D. Nelson, *Phys. Rev. Lett.* **41**, 121 (1978).

[30] J. P. Hirth and J. Lothe, *Theory of Dislocations*, Krieger Publishng Company, Malabar, Florida (1992).

[31] D.B. Fahrenheit, *Philos. Trans. Roy. Soc.* **33**, 78 (1724).

[32] P. J. Flory, *Principles of Polymer Chemistry*, Cornell University Press, Ithaca (1953).

[33] G. M. Torrie and J. P. Valleau , *Chem. Phys. Lett.* **28**, 154 (1974).

[34] C. J. Geyer and E. A. Thompson, *J. Am. Stat. Assoc.* **90**, 909 (1995).

[35] D. Frenkel and B. Smit, "Understanding Molecular Simulation", Academic Press, San Diego (2002).

[36] B. Coasne, S. K. Jain, L. Naamar, and K. E. Gubbins, *Phys. Rev. B* **76**, 085416 (2007).

[37] S. Ogata, *Phys. Rev. A* **45**, 1122 (1992).

[38] I. Volkov, M. Cieplak, J. Koplik, and J. R. Banavar, *Phys. Rev. E* **66**, 061401 (2002).

[39] L. Landau and E. Lifschitz, "Quantum Mechanics", Pergamon, London (1965).

[40] J. L. Johnson, J. A. Zollweg, and K. E. Gubbins, *Mol. Phys.* **78**, 591 (1993).

[41] A. Pertsinidis and X. S. Ling, *Nature* **413**, 147 (2001).

[42] A. Pertsinidis and X. S. Ling, *New J. Phys.* **7**, 33 (2005).

[43] A. Pertsinidis and X. S. Ling, *Phys. Rev. Lett.* **87**, 098303 (2001).

[44] K. Zahn, R. Lenke, and G. Maret, *Phys. Rev. Lett.* **82**, 2721 (1999).

[45] C. Eisenmann, U. Gasser, P. Keim, G. Maret, and H.H. von Grünberg, *Phys. Rev. Lett.* **95**, 185502 (2005).

[46] S. W. de Leeuw and J. W. Perram, *Physica* **113A**, 546-558 (1982).

[47] R. Karch, M. Neumann, F. Neumann, R. Ullrich, J. Neumüller, and W. Schreiner, *Physica* **369A**, 599-611 (2006).

[48] F. H. Stillinger and T. A. Weber, *J. Chem. Phys.* **74**, 4015 (1981).

[49] W. Lechner and C. Dellago, *Soft Matter*, in preperation (2009).

[50] L. Landau and E. Lifschitz, "Theory of Elasticity", Pergamon, London (1959).

[51] J. D. Eshelby, *Phil. Trans. R. Soc. A*, **244** , 87 (1951).

[52] J. D. Eshelby, *Act. Met.* **3**, 487 (1955).

[53] D. J. Bacon, D. M. Barnett, and R. O Scattergood, *Progr. Mat. Sci.* **23**, 51 (1979).

[54] R. Courant and D. Hilbert, "Methods of Mathematical Physics I", Wiley (1991).

[55] A. Libal, C. Reichhardt, and C. J. Olson Reichhardt, *Phys. Rev. E*, 011403 (2007).

[56] G. Y. Hu and R. F. O'Connel, *J. Phys. A: Math Gen.* **29**, 1511-1513 (1996).

[57] D. S. Fisher, B. I. Halperin, and R. Morf, *Phys. Rev. B* **20**, 4692 (1979).

[58] K. Bagchi, H. C. Andersen, and W. Swope, *Phys. Rev. E* **53**, 3794 (1995).

[59] K. Bagchi, H. C. Andersen, and W. Swope, *Phys. Rev. Lett.* **76**, 255 (1995).

[60] H. C. Andersen and W. Swope, *J. Chem. Phys.* **102**, 2851 (1995).

[61] E. Kim and M. H. W. Chan, *Nature* **427**, 225 (2004).

[62] W. Cai, V. V. Bulatov, J. Chang, J. Li, and S. Yip, *Phys. Rev. Lett.* **86**, 5727 (2001).

[63] W. Cai, V. V. Bulatov, J. Chang, J. Li, and S. Yip, *Phil. Mag.* **83**, 539 (2003).

[64] A. J. C. Ladd and W. G. Hoover, *Phys. Rev. B* **26**, 5469 (1982).

[65] P. B. Bladon and D. Frenkel, *J. Phys. Chem.* **180**, 6707 (2004).

[66] F. H. Stillinger and T. A. Weber, *J. Chem. Phys.* **74**, 4020 (1981).

[67] M. Parrinello and A. Rahman, *Phys. Rev. Lett.* **45**, 1196 (1980).

[68] W. Lechner, E. Schöll-Paschinger, C. Dellago, *J. Phys.: Condens. Matter* **20**, 40402 (2008).

[69] L. Tewordt, *Phys. Rev.* **109**, 1 (1958).

[70] M. Neumann, personal communication (2008).

[71] K. Zahn, R. Lenke, and G. Maret, *Phys. Rev. Lett.* **82**, 2721 (1999).

[72] P. Schall, I. Cohen, D. A. Weitz, F. Spaepen, *Science* **305**, 1944 (2004).

[73] K. Zahn, R. Lenke, and G. Maret, *Phys. Rev. Lett.* **85**, 3656 (2000).

[74] P. Keim, personal communication (2009).

[75] P. Keim, G. Maret, U. Herz, and H. H. von Grünberg *Phys. Rev. Lett.* **92**, 215504 (2004).

[76] G. I. Taylor, *Proc. R. Soc. A*, **145** , 362 (1934).

[77] W. Lechner and C. Dellago, *Soft Matter*, **5**, 646 (2009).

[78] K. Zahn, J. M. Méndez-Alcaraz, and G. Maret, *Phys. Rev. Lett.* **79**, 175 (1997).

[79] K. W. Ingle, R. C. Perrin, and H. R. Schober, *J. Phys. F: Metal Phys.* **11**, 1161 (1981).

[80] Yu. N. Osetsky, D. J. Bacon, A. Serra, B. N. Singh, and S. I. Golubov, *J. Nuc. Mat.* **276**, 65 (2000).

[81] V. Gavini, K. Batthacharya, and M. Ortiz, *Phys. Rev. B* **76**, 180101 (2007).

[82] Y. Matsukawa and S. J. Zinkle, *Science* **318**, 959 (2007).

[83] K. Arakawa, K. Ono, M. Isshiki, K. Mimura, M. Uchikoshi, and H. Mori, *Science* **318**, 956-959 (2007).

[84] D. Hull and D. J. Bacon, 'Introduction to Dislocations', Butterworth-Heinemann, Oxford (2001).